MECHANISTIC ANALYSIS OF MICROTUBULE DYNAMICS AND REGULATION

APPROVED BY SUPERVISORY COMMITTEE

Luke M. Rice, Ph.D

Khuloud Jaqaman, Ph.D.

Michael K. Rosen, Ph.D.

Hongtao Yu, Ph.D.

DEDICATION

This dissertation is dedicated to my parents, family, friends and my fiancée Eric: all of these people have collectively helped to keep me sane and get me to this place in my educational journey.

MECHANISTIC ANALYSIS OF MICROTUBULE DYNAMICS AND REGULATION

by

ELISABETH ANNE GEYER

DISSERTATION / THESIS

Presented to the Faculty of the Graduate School of Biomedical Sciences

The University of Texas Southwestern Medical Center at Dallas

In Partial Fulfillment of the Requirements

For the Degree of

DOCTOR OF PHILOSOPHY

The University of Texas Southwestern Medical Center at Dallas

Dallas, Texas

December, 2018

ACKNOWLEDGEMENTS

It's hard to know exactly where to start, as there are so many people that have gotten me to this point today. But since I have to begin somewhere, I first want to thank my mentor and Ph. D. advisor, Luke Rice. Whether he knows it or not, meeting Luke during my interview weekend became one of the driving forces behind my decision to come to graduate school at UTSW. His excitement and passion for the science he does is infectious and I knew from my first week in his lab that I wanted to be a part of whatever he was selling. Luke's inability to accept complacency, thinking outside the box, asking the difficult questions, critically thinking about my data and analyses, and never being afraid to push me to try new things and question alternative ideas has shaped me into the scientist I am today. After having worked with Luke for six years, I feel ready to take on just about anything science has to offer me. There is really no proper way to thank Luke for all the lessons and opportunities he's given to me, but hopefully this little section was a start. I would also like to thank all the members of the Rice lab, both past and present, for helping me to navigate the unknown territory of grad school—and for providing a good bit of comic relief along the way!

Next, I want to thank my thesis committee, Drs. Khuloud Jaqaman, Michael Rosen and Hongtao Yu. Over the last six years, they've taken a considerable amount of time to meet with me, critically assess my data and my progress, and help to develop my projects and provide a fresh prospective on all of my work. I truly appreciate all of your time, effort and support on my graduate school journey (and beyond!).

Finally, I have to thank my family and friends, especially my parents, Karl and Lori, and my fiancée, Eric. To my parents: your constant love, encouragement, and guidance are the main reason that I'm where I am today and without it, I would be lost. Your support in all my

endeavors, even ones as crazy as moving to Texas for graduate school, mean more to me than I can express in this short section. Thank you for always listening to my melt downs, for sending lots of delicious home baked goods, and for providing me a non-science outlet that helps give me a better perspective on the world (and reminds me that life will go on, even when my experiments fail!). To Eric: thank you for being my rock, day in and day out. Your support and love, and constant reminders to take deep breaths when I'm stressed to the max, mean the world to me. I am so very lucky to have you by my side and can't wait to see where our journey takes us!

MECHANISTIC ANALYSIS OF MICROTUBULE DYNAMICS AND REGULATION

Publication No. _____

Elisabeth Anne Geyer, Ph.D.

The University of Texas Southwestern Medical Center at Dallas

Supervising Professor: Luke M. Rice, Ph.D.

ABSTRACT

Microtubules are critical components in a cells cytoskeletal network, known to form the mitotic spindle which allows for chromosome segregation and cell division and organizing the cytoplasm of non-dividing cells. The quick reorganization of the cytoskeleton relies heavily on the underlying behavior of microtubules, known as dynamic instability. Dynamic instability, the rapid switch between growing and shrinking states of the microtubule, depends on the functional GTPase behavior of the microtubule polymerizing subunits, αβ-tubulin. Recent studies have noted the presence of multiple conformational states of αβ-tubulin in the microtubule lattice, in addition to major conformational changes that occur in αβ-tubulin within the microtubule as

compared to free αβ-tubulin in solution. In Chapter 2, I will discuss a study in which I explored the role of the conformational cycle and its impact on microtubule dynamic instability. By studying a mutation in β-tubulin, T238A, I have shown that nucleotide hydrolysis and conformational changes in the lattice are tightly linked and provide allostery throughout the microtubule. Uncoupling the two cycles disrupts the allostery which greatly impacts the rapid transitions normally seen in dynamic instability that allow for fast and decisive structural rearrangements. In Chapter 3, I will discuss a study that aimed to dissect the molecular mechanisms of the yeast microtubule polymerase, Stu2p. In this project, I developed an all-yeast *in vitro* reconstitution system using total internal reflection fluorescence microscopy which enabled me to study a variety of Stu2 mutants, in the presence of wild-type and mutant yeast tubulin samples. Here, I discovered how the tubulin conformational state can impact Stu2 function and determined a new property of Stu2 in its ability recognize and bind either the microtubule lattice or free tubulin. From these findings, I have proposed a new alternating engagement mechanism to explain how Stu2 functions processively at the microtubule plus end to increase the growth rates of microtubules. Finally, in Chapter 4 I will summarize my work on both of these projects and discuss both future directions and preliminary results looking to solve the structure of human β:T238A microtubules using cryo-EM.

TABLE OF CONTENTS

PRIOR PUBLICATIONS

A tethered delivery mechanism explains the catalytic action of a microtubule polymerase. Ayaz, P.; Munyoki, S.; **Geyer, E. A**.; Piedra, F-A.; Vu, E. S.; Bromberg, R.; Otwinowski, Z.; Grishin, N. V.; Brautigam, C. A.; Rice, L. M. *eLife*. **2014**; 3: e03069

A mutation reveals allosteric control of microtubule dynamics by uncoupling the tubulin conformational and GTPase cycles. **Geyer, E. A**.; Burns, A.; Lalonde, B. A.; Ye, X.; Piedra, F-A; Huffaker, T. C.; Rice, L. M., *eLife*, **2015;** 4: e10113

May I check your cap? **Geyer, E. A*.;** Majumdar, S*.; Rice, L. M.; *eLife*, **2016**;5: e15570

GDP to GTP exchange on the microtubule end can contribute to the frequency of catastrophe. Piedra, F-A.; Kim, T.; Garza, E. S.; **Geyer, E. A**.; Burns, A.; Ye, X.; Rice, L. M.; *Molecular Biology of the Cell*, **2016**: mbc.E16-03-0199v1-mbc.E16-03-0199.

Direct measurement of conformational strain energy in protofilaments curling out from disassembling microtubule tips. Driver, J.; **Geyer, E.;** Bailey, M.; Rice, L.; Asbury, C.*; eLife*, **2017**, 6: e28433 DOI: 10.7554/eLife.28433

Structural differences between yeast and mammalian microtubules revealed by cryo-EM studies. Howes, S.C.; **Geyer, E. A**.; LaFrance, B.; Zhang, R.; Kellogg, E. H.; Westermann, S.; Rice, L. M.; Nogales, E.; J Cell Biol, **2017**, jcb.201612195; DOI: 10.1083/jcb.201612195

A tubulin binding switch underlies Kip3/Kinesin-8 depolymerase activity. Arellano-Santoyo, H.; **Geyer, E. A.*;** Stokasimov, E.*; Chen, G.Y.; Hancock, W.; Rice, L.M.; Pellman, D.; *Developmental Cell*, **2017**, Volume 42, Issue 1, 37 - 51.e8.

DOI: http://dx.doi.org/10.1016/j.devcel.2017.06.011

Structural and functional differences between porcine brain and budding yeast microtubules. Howes, S.C*.; G**eyer, E. A**.*; LaFrance, B.; Zhang, R.; Kellogg, E. H.; Westermann, S.; Rice, L. M.; Nogales, E.; Cell Cycle, **2018,** ISSN: 1538-4101 DOI: https://doi.org/10.1080/15384101.2017.1415680

Design principles of a microtubule polymerase. **Geyer, E. A.,** Miller, M., Brautigam, C. A., Biggins, S., Rice, L. M. *eLife*, **2018**, eLife 2018;7:e34574 DOI: 10.7554/eLife.34574

LIST OF FIGURES

LIST OF ABBREVIATIONS

γ-TuRC – gamma tubulin ring complex

Alp14 – Altered polarity protein 14

AUC – analytical ultracentrifugation

chTOG – Colonic and hepatic tumor over-expressed gene

DCX – Doublecortin

Dis1 – distorted trichomes 1

DMSO – dimethyl sulfoxide

EB1 – End-binding protein 1

EM – Electron microscopy

E-site – Exchangeable site

GDP – Guanosine diphosphate

GTP – Guanosine-5'-triphosphate

GTPγS - Guanosine 5'-O'[γ-thio]triphosphate

GMPCPP - Guanosine-5'-[(α,β)-methyleno]triphosphate

HEAT – Huntingtin, elongation factor 3, protein phosphatase 2A, and the yeast kinase TOR1

KCl – potassium chloride

MAP – Microtubule associated protein

MCAK – Mitotic centromere-associated kinesin

MT(s) – Microtubule(s)

N-site – Non-exchangeable site

PEG – polyethylene glycol

Stu1 – Suppressor of tubulin 1

Stu2 – Suppressor of tubulin 2

TOG – Tumor overexpressed gene

TLC - thin layer chromatography

VALAP - Vaseline, lanolin and paraffin

XMAP215 – Xenopus microtubule-associated protein 215

Zyg9 – Zygote defective protein 9

CHAPTER ONE

INTRODUCTION

Microtubule structure and function

Microtubules are essential components of the cytoskeleton

Since their discovery in the mid-20th century by Walther Flemming (Flemming, 1965), the structure and function of microtubules (MTs) has been a burgeoning topic of research and discovery. Microtubules serve a variety of purposes *in vivo*. In non-dividing cells, microtubules help to organize the cytoplasm, contribute to cellular morphogenesis and migration, and function as tracks for motor proteins as they transport cargo (Ganguly, Yang, Sharma, Patel, & Cabral, 2012; Hirokawa, Noda, Tanaka, & Niwa, 2009). In dividing cells, microtubules form the mitotic spindle, which allows for proper chromosome segregation and division into daughter cells (reviewed in (Inoue, 1981; Mitchison, Evans, Schulze, & Kirschner, 1986; Pickett-Heaps, Tippit, & Porter, 1982). Microtubules are major drug-targets because of their role in cellular division (Amos, 2011; Jordan & Wilson, 2004). To properly engage, orient and segregate chromosomes in a rapid and efficient manner, microtubules are highly dynamic and undergo very fast rates of assembly and disassembly (Desai & Mitchison, 1997). Many anti-cancer chemotherapies target microtubule dynamics. Paclitaxel, commonly known as taxol, is a widely used chemotherapy against a variety of cancers ranging from breast and ovarian to prostate and lung. Taxol binds to the microtubule lattice, functioning as an anti-mitotic drug by suppressing microtubule dynamics. These cells are rendered incapable of completing mitosis and will eventually undergo apoptosis (Jordan & Wilson, 2004).

Microtubules are polymers composed of αβ-tubulin

Microtubules are hollow, cylindrical polymers composed of obligate heterodimers of αβ-tubulin. Each heterodimer contains an individual α- and β- tubulin monomer, each having an approximate mass of 50,000 Daltons. αβ-tubulin heterodimers are highly conserved across eukaryotic species (Fygenson, Needleman, & Sneppen, 2004; Tuszynski et al., 2006)) and within a species (Burns, 1991)).

High-resolution crystal structures of αβ-tubulin have been solved, the majority in complex with a binding partner (Ayaz et al., 2014; Ayaz, Ye, Huddleston, Brautigam, & Rice, 2012; Gigant et al., 2000; Prota et al., 2014). These structures have shown that, consistent with the original structural findings from electron crystallography (Nogales, Wolf, & Downing, 1998), each of the compact tubulin monomers is composed of a core containing beta sheets enclosed in alpha helices. Distinct from the landmark structure solved in 1998 (Nogales et al., 1998), recent crystallographic structures reveal conformational changes in αβ-tubulin. In the first structure, the αβ-tubulin heterodimer is in a straight conformation. To align the tubulin monomers, all that is required is a simple translation (Figure 1.1, top). In all subsequent structures solved by x-ray crystallography, the αβ-tubulin dimer is in a curved conformation. In these structures, α- and β- tubulin are related to each other by a ~10-13° rotation (Figure 1.1, bottom). To align the tubulin monomers in the curved conformation, a 10-13° rotation and accompanying translation allow the subunits to overlay one another.

From biochemical and structural studies, it is known that both tubulin monomers bind a single guanine nucleotide (GDP or GTP) (Figure 1.2A). Binding of guanosine-5'-triphosphate (GTP) by α-tubulin occurs in a pocket near its binding interface with an accompanying β-tubulin. Because engagement with β-tubulin buries the GTP at the interface, this is a non-exchangeable

site (N-site). β-tubulin can bind either GTP or guanosine diphosphate (GDP) in a similar pocket at a solvent-exposed, exchangeable site (E-site) (Figure 1.2A).

Although both tubulin monomers share very similar structural architecture, subtle differences between α- and β-tubulin are evident in solved structures. Because αβ-tubulin dimers stack in a 'head-to-tail' fashion within each microtubule protofilament, these subtle structural differences in tubulin monomers give rise to an overall polarity within the microtubule lattice. The growing, dynamic end of the microtubule where β-tubulin is exposed is termed the plus-end of the microtubule; the less dynamic end of the microtubule where α-tubulin is exposed is termed the minus-end (Figure 1.2B). Minus-ends of microtubules in cells are typically capped by some type of nucleating or organizing center within the cell. By anchoring the minus-end of the microtubule to a microtubule organizing center, like the centrosome, the dynamic plus-end of the microtubule can more effectively explore the cytoplasm.

In order to create the microtubule lattice, αβ-tubulin dimers interact to form protofilaments by engaging in longitudinal associations. Tubulin heterodimers longitudinally interact 'head-to-tail' such that the β-tubulin of a prior heterodimer will engage the α-tubulin of a newly incoming heterodimer (Figure 1.2C). Lateral associations between protofilaments result in formation of the canonical 'barrel-like' microtubule lattice. This creates a cylindrical polymer structure that has an inner diameter of approximately 25 nm. Most commonly, microtubules consist of 13 protofilaments *in vivo* (reviewed in Desai and Mitchison, 1997) where all of the protofilaments are parallel to the microtubule axis. The number of protofilaments in a microtubule can vary from 11-16 protofilaments both *in vivo* and *in vitro*. Factors that affect the number of protofilaments in the microtubule include: the type of guanine nucleotide bound to tubulin (further explanation below) (Hyman, Chretien, Arnal, & Wade, 1995), the presence of

drugs (Diaz, Valpuesta, Chacon, Diakun, & Andreu, 1998), tubulin homologues from different species (Howes et al., 2017) or a host of regulatory proteins in the cell (Bechstedt & Brouhard, 2012; Zhang, Alushin, Brown, & Nogales, 2015). Changes in protofilament number alter the skew angle and curvature of the lattice, which can affect microtubule dynamics, function and interaction with microtubule associated proteins (MAPs) (Pampaloni & Florin, 2008; Wade, Chretien, & Job, 1990).

Within the lattice, the majority of lateral contacts between tubulin heterodimers are homotypic, such that α-tubulin interacts with α-tubulin, and β-tubulin interacts with β-tubulin. For a 13-protofilament microtubule, the only place where these lateral contacts are disturbed is at the microtubule seam (Figure 1.2B). Here, lateral contacts become heterotypic, such that α-tubulin interacts with β-tubulin. While the function of the seam has been a constant area of question and research, its role still remains ambiguous in relation to microtubule dynamics.

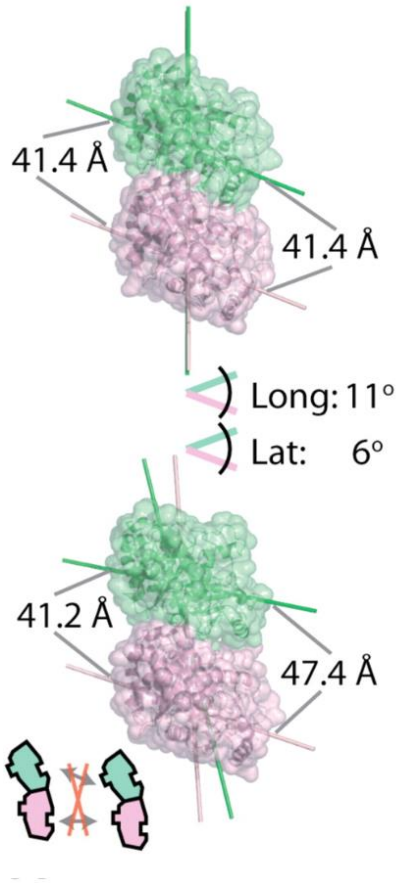

Figure 1.1: αβ-tubulin can exist in two conformational states. Figure and legend is reproduced from (Rice, Montabana, & Agard, 2008). In the straight conformation of tubulin (top, PDB 1JFF), both the longitudinal and lateral polymerization interfaces are aligned. In the curved conformation (bottom, 1SA0), the α- and β-tubulin protofilaments and lateral interaction axes are skewed by 11° and 6°, respectively; these rearrangements separate equivalent laterally interacting atoms by up to 6Å. (*Inset)* This misalignment of interfaces destabilizes lateral interactions between curved αβ-tubulins.

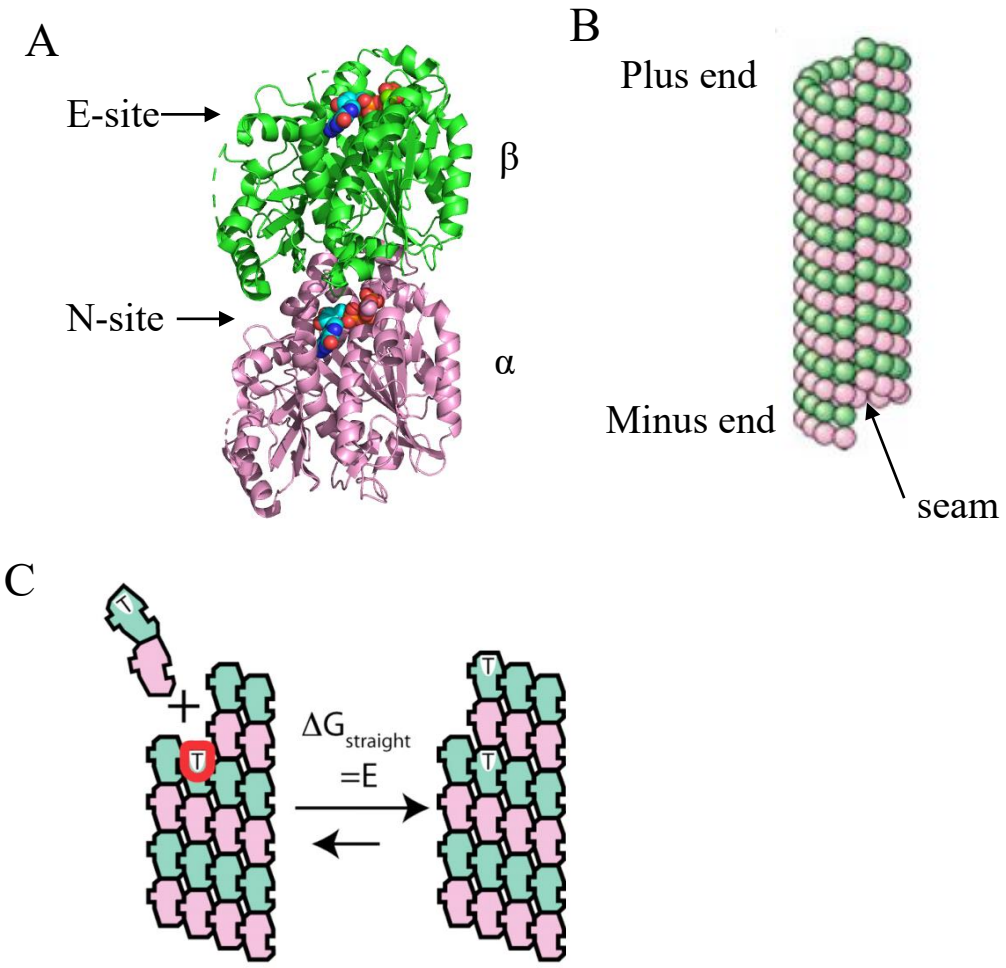

Figure 1.2: Properties of αβ-tubulin heterodimers and their influence on microtubule structure and polymerization. A. The structure of yeast tubulin (PDB code 4FFB, TOG1 domain removed for clarity) reveals that tubulin heterodimers bind GTP molecules at unique sites. In β-tubulin (green subunit), GTP binds at an exchangeable, E-site; in α-tubulin (pink subunit), GTP binds at the buried interface directly under β-tubulin, known as the nonexchangeable N-site. B. Tubulin dimers stack in a 'head to tail' manner in the microtubule creating a polar microtubule marked by differences at the ends: β-tubulin (green) is exposed at the plus-end while α-tubulin (pink) is exposed at the minus end. In cells, minus ends are typically capped by a nucleating structure, such as the centrosome. C. Figure and legend are reproduced from (Rice et al., 2008). Unpolymerized αβ-tubulin remains curved even when bound to GTP. Incorporation into the lattice requires unfavorable domain rearrangements (ΔGstraight = E). The lattice-acting GTP (circled in red) provides stronger lattice contacts to stabilize the MT-bound straight conformation.

Dynamic instability is influenced by nucleotide hydrolysis and conformational changes

It was originally thought that the behavior of microtubules was attributed to a property known as 'treadmilling' (Margolis & Wilson, 1978): growth of the microtubule by addition of tubulin subunits at the plus-end of the polymer competed with the loss of tubulin subunits at the minus-end of the polymer. In this way, the microtubule was simultaneously growing and disassembling. Landmark discoveries made by Mitchison and Kirschner (Mitchison & Kirschner, 1984a, 1984b) later demonstrated that the primary behavior of microtubules is not treadmilling but rather a non-equilibrium state known as dynamic instability. Since this discovery, the underlying features that contribute to microtubule dynamic instability have been a growing topic of interest in the field to more accurately understand the mechanistic behavior of these polymers.

Dynamic instability is the rapid switch between growth and rapid disassembly. Two terms define the core of dynamic instability: catastrophe, the switch from growth to shrinking, and rescue, the switch from shrinking back to a growing state (Figure 1.3). To meet the ever-changing needs of the cellular environment, microtubules must be highly dynamic. The function of dynamic instability allows the microtubule cytoskeleton to rapidly disassemble and reorganize. This prevents the microtubule cytoskeleton from being confined in one area of the cell because the polymer can rapidly turnover to solution-state tubulin. Over the years it has been shown that dynamic instability is predominantly controlled by two processes related to the tubulin heterodimer: a nucleotide cycle and a conformational cycle.

Each tubulin monomer within the heterodimer binds its own molecule of GTP; α-tubulin binds a GTP at its N-site site while β-tubulin binds a GTP molecule at its E-site. Only GTP-bound tubulin dimers are capable of entering the polymer at the growing and dynamic plus-end

(Figure 1.3). A productive tubulin binding event occurs at the plus-end when a GTP-bound tubulin successfully incorporates into the lattice. These events tend to be rare and lead to slow growth because the binding affinity of free tubulin to the microtubule is relatively low: longitudinal contacts are estimated to be on the order of micromolar, while lateral contacts are estimated to be on the order of millimolar to molar (Gardner et al., 2011; Piedra et al., 2016). This newly bound tubulin will, presumably, initially form longitudinal contacts and then eventually lateral contacts. It is only after another tubulin dimer binds directly atop the first, completing the GTP hydrolysis pocket with the incoming α-tubulin subunits, that GTP hydrolysis will occur. Buried tubulins within the lattice will all undergo GTP hydrolysis at the E-site during the course of growth. This creates a highly unstable GDP-microtubule core. As the microtubule grows, a layer of GTP-bound tubulins that has not yet undergone hydrolysis act as a 'stabilizing GTP cap', preventing the microtubule from undergoing disassembly. Due to pause events during growth or a decrease in the growth rate, GTP hydrolysis can erode through the stabilizing GTP cap. Loss of the stabilizing GTP cap results in catastrophe, which leads to rapid disassembly of the microtubule. Disassembly releases the now GDP-bound tubulin dimers back into solution, where they can undergo nucleotide exchange of GDP for GTP. Tubulin dimers that have exchanged their nucleotide and are now bound to GTP are capable of re-entering the polymerization cycle.

Based on x-ray crystallography and cryo-EM structures, it has been shown that tubulin 'changes shape' as it enters and exits the microtubule lattice. In solution, crystal structures have shown that tubulin exists in a curved conformation, where α- and β-tubulin are related to each other by ~13° rotation (previously described, see Figure 1.1). To enter the microtubule lattice, the tubulin dimer must 'straighten' out. Cryo-EM structures have shown that tubulin dimers are

in a straight conformation in the microtubule lattice, where α- and β- tubulin sit almost exactly atop one another. In the next section, I will discuss how recent high-resolution cryo-EM structures have revealed multiple lattice conformations of tubulin. These structures have stirred new questions as to the function of the tubulin conformational cycle and its role in regulating dynamic instability.

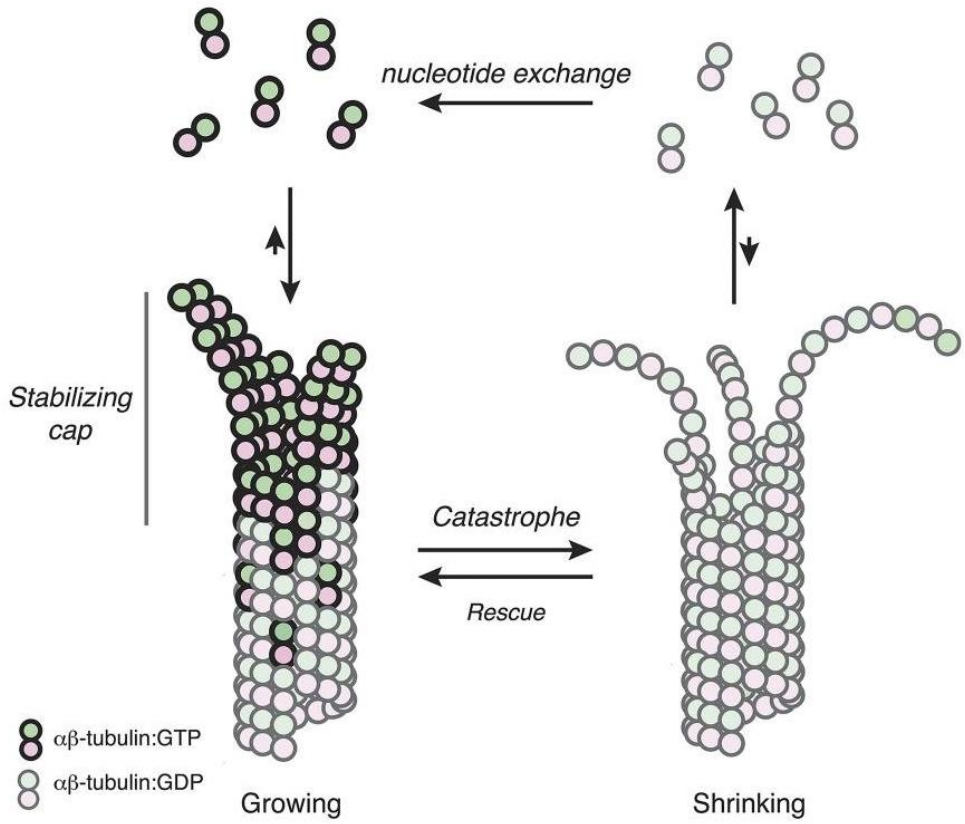

Figure 1.3: The cycle of microtubule polymerization. Figure and legend are reproduced from (Brouhard & Rice, 2014). Microtubules are hollow cylindrical polymers composed of αβ-tubulin subunits. Microtubule polymerization occurs through the addition of GTP-bound αβ-tubulin subunits onto microtubule ends. Growing microtubule ends show outwardly curved, tapered, and flattened end structures, presumably reflecting the conformational changes that occur during polymerization. The addition of a new subunit completes the active site for GTP hydrolysis, and consequently most of the body of the microtubule contains GDP-bound αβ-tubulin. The GDP lattice is unstable and protected from depolymerization by a stabilizing "GTP cap", an extended region of newly added GTP- or GDP.Pi-bound αβ-tubulin. The precise nature of the microtubule end structure and the size and composition of the cap are a matter of debate. Loss of the stabilizing cap leads to rapid depolymerization, which is characterized by an apparent peeling of protofilaments. "Catastrophe" denotes the switch from growth to shrinkage, and "rescue" denotes the switch from shrinkage to growth.

Understanding the role of the conformational cycle

Recent advances in data collection and processing in cryo-EM have allowed for the possibility to solve high-resolution (sub 4Å) structures of microtubules (Alushin, et al., 2014) which have yielded landmark discoveries regarding the conformational states of tubulin. While it had been known that tubulin changes conformation throughout the polymerization cycle, prior to the determination of these high-resolution lattice structures, it was simply though that tubulin *only* existed in either a curved or straight conformation. Work from the Nogales lab (Alushin et al., 2014; Zhang et al., 2015) has recently revealed that there are actually *multiple* conformational states of tubulin within the microtubule lattice. To probe the 'GTP-bound' state of the microtubule lattice, the Nogales lab solved structures bound to GMPCPP; to probe the 'GDP-bound' state, they solved microtubule structures incubated with GTP and allowed to polymerize for a short time (Alushin et al., 2014).

Comparisons of these structures revealed that in the GTP-state, tubulin exists in an expanded, straight conformation analogous to previously solved low-resolution structures of microtubules. However, in the GDP-bound state, compression of α-tubulin at the interdimer interface near the E-site was now visible, resulting in a new tubulin conformational state: compacted (Alushin et al., 2014). Additional structures solved by the Nogales lab have also shown that in the presence of guanosine 5'-O'[γ-thio]triphosphate (GTPγS), a non-hydrolyzable GTP-analog, tubulin conformation is not only compacted, but there is a small twist in the lattice (Zhang et al., 2015) (Figure 1.4). This new compacted/ twisted intermediate state is of great interest to those trying to understand the intricate details of dynamic instability, because GTPγS is believed to closely mimic the GDP-Pi nucleotide state. In summary, four distinct conformational states of tubulin are currently known in atomic detail. These include the curved

conformation in solution, and three lattice conformations: expanded in the GTP-state, compacted in the GDP-state and compacted/twisted in the presumed GDP-Pi state.

These recent discoveries of new conformational states of tubulin have created new questions surrounding the function of the conformational cycle and its role in regulating dynamic instability. While it has long been understood that dynamic instability is dependent on the GTPase activity of αβ-tubulin, what remains to be answered is correlation between GTPase activity and these newly determined conformational states. Does the conformational cycle contribute to microtubule dynamics? Are these 'shape changes' simply a by-product of GTPase activity that really plays no role in regulating dynamic instability? If changes in conformation are tightly linked to different nucleotide hydrolysis states, could this induce some type of allostery in the lattice? If so, how 'far' does the allostery reach: do tubulin dimers only influence those in contact with them, or can conformational changes induced by hydrolysis have further reaching effects in the context of the lattice? I will explore these questions, in regards to the role of the conformational cycle of tubulin, in Chapter 2.

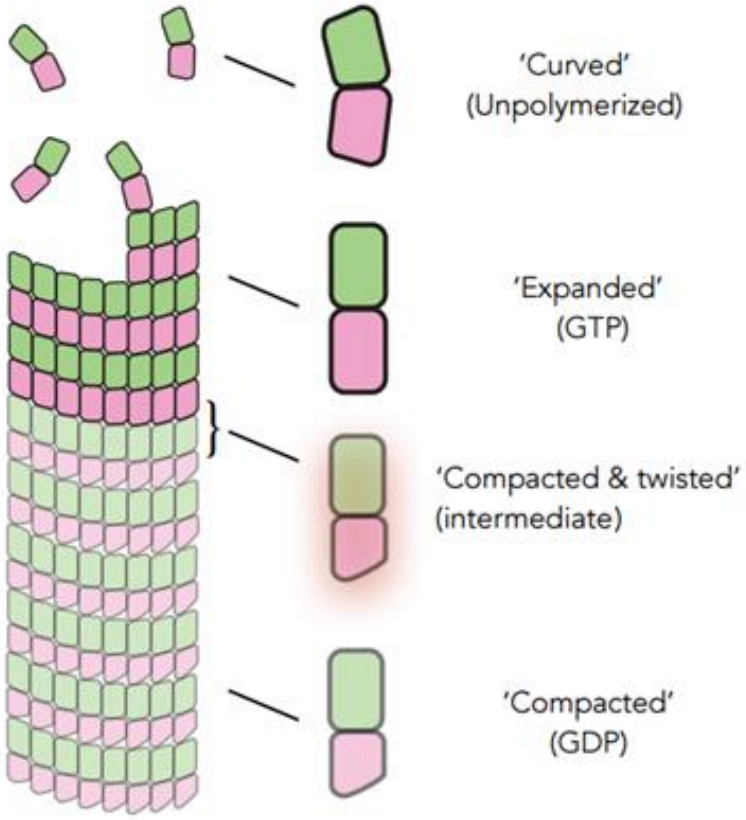

Figure 1.4: Conformational states of tubulin dimers through the polymerization cycle. In solution, tubulin is in a 'curved' conformation. αβ-tubulin cycles through various 'straight' states while in the microtubule lattice. When bound to GTP near the polymer end, tubulin exists in an 'expanded' state. Current structures have revealed that tubulin, over the course of GTP hydrolysis, undergoes a slight upward compaction of the α-tubulin subunit and dimer twist which is referred to as a 'compacted & twisted' state. This state is believed to be correlated to a GDP-Pi intermediate state that is still unknown. After hydrolysis has completed and tubulin is bound to GDP, it remains compacted in the α-subunit but no longer has an accompanying twist, referred to as the 'compacted' state.

Factors that Regulate Microtubule Dynamics

Perturbing dynamic instability using tubulin mutants

Dynamic instability relies heavily on both a functional GTPase cycle of tubulin and the ability of tubulin dimers to properly transition through conformational changes as they enter and exit the microtubule polymer. Perturbing each of these cycles independently would allow for a deeper understanding into the underlying mechanisms of how they tune dynamic instability, as well as how the two cycles are interconnected. Historically, experiments probing the effects of altering the GTPase cycle have relied on the use of non-hydrolyzable GTP-analogs, such as guanosine-5'-[(α,β)-methyleno]triphosphate (GMPCPP) and GTPγS, to eliminate hydrolysis. Microtubules are still capable of growing in these GTP-analog conditions (Hyman, Salser, Drechsel, Unwin, & Mitchison, 1992). These polymers, however, are resistant to catastrophe and, under *in vitro* experimental conditions, do not measurably shrink. While these types of nucleotides are useful where stable microtubules are desired, they cannot be used to explore how altering the rate or release of GTP will affect the switch to catastrophe or shrinkage rates. Another major area of interest is the impact of modifying the conformational cycle of tubulin. One could imagine that altering the ability of tubulin to 'change shape' or changing the rate at which GTP hydrolysis occurs could expose a deeper understanding into the mechanism of dynamic instability.

The optimal way to approach these mechanistic questions would be by creating tubulin mutants that would selectively perturb either the nucleotide or conformational cycle. As the primary source of tubulin used in most labs studying the microtubule cytoskeleton comes from cow or pig brains, purifying tubulin directly from animal brains is convenient but also has significant implications, one of the largest being the inability to make and study tubulin mutants.

Others include sample heterogeneity, differences in isotypes and differences in post-translational modifications on the flexible C-terminal 'E-hook' tubulin tails. To circumvent this issue, many have instead studied the effects of tubulin mutants *in vivo*, typically using yeast genetic screens (Stearns, Hoyt, & Botstein, 1990; Thomas, Neff, & Botstein, 1985). These genetic screens have provided a wealth of information surrounding the characterization of tubulin *in vivo*, but frequently the read out on these screens are either cell survival or cell death. Cell death or survival does not provide an accurate picture as to how the mutant affects the microtubule cytoskeleton. Determining how a tubulin mutant could directly impact microtubule dynamics would require being able to isolate pure tubulin *in vitro* to allow for quantitative measurements to be made on dynamics, correlating perturbations in tubulin with changes in dynamic instability.

Our lab works primarily with tubulin from *Saccharomyces cerevisiae*, commonly known as budding yeast tubulin, which brings a unique advantage to be able to isolate yeast tubulin mutants. We can introduce mutations into either α- or β-tubulin and selectively purify these tubulin mutants using affinity protein purification methods, by over-expressing yeast tubulin on inducible plasmids in their native background. Over the years, our lab has produced a number of tubulin mutants that have allowed us to explore a range of topics. Studying a mutation at the GTP-binding pocket of β-tubulin, C12A, revealed the impact of nucleotide exchange on the microtubule end in relation to catastrophe frequency (Piedra et al., 2016), while use of longitudinal polymerization-blocking mutations on either α- or β-tubulin have allowed for further discovery into polymerization dynamics (Johnson, Ayaz, Huddleston, & Rice, 2011) as well as the first crystal structures of a tubulin dimer bound to tumor overexpressed gene (TOG) domains from the microtubule polymerase, Stu2p (Ayaz et al., 2014; Ayaz et al., 2012) (Figure 1.5). Given our experience in studying tubulin mutants, and coupled with the new structures of

microtubules that have elucidated different states in the tubulin conformational cycle, is it possible to identify some type of tubulin mutant that could selectively perturb the conformational cycle? Using a previously identified mutation in β-tubulin, I will discuss our findings into the role of the conformational cycle and its interplay with the nucleotide hydrolysis cycle in Chapter 2.

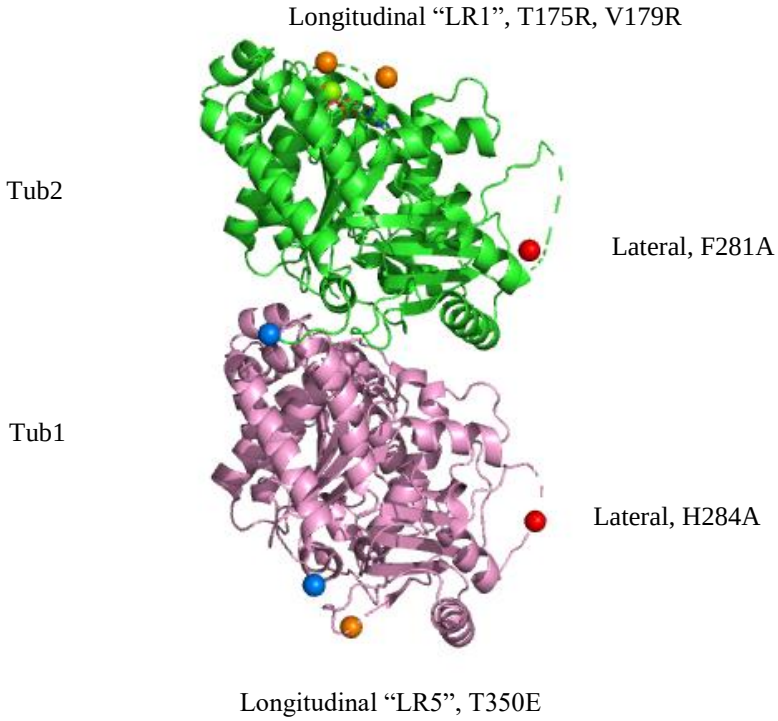

Figure 1.5: Cartoon representation of point mutations that have been studied in yeast tubulin. The structure of Stu2:TOG1 bound to yeast αβ-tubulin (α-tubulin in pink and β-tubulin in lime; PDB code 4FFB) is shown in cartoon representation, with the TOG1 domain having been removed for clarity. Red spheres indicate the position of the interface perturbing mutations on the lateral interaction surfaces (α: H284A, β: F281A). Orange spheres indicate the position of longitudinal blocking mutations on the plus-(β:T175R,V179R) or minus-end (α:T350E) of tubulin. Blue spheres indicate the approximate location of the start of the negatively charged, unstructured C-terminal tails of α- and β-tubulin.

Microtubule associated proteins (MAPs) in the cell can influence microtubule dynamics and structure.

Tubulin is capable of forming microtubule polymers *in vitro* in the absence of any additional binding partners: all that is required for controlled polymerization is buffer, excess GTP and a seeding substrate. However, in the cell, tubulin never exists by itself. Tubulin dimers, and microtubules, are in constant contact with hundreds of additional proteins, some of which are capable of altering dynamic instability. Proteins in the cell that impact microtubule structure and function are known as MAPs, or microtubule associated proteins. MAPs exhibit a wide-range of function. End-binding protein 1 (EB1) is a MAP that is capable of recognizing and binding to a specific conformational state, the compacted/twisted region, of the microtubule lattice (Duellberg, Cade, Holmes, & Surrey, 2016). Once bound, EB1 accelerates the rate of GTP hydrolysis leading to an increase in the catastrophe frequency (Maurer et al., 2014; Maurer, Fourniol, Bohner, Moores, & Surrey, 2012). Some MAPs, like mitotic centromere-associated kinesin (MCAK), are depolymerizing proteins that bind selectively to curved tubulin dimers with such high affinity that they elicit removal of tubulin from the microtubule end leading to microtubule depolymerization (Cooper, Wagenbach, Asbury, & Wordeman, 2010; Helenius, Brouhard, Kalaidzidis, Diez, & Howard, 2006) (Figure 1.6A). Another MAP, Doublecortin (DCX), preferentially binds the microtubule end where it is capable of stabilizing the curved conformational of tubulin found at the very microtubule tip (Bechstedt & Brouhard, 2012) (Figure 1.6B). One family of MAPs, XMAP215/Dis1/Stu2, is a family of microtubule polymerases that have been shown to increase rates of microtubule polymerization five-fold *in vitro* (Figure 1.6B) (Brouhard et al., 2008; Widlund et al., 2011). I am interested in understanding the mechanisms of these polymerases, particularly in regards to Stu2. Co-crystal

structures of the TOG domains of Stu2 with yeast tubulin have revealed that the TOG domains bind tubulin dimers in a conformation-selective manner (Ayaz et al., 2014; Ayaz et al., 2012). I aim to dissect the underlying molecular mechanism of Stu2 function to gain insight into how this polymerase family can interact with both tubulin and the microtubule lattice to allow for an increase in polymerization rates.

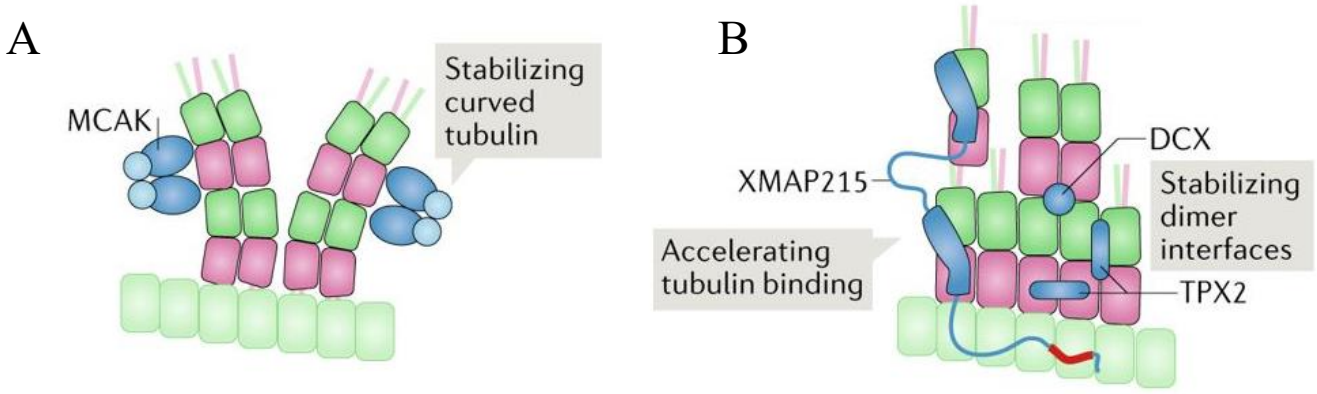

Figure 1.6: MAPs regulate microtubule dynamics by performing a variety of functions. Figure and legend reproduced from (Brouhard & Rice, 2018). A. The depolymerizing kinesin motor MCAK tightly binds the highly curved conformation of tubulin at the microtubule ends. By stabilizing this conformation, MCAK is able to depolymerize the microtubule lattice through dissociation with tubulin dimers. B. XMAP215, a microtubule polymerase, and DCX, a neuronal migration protein, both recognize the curved tubulin dimers at the plus-end of the lattice. XMAP215 (with only two of its TOG domains cartooned) increases the growth rates of microtubules by rapid addition of free tubulin dimers to the end of the lattice. DCX stabilizes tubulin:tubulin interactions at interfaces between dimers at the plus-end of the polymer.

XMAP215/Stu2 Family Polymerases

The XMAP215/Stu2 family of polymerases are essential proteins that increase the growth rates of microtubules

The evolutionarily conserved proteins in the XMAP215/Stu2 family regulate microtubule dynamics by accelerating the growth of microtubules *in vivo* and *in vitro* (Brouhard et al., 2008; Podolski, Mahamdeh, & Howard, 2014). These polymerases are found in multiple eukaryotic organisms including: *Xenopus laevis* XMAP215, *Caenorhabditis elegans* Zyg 9 (Zygote defective protein 9), human Colonic and hepatic tumor over-expressed gene (ch-TOG), *Schizosaccharomyces pombe* Alp14 (Altered polarity protein 14) and Dis1 (Distorted trichomes 1), and *Saccharomyces cerevisiae* Stu2 (Al-Bassam & Chang, 2011). The higher eukaryotic members, such as ch-TOG, XMAP215 and Zyg-9, are monomeric proteins, while the lower eukaryotic members, such as Dis1 and Stu2, are dimeric proteins. All members in this family, regardless of dimerization state, have a very similar structural architecture. This architecture consists of multiple tubulin-binding TOG domains, followed by an SK-rich basic domain region and a flexible C-terminal tail (Figure 1.7). The TOG domains are small, helical proteins that each contain six HEAT (Huntingtin, elongation factor 3, protein phosphatase 2A, and the yeast kinase TOR1) repeats, forming a flat 'paddle-like' interaction surface (Al-Bassam, Larsen, Hyman, & Harrison, 2007). Dimeric proteins, like Stu2, also have a coiled-coil region that follows the basic domain to allow for homodimerization (Figure 1.7).

Stu2 is an essential protein in yeast: degradation of Stu2 results in cell death (Ayaz et al., 2014; Wang & Huffaker, 1997). Although loss of function or knockdown of Stu2 in cells has lethal effects, it remains to be understood as to what the primary function of Stu2 is in the cell such that loss of Stu2 leads to apoptosis. While many view the function of Stu2 as a microtubule

polymerase, localization of Stu2 in the cell complicates this picture. Stu2 has been shown to tightly bind the growing microtubule plus-end, but it has also been shown to localize at kinetochore-microtubule attachment sites and microtubule organizing centers (MTOCs) (Miller, Asbury, & Biggins, 2016; Wang & Huffaker, 1997). Loss of Stu2 *in vivo* results in a decrease in growth rates of microtubules, abnormalities in the formation of the mitotic spindle and noticeable decreases in the elongation of microtubules from kinetochores (Gard & Kirschner, 1987; Tang, Takada, Hsu, & Toda, 2013; Wang & Huffaker, 1997). Recent studies have even started to reveal new functions for this polymerase family as potential potent microtubule nucleators that work in complex with the γ-tubulin ring complex (γ-TuRC) to help give rise to new microtubules in the cell (Thawani, Kadzik, & Petry, 2018).

In vitro characterization of XMAP215 has revealed critical insights into the mechanism of this polymerase family. Thorough biochemical characterization using *in vitro* reconstitution systems revealed that XMAP215 functions as a catalyst, increasing the rates of microtubule elongation five-fold above tubulin-only control measurements (Brouhard et al., 2008). When tubulin is in excess, XMAP215 or Stu2 are known to function as polymerases, such that they increase growth rates by adding tubulin dimers to the microtubule lattice. When tubulin is in sub-stoichiometric ratios to XMAP215 or Stu2, these proteins can function in 'reverse' and work to depolymerize stabilized microtubules by removing tubulin dimers from the microtubule ends (Geyer et al., 2015; Podolski et al., 2014). In this way, the catalytic activity of this family relies on their behavior to not only sense their local tubulin environment but to recognize and track the growing microtubule end, further distinguishing this family as 'tip-tracking' proteins. XMAP215 acts as a processive polymerase: once bound at the microtubule end, XMAP215 performs multiple cycles of tubulin addition over a period of seconds on the growing

microtubule end before it diffuses into solution (Brouhard et al., 2008). Structurally, XMAP215 requires a minimum of two TOG domains to retain its polymerase function, even though the native monomeric protein contains a total of five TOG domains (Widlund et al., 2011). Many details about the function of this protein family have been uncovered, primarily by studying XMAP215 with the use of *in vitro* reconstitution systems. However, a detailed molecular mechanism to wholly characterize the functional aspects of this protein family still remains unsolved. Differences between XMAP215 and lower eukaryotic homologues, specifically Stu2, elucidate a new set of questions that surpass the general function of this protein family. Stu2 is homodimeric with two TOGs on each monomer arm that are linked through a 72 amino acid flexible linker. XMAP215 is monomeric with five TOGs in a linear strand. Stu2 acts as a polymerase primarily on yeast tubulin, while XMAP215 is a functional polymerase on both animal and yeast tubulin (Podolski et al., 2014). Addressing these differences will help to develop a more complete molecular picture to explain the molecular activity of this protein family.

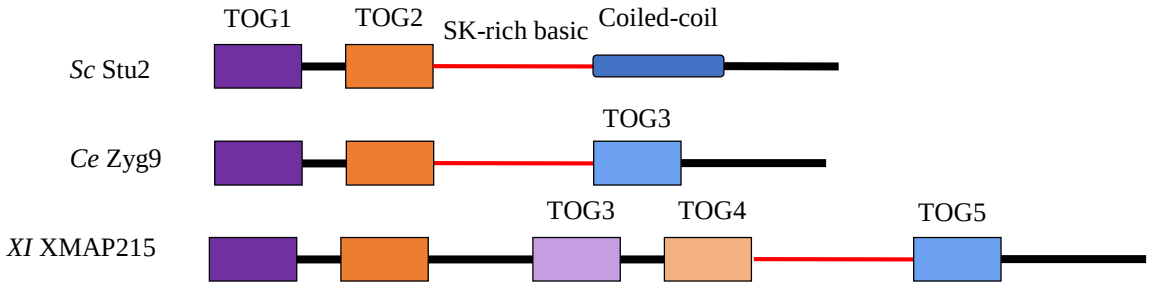

Figure 1.7: Domain architecture of the XMAP215/Stu2 family of proteins. Stu2 and lower yeast homologues are dimeric proteins composed of two, N-terminal TOG domains (TOG1 in purple and TOG2 in orange) linked by a 72 amino acid flexible linker, followed by an SK-rich basic domain (red), coiled coil domain (blue barrel) and flexible C-terminal tail (black). Higher eukaryotic homologues, like Zyg9 and XMAP215, are monomeric and contain multiple TOG domains (Zyg 9: TOG1, TOG2, TOG3 in light blue; XMAP215: TOG1, TOG2, TOG3 in light purple, TOG4 in light orange, TOG5 in light blue), an SK-rich basic domain between their final two TOG domains, and a flexible C-terminal tail (black).

Stu2 contains two N-terminal TOG domains that selectively bind curved tubulin dimers with high affinity

Crystallization of proteins bound to free tubulin dimers has been challenging because of the intrinsic property of tubulin heterodimers to self-assemble. While trying to get high enough yields to grow sizeable crystals, animal-purified tubulin, such as bovine and porcine, readily form polymers. This prevents crystallization of the desired complex. Working with yeast tubulin, rather than animal, presents a unique opportunity to gain access to crystal structures of tubulin that were previously unsolvable. By introducing longitudinal blocking mutations (described in the previous section) that prevent yeast tubulin from polymerizing, co-crystal structures of each of the N-terminal TOG domains of Stu2, TOG1 and TOG2, bound to a yeast tubulin heterodimer (Ayaz et al., 2014; Ayaz et al., 2012) were able to be solved (Figure 1.8A).

These structures have revealed several new insights into TOG: tubulin binding. Prior to the determination of these structures, it was argued that multiple TOG domains would engage a single tubulin dimer and cooperatively shuttle it to the microtubule end (Al-Bassam, van Breugel, Harrison, & Hyman, 2006). Both TOG structures, however, reveal that a multiple TOG:tubulin mechanism is not possible. TOG1 and TOG2 exclusively bind their own curved tubulin heterodimer through interactions of two key residues: a tryptophan (W23 in TOG1, W341 in TOG2) that engages β-tubulin subunit through hydrophobic interactions, and an arginine (R200 in TOG1, R519 in TOG2) that contacts the α-tubulin subunit using electrostatic interactions (Figure 1.8A). Mutation of these residues prevents either TOG domain from binding tubulin with high affinity (Ayaz et al., 2014). Docking either TOG domain onto a straight tubulin dimer reveals that binding of both TOGs are only compatible to a curved tubulin dimer (Figure 1.8B); engaging a straight tubulin dimer forces the TOG domain to compromise either

binding site, as the structure reveals that both the tryptophan and arginine residues simultaneously engage both α- and β-tubulin. Biochemical characterization of the TOGs show that they bind free tubulin with high affinity (low nanomolar, nM, regime). Both TOG domains bind with similar affinity, but TOG1 binds tubulin with approximately two-fold tighter affinity than TOG2 (~70 nM for TOG1 versus ~150 nM for TOG2) (Figure 1.8C).

Biochemically and structurally both TOG domains of Stu2 appear to be very similar and possibly interchangeable. This was further evidenced with *in vivo* experiments. Yeast genetic rescue assays allow for inducible depletion of native Stu2. The cells will die if no 'rescuing' Stu2 construct is transformed into the cells. When dimeric or monomeric constructs are transformed into the cells, cell proliferation provides an assessment as to the function of the transformed Stu2 variant. Yeast cells are rescued with high viability in the presence of either monomeric or dimeric Stu2 constructs. In the background of a Stu2 dimer, replacing the native TOG1 with TOG2, or mutating the tubulin binding residues in either TOG1 or TOG2 has little no effect on cell viability (Figure 1.9, left). Mutations in TOG1 or TOG2 abolish rescue activity when they are made in monomeric Stu2 constructs (Figure 1.9, right). These data are consistent with previous findings of XMAP215 that demonstrate the need for two functional TOG domains. They also point to the idea that the TOG domains appear interchangeable, consist with biochemical and structural findings *in vitro*.

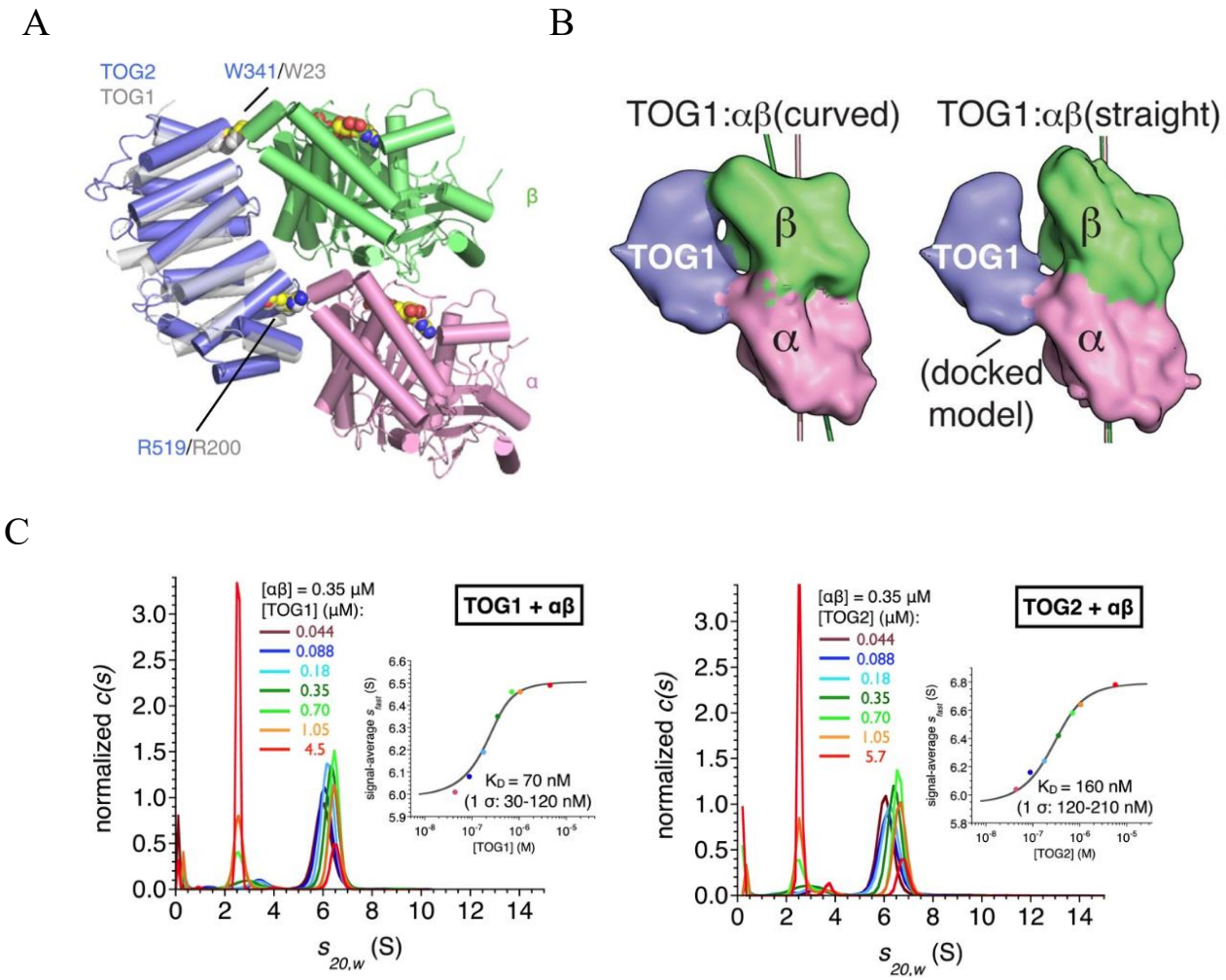

Figure 1.8: Biochemical and structural characterization of Stu2 TOG domains. Figures A and C were reproduced from (Ayaz et al., 2014), figure B was reproduced from (Ayaz et al., 2012). A. Co-crystal structures of TOG1 (silver) and TOG2 (purple) bound to yeast αβ-tubulin heterodimer. Two key residues are critical to this interaction: W23 (TOG1)/W341 (TOG2) and R200 (TOG1)/R519 (TOG2. B. Docking the TOG1 structure onto a straight αβ-tubulin reveals lack of engagement to both critical binding sites. C. Analytical ultracentrifugation sedimentation equilibrium experiments show that TOG1 binds αβ-tubulin with 70 nM affinity (left) while TOG2 binds αβ-tubulin with 160 nM affinity (right). The inset plots show a fit to a 1:1 binding isotherm of the signal average, s_{fast}.

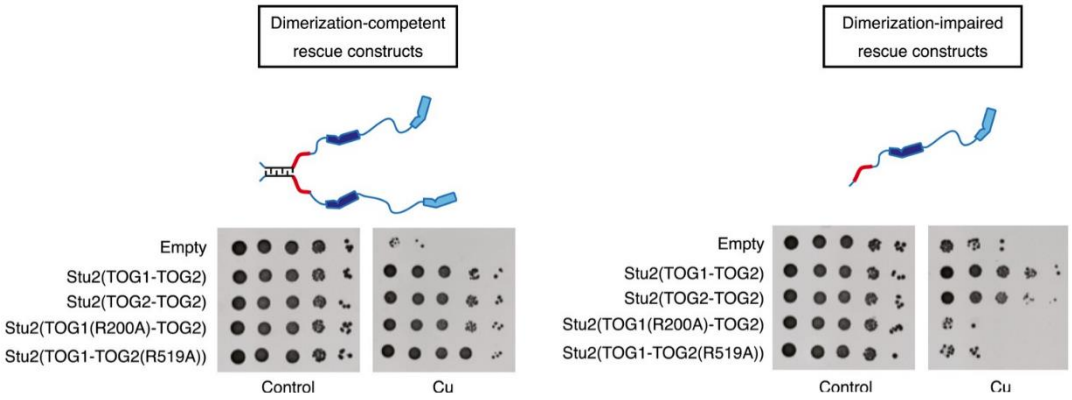

Figure 1.9: Yeast genetic rescue assays show that Stu2 requires a minimum of two functional TOG domains to allow for robust cell viability. Figure is reproduced from (Ayaz et al., 2014). Stu2 does not require different types of TOG domains, as mutating either TOG1 or TOG2, or swapping the native TOG1 for a TOG2 in the dimeric construct (left) does not affect cell rescue. Stu2 does require at least two functional TOG domains, as mutating either TOG domain in the background of monomeric Stu2 (right) results in cell death.

An early model to explain Stu2 polymerase function

Based on these data, an initial 'tethering' mechanism to explain Stu2 function was proposed (Figure 1.10). In the absence of Stu2, additions of tubulin at the microtubule end occur inefficiently (Figure 1.10, first panel starting from left). Dimers dissociate much more rapidly than they successfully associate because tubulin dimers bind the end of the microtubule with weak affinity, usually only engaging with a single longitudinal bond. This leads to non-productive, slow microtubule growth. In the presence of Stu2, one of the TOG domains, possibly the more C-terminal TOG2, is able to stabilize a weakly-bound tubulin dimer at the microtubule end to prevent its dissociation. The remaining TOG, possibly the more N-terminal TOG1, is able to search in solution to bind and sequester free-tubulin dimers and bring them back to the microtubule end (Figure 1.10, second panel). The 'searching' TOG domain can bring its tubulin back to the microtubule end, possibly interacting with the already weakly-bound tubulin dimer (Figure 1.10, third panel). Lateral associations between the two tubulin dimers help to drive the conformational transitions into the straight state, which would result in release of the TOG domains (Figure 1.10, fourth panel). The polymerase is then able to repeat this process with a new round of tubulin dimers. This 'tethering' mechanism works to concentrate tubulin dimers near the growing plus-end, leading to more efficient and rapid polymerization. Because the TOGs are physically linked through their 72 amino acid flexible linker, this type of mechanism could be thought of as analogous to a paddle ball: one TOG domain remains 'stuck' on the microtubule end, while the other can 'bounce' back and forth between the end of the microtubule, to deliver a tubulin, and the surrounding solution, where it can bind free tubulin as it 'reloads'.

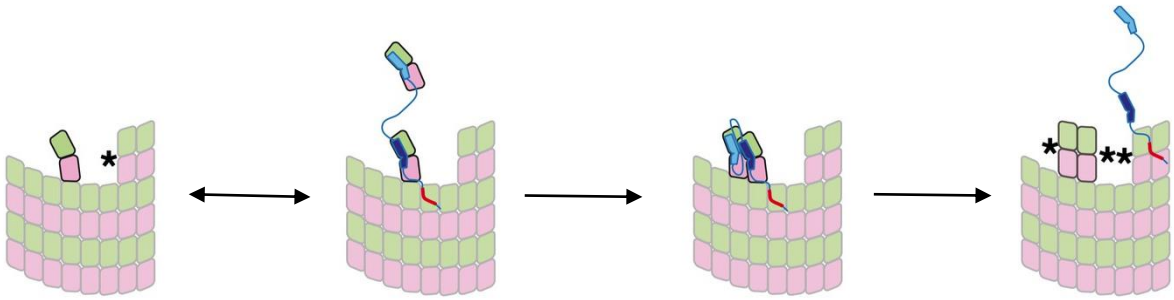

Figure 1.10: Cartoon illustrating the tethering mechanism of Stu2 polymerase function. Figure reproduced from (Ayaz et al., 2014). In the absence of Stu2, tubulin dimers associate non-productively with the microtubule end and often dissociate far more often than they incorporate into the polymer. This leads to slow microtubule growth. In the presence of Stu2, it is able to use its tethered TOG domains to stabilize, sequester and concentrate tubulin at the end of the microtubule. This creates a higher affinity binding site for tubulin on the end, as dimers can engage with both longitudinal and lateral contacts helping them to overcome the conformational energy barrier to straightening. More productive tubulin associations at the microtubule end leads to an increase in growth rate. Straightening of the tubulins releases the TOG domains, allowing the polymerase to repeat the cycle by capturing and binding new tubulin dimers.

Lack of in vitro reconstitution data for Stu2 has left unanswered questions as to the mechanism of the full-length protein

A large body of work has gone into elucidating the overall function of the XMAP215/Stu2 (suppressor of tubulin 2) family of proteins. Recent focus has centered on understanding the function of the tubulin-binding TOG domains, as these are the critical 'workhorse' components of the protein. While much is now known about the structure and function of the TOG domains, little remains to be understood about the remainder of these polymerase enzymes, particularly in regards to the yeast member, Stu2. Although the TOG's are critical to polymerase function, TOG domains by themselves cannot function as polymerases because they require the remaining domains on the protein in order to target them to the proper portion of the microtubule. Outside of the N-terminal TOG domains, Stu2 contains a flexible 72 amino acid linker that physically tethers the TOGs, and a 100 amino acid SK-rich basic domain region filled with positively charged amino acids like arginine (R) and lysine (K). The basic domain is followed by a ~100 amino acid coiled-coil domain, which is then followed by a ~120 amino acid flexible C-terminal tail. It was shown previously that the SK-rich basic domain is the microtubule binding domain, interacting through electrostatic interactions to the negatively charged C-terminal 'E-hook' tails of tubulin (Wang & Huffaker, 1997). The unstructured C-terminal tail has been shown to interact with a host of MAPs, such as Bim1 and Bik (Wolyniak et al., 2006). To form a detailed molecular mechanism to explain the polymerase function of Stu2, the full-length protein, not just the TOG domains, need to be studied to understand how all the components of Stu2 work together to increase the growth rates of microtubules. What happens if the linker length between TOG domains is altered? Can the polymerase function equivalent to that of wild-type Stu2 with only one type of TOG domain (ie only TOG1 or only

TOG2)? What if the order of the TOG domains are switched (TOG1-TOG2 vs. TOG2-TOG1)? What happens if the charge in the basic domain is altered? If XMAP215 and Zyg9 are monomeric polymerases, can Stu2 also function in a monomeric state if the coiled coil domain is removed? Taking these questions one step further, can the tubulin conformational cycle influence Stu2 activity, given that TOG domains strictly recognize and bind curved tubulin dimers? In Chapter 3 I will explore many of the above questions and provide new insights and details into the underlying molecular mechanism of the yeast microtubule polymerase, Stu2.

CHAPTER TWO

Understanding the Role of the Conformational Cycle with the use of an αβ-Tubulin Mutant

Reliance upon the GTPase activity of the tubulin subunits for functional dynamic instability has been a well-established feature of microtubule dynamics for many decades; what is less clear is the role of the conformational cycle. Although known that tubulin undergoes a conformational change between the polymer and solution-state, new high resolution structures have revealed multiple conformational states within the microtubule lattice over the course of polymerization. Given that GTP hydrolysis is a major driving force for dynamic instability, what is the purpose of the conformational cycle? Does the conformational cycle regulate dynamics or is it merely a consequence of nucleotide hydrolysis? The ability to address these questions by studying different conformational states is challenging, given how rapid the dynamics of microtubule growth and shrinkage are, and the fact that conformational states have only been isolated using stabilizing nucleotides (Zhang et al., 2015). The use of yeast tubulin rather than animal tubulin allows for the isolation and characterization of specific tubulin mutants—even mutants that may perturb the conformational cycle. Using a previously identified mutation in β-tubulin, T238A (hereafter β: T238A), I was able to purify and characterize the effects of a tubulin conformational mutant *in vitro*. In the first section of this chapter, I will discuss my initial characterization of β: T238A on yeast microtubule dynamics, which demonstrates how coupling the nucleotide and conformational cycles allows for fast dynamics and proper allosteric control in the lattice. In the second section of this chapter, I will discuss ongoing work to study the effects of β: T238A in human tubulin. I am interested in determining whether or not the stabilizing properties β: T238A can translate into higher eukaryotic homologues. To do this,

I will not only evaluate the biochemical properties of the mutation, but will attempt to solve high-resolution cryo-EM structures of wild-type and β: T238A human microtubules, in GMPCPP and GDP states. These structures will allow me to determine whether the mutation results in changes to the conformational state of the microtubule lattice.

I. A mutation uncouples the tubulin conformational and GTPase cycles, revealing allosteric control of microtubule dynamics

This section was re-produced from:

Geyer, E. A., Burns, A., Lalonde, B. A., Ye, X., Piedra, F. A., Huffaker, T. C. & Rice, L. M. (2015). A mutation uncouples the tubulin conformational and GTPase cycles, revealing allosteric control of microtubule dynamics. *Elife, 4*, e10113. Doi:10.7554/eLife.10112

Abstract

Microtubule dynamic instability depends on the GTPase activity of the polymerizing αβ-tubulin subunits, which cycle through at least three distinct conformations as they move into and out of microtubules. How this conformational cycle contributes to microtubule growing, shrinking, and switching remains unknown. Here, we report that a buried mutation in αβ-tubulin yields microtubules with dramatically reduced shrinking rate and catastrophe frequency. The mutation causes these effects by suppressing a conformational change that normally occurs in response to GTP hydrolysis in the lattice, without detectably changing the conformation of unpolymerized αβ-tubulin. Thus, the mutation weakens the coupling between the conformational and GTPase

cycles of αβ-tubulin. By showing that the mutation predominantly affects post-GTPase conformational and dynamic properties of microtubules, our data reveal that the strength of the allosteric response to GDP in the lattice dictates the frequency of catastrophe and the severity of rapid shrinking.

Experimental Procedures

Protein Expression and Purification

Protein expression and purification Plasmids to express TOG1, TOG2 and wild-type yeast αβ-tubulin were previously described (Johnson et al., 2011; Ayaz et al., 2012; 2014). A Bim1-GFP construct, in pHAT vector containing C-terminal EGFP-tag followed by a Strep-tag II, was a gift from Dr. Gary Brouhard. A plasmid to express the T238A mutation of Tub2p (yeast β-tubulin) was made by QuikChange (Stratagene) mutagenesis, using an expression plasmid for wild-type Tub2 as template and with primers designed according to the manufacturer's instructions. A C-terminal FlAsH (Griffin, Adams, Jones, & Tsien, 2000) sequence was added to a Tub1 construct using polymerase chain reaction with primers designed to add the sequence WDCCPGCCK (Griffin et al., 2000). The integrity of all expression constructs was confirmed by DNA sequencing. Wild-type or mutant yeast αβ-tubulin was purified from inducibly overexpressing strains of *S. cerevisiae* using Ni-affinity and ion exchange chromatography (Johnson et al., 2011; Ayaz et al., 2012; 2014) with the exception that T238A and wild-type FlAsH mutants were eluted from the Ni-affinity column with 200 mM NaCl. Prior to ion exchange chromatography, T238A Ni elution fractions were treated with Universal Nuclease (Pierce) at RT for 1 hr. Tubulin samples were stored in storage buffer (10 mM PIPES pH 6.9, 1 mM $MgCl_2$, 1 mM EGTA)

containing 20 or 50 µM GTP depending on the application. The TOG1(1-317) and TOG2(318-560) were expressed in E. coli with C-terminal His6 tags and purified using Ni-affinity, gel filtration (TOG1) and ion exchange chromatography (TOG2) (Ayaz et al., 2012; 2014). TOG domains were stored in RB100 (25 mM Tris pH 7.5, 100 mM NaCl, 1 mM $MgCl_2$, 1 mM EGTA). Expression of Bim1-GFP was induced in the BL21(DE3) strain of E. coli with 0.5 mM IPTG for 15 hrs at 16C. Single pellets were resuspended in 50 mM Na_2HPO_4, 300 mM NaCl, 40 mM imidazole and sonicated for 30 min in the presence of PMSF. Lysates were clarified by centrifugation. Cleared lysate was loaded onto a His60 Superflow Column (Clontech) and the final sample was eluted in 200 mM imidazole. Elution fractions were loaded onto a 3 mL Strep-Tactin Superflow column (IBA, Germany) and eluted in RB100 with 5 mM desthiobiotin.

Yeast strains for expression:

JEL1 MATa leu2 trp1 ura352 prb11122 pep43 Dhis3::PGAL10-GAL4

For analysis of growth phenotypes:

CUY 2172 MATa TUB2::URA3 ade2-101 his3-D200 leu2-1 lys2-801 ura3-52

CUY 2179 MATa tub2-T238A::URA3 ade2-101 his3-D200 leu2-1 lys2-801 ura3-52

CUY 2198 MATa tub2-T238S::URA3 ade2-101 his3-D200 leu2-1 lys2-801 ura3-52

CUY 2200 MATa tub2-T238V::URA3 ade2-101 his3-D200 leu2-1 lys2-801 ura3-52

For microtubule imaging:

CUY 2265 MATa TUB2::URA3 GFP-TUB1::LEU2::TUB1 ade2-101 his3-D200 leu2-1 lys2-801 ura3-52

CUY 2238 MATa tub2-T238A::URA3 GFP-TUB1::LEU2::TUB1 ade2-101 his3-D200 leu2-1 lys2-801 ura3-52 CUY 2208 MATa tub2-T238S::URA3 GFP-TUB1::LEU2::TUB1 ade2-101 his3-D200 leu2-1 lys2-801 ura3-52 CUY 2209 MATa tub2-T238V::URA3 GFP-TUB1::LEU2::TUB1 ade2-101 his3-D200 leu2-1 lys2-801 ura3-52

In vivo experiments

tub2 alleles were integrated into yeast as described previously (Reijo, Cooper, Beagle, & Huffaker, 1994) *in vivo* imaging of microtubule dynamics was performed as described previously (Huang & Huffaker, 2006). Note that introduction of GFP-TUB1 into strains containing the tub2-T238A mutation lessens their dependence on benomyl for growth (Figure 2.6) and allowed us to image these cells in the absence of benomyl.

Time-lapse measurements of microtubule dynamics

Flow chambers were prepared as described previously (Gell et al., 2010), with the exception that sea urchin axonemes (Waterman-Storer, 2001) were used to template yeast MT growth. Chambers were rinsed with BRB80 (80 mM PIPES pH 6.9, 1 mM $MgCl_2$, 1 mM EGTA), followed by 10 min incubation with sea urchin axonemes. Chambers were then blocked with 1% F-127 Pluronic in BRB80 for 5 min, and washed with 1X PEM (100 mM PIPES pH 6.9, 1 mM EGTA, 1 mM $MgSO_4$) containing 1 mM GTP. Reaction chambers were sealed with VALAP after addition of αβ-tubulin. Wild type or mutant yeast αβ-tubulin (in storage buffer containing 50 µM GTP) was taken from -80˚C, rapidly thawed, and passed through a 0.1 mm centrifugal filter at 4˚C to remove aggregates. The concentration of αβ-tubulin was measured by UV

absorbance using an extinction coefficient of 115000 M-1cm-1. Protein was kept on wet ice for no more than 30 min before measuring MT dynamics. MT dynamics were imaged by differential interference contrast microscopy (DIC) using an Olympus IX81 microscope with a Plan Apo N 60x/1.42 NA objective lens and DIC prisms. Illumination at 550 nm was obtained by inserting a bandpass filter of 550/100 nm (Olympus) in the light path. Temperature was maintained at 30˚C using a WeatherStation temperature controller with enclosure fit to the microscope's body. Micro-Manager 1.4.16 (Edelstein et al., 2010) was used to control the microscope and a Hamamatsu ORCA-Flash2.8 CMOS camera used to record the reactions. MT dynamics were recorded by taking an image every 500 ms for 1 to 2 hrs. At the end of each movie, a set of 100 out-of-focus background images was taken for background subtraction (see below). To improve signal to noise, batches of 10 raw images were averaged using ImageJ (Schneider et al., 2012) and intensity normalized before background subtraction. MT length was measured manually using a PointPicker plugin for ImageJ. Rates of MT elongation and catastrophe frequencies were determined as described previously (Walker et al., 1988).

Electron microscopy

To prepare microtubules for electron microscopy, samples of wild-type (3-–4 μM) or β:T238A αβ-tubulin (2 μM) were prepared in 100 mM PIPES pH 6.9, 10% glycerol, 2 mM $MgSO_4$, 0.5 mM EGTA, 1 mM GTP and incubated at 30 ˚C for 1 hr. 5 mL of the assembly reactions were spotted onto freshly glow-discharged 400 mesh grids with a carbon coated formvar support (Ted Pella), incubated for 30 s, rinsed with water, and stained with 2% aqueous uranyl acetate. Negatively stained grids were imaged at 23,000 x magnification using a Tecnai G2 Spirit electron microscope equipped with a 2Kx2K CCD camera (Gatan).

Assays for microtubule nucleation

Microtubule sedimentation assays were performed using a range of wild-type or mutant yeast αβ-tubulin concentrations (Figure 2.2B, 0.25 – 4 μM) in assembly buffer (100 mM PIPES pH 6.9, 10% glycerol, 2 mM $MgSO_4$, 0.5 mM EGTA) containing the indicated nucleotide. Samples were polymerized for 90 min at 30˚C. For SDS-PAGE analysis, microtubules were pelleted by centrifugation at 60,000 rpm (~150000 x g) at 30˚C for 30 min in a pre-warmed TLA-100 rotor (Beckman-Coulter), supernatant was carefully removed, and the pellet was re-suspended in an equal volume of assembly buffer such that the pellet and supernatant fractions were of equal volume. To image the products of the nucleation reactions, the reactions were cross-linked by diluting 10-fold into assembly buffer containing 1% glutaraldehyde. Cross-linking was quenched after 3 min by 5-fold dilution into assembly buffer containing 20 mM Tris pH 6.8. 150 mL of the quenched, cross-linked reactions were applied to the top of a glycerol cushion (20% glycerol in BRB80) and spun through the cushion onto poly-L-lysine coated coverslips. Coverslips were washed with BRB80, fixed with methanol and stained using FITC-DM1a (Sigma-Aldrich) for imaging by epifluorescence, as described previously (Ayaz et al., 2012).

Determining nucleotide content

Wild type (2 or 1 μM respectively for GTP or GTPγS) or β:T238A tubulin (1 μM for either nucleotide) was mixed with 100 mM GTP or GTPγS (containing 33 nM [α32P or γ32P]-GTP) in assembly buffer (see above) on ice. Microtubules were assembled and harvested by centrifugation at 80,000 rpm (~268000 x g) at 30˚C for 10 min in a pre-warmed TLA-120 rotor (Beckman-Coulter). Supernatant was carefully removed, and the pellets were gently washed 4

times with pre-warmed assembly and then resuspended with 6 M guanidine to denature the protein and release bound nucleotide. After 10-fold dilution into water, samples were loaded onto a Cellulose PEI TLC plate (Selecto Scientific) and TLC was performed, first with water followed by buffer containing 0.75 M Tris, 0.4 M LiCl, and 0.45 M HCl. The TLC plate was exposed to X-ray film after air drying. Radiolabelled mixtures of GTP/GDP and GTP/Pi were used as markers.

Analytical ultracentrifugation

Samples for analytical ultracentrifugation (TOG1, TOG2, yeast αβ-tubulin, and mutant T238A polymerization-competent yeast αβ-tubulin) were dialyzed into final buffer conditions of RB100 (25 mM Tris pH 7.5, 1 mM $MgCl_2$, 1 mM EGTA, 100 mM NaCl) containing 20 mM GTP. The samples shown in Figure 2.3 contain 0.15 µM T238A yeast αβ-tubulin and 0.015 µM, 0.03 µM, 0.15 µM, 0.3 µM, 0.6 µM, 1.2 µM, 5 µM TOG1 or 0.015 µM, 0.025 µM, 0.05 µM, 0.1 µM, 0.2 µM, 0.4 µM, 0.8 µM, 1.6 µM, and 5 µM TOG2. Samples were mixed and incubated at 4˚C for at least one hr prior to the experiment. All analytical ultracentrifugation experiments were carried out in an Optima XL-I centrifuge using an An50-Ti rotor (Beckman-Coulter). Approximately 390 mL of each sample were placed in charcoal filled, dual-sector Epon centerpieces. Sedimentation (rotor speed: 50,000 rpm) was monitored using absorbance at 229 nm and centrifugation was conducted at 20˚C after the centrifugation rotor and cells had equilibrated at that temperature for at least 2.5 hrs. Protein partial-specific volumes, buffer viscosities, and buffer densities were calculated using SEDNTERP (Laue et al., 1992). Data were analyzed using SEDFIT and SEDPHAT (available at http://www.analyticalultracentrifugation.com) (Schuck, 2000; Schuck, Perugini, Gonzales, Howlett, & Schubert, 2002).

Microtubule depolymerization fluorescence assays

Wild-type and mutant yeast αβ-tubulin were labeled with 6-–10 mM ReAsH in DMSO (Life Technologies) and 1 mM TCEP, in tubulin storage buffer (see above) for 90 min at RT. To remove excess unbound dye, samples were exchanged into assembly buffer (100 mM PIPES pH 6.9, 10% glycerol, 2 mM $MgSO_4$, 0.5 mM EGTA) with 2 mL, 7K MWCO Zeba spin desalting columns (Thermo Scientific). Labeled wild-type and mutant yeast αβ-tubulin were polymerized in the presence of 3–5 mM epothilone-B in assembly buffer (see above) with 1 mM GTP or in the presence of 500 µM GTPγS in assembly buffer (see above). The mixture was incubated for 30 min at 30˚C. Flow chambers were prepared as described above. His-Tag Antibody (1:200, Gentech) was incubated in the chamber for 10 min, followed by incubation with 1% Pluronic F-127 in BRB80 for 5 min, followed by a wash with BRB80. Pre-formed, epothilone- or GTPγS-stabilized wild-type or T238A yeast MTs were then introduced into the chamber and allowed to incubate for 10 min, followed by a wash with BRB80 to remove unbound MTs. Solutions containing a range of TOG1 (0.1-–10 µM) or TOG1(R200A) (250, 750 nM) concentrations (Figure 2.5B) in imaging buffer (BRB80 + 200 nM epothilone + 0.1 mg/mL BSA + antifade reagents (glucose, glucose oxidase, catalase), without the addition of β-mercaptoethanol [Gell et al., 2010]) were introduced into the chamber immediately prior to data collection. To ensure that the TOG-induced depolymerization was not an artifact of fluorescence imaging, unlabeled wild-type microtubule were assembled as described above but without ReAsH labeling and then imaged with two concentrations of TOG1 using DIC microscopy (black points in Figure 2.5B). MT depolymerization reactions with fluorescent microtubules were imaged by epifluoresence microscopy using an Olympus IX81 microscope with a Plan Apo N 60x/1.42 NA objective lens

and Hamamatsu ORCA-Flash2.8 CMOS camera, a mercury short arc lamp, and a Texas Red filter cube (Olympus). Reactions were temperature controlled and the microscope was controlled as described above. Images of MT shrinking were recorded every 60 s for about 10 min. MT depolymerization reactions with non-fluorescent wild-type microtubules were imaged using differential interference microscopy as described above. MT length was measured manually using ImageJ (Schneider et al., 2012). Average lengths of MT's were taken over the time course of the movie and were used to determine rate of depolymerization over an hour time span.

Dynamic assays with Bim1-GFP

Preparation of flow chambers using sea urchin axonemes was followed as described above. Samples of wild-type, β:T238A, or C354A αβ-tubulin with 1 mM GTP or GTPγS were prepared and incubated in flow-chambers for 30–180 min and observed under DIC to evaluate presence of microtubule growth. After a given time, solutions containing desired tubulin sample and nucleotide of interest, along with 5 or 50 nM Bim1-GFP with imaging buffer described above, were flowed into the chamber. Interactions of Bim1-GFP with MTs were imaged by total internal reflection fluorescence microscopy using an Olympus IX81 microscope with a TIRF ApoN 60x/1.49 objective lens, a 491 nm 50 mW solid-state laser and Hamamatsu ORCA-Flash2.8 CMOS camera (Olympus). Reactions were temperature controlled at 30˚C and the microscope was controlled as described above. Axonemes were tracked under DIC and TIRF conditions. Images of MTs were taken over several frames from 15–30 min. Bim1-GFP fluorescence intensity along microtubules and extending beyond their growing ends was obtained using the PlotProfile function in ImageJ (Schneider et al., 2012). These linescans were

manually aligned to superimpose the sharp change in intensity at the very microtubule end, and aligned intensity values were averaged.

Analysis of sequence conservation

To collect a large number of a- and β-tubulin sequences, we performed psiblast (Altschul et al., 1997) (non-redundant (nr) database, 3 iterations) on the amino acid sequences of Tub1p and Tub2p from S. cerevisiae. The top 1000 sequences from both searches were aligned using Clustal Omega (Sievers et al., 2011) and manually pruned in Jalview (Waterhouse, Procter, Martin, Clamp, & Barton, 2009) to eliminate sequences with large insertions or deletions

Results

The buried T238A mutation in β-tubulin hyperstablizes microtubules *in vivo* and *in vitro*

The β:T238A mutation was previously identified by virtue of drug- and temperature-sensitive phenotypes that were consistent with hyperstable microtubules (Thomas et al., 1985). However, prior studies of this mutant have not directly examined its polymerization dynamics *in vivo* or *in vitro*(Dorn et al., 2005; Machin, Lee, & Barnes, 1995) . To obtain insight into how the mutation affects polymerization dynamics in cells, we used time lapse imaging in GFP-Tub1p expressing strains to measure microtubule dynamics of wild-type and β:T238A-containing yeast. These measurements revealed that β:T238A-tubulin forms static microtubules (neither growing nor shrinking) that are on average over 50% longer than the dynamic microtubules that form in a strain with wild-type β-tubulin (Figure 2.1B). Because the mutated site is solvent inaccessible,

this striking change in microtubule dynamics cannot be the result of a direct perturbation of a polymerization interface or of an interaction with one or more regulatory proteins. To determine how the buried β:T238A mutation affected microtubule dynamics *in vitro*, we purified β:T238A αβ-tubulin from an overexpressing strain of yeast (Johnson et al., 2011) and used time-lapse differential interference contrast microscopy to measure its polymerization dynamics. We were unable to measure mutant and wild-type microtubule dynamics at equivalent concentrations, because β:T238A αβ-tubulin showed abundant spontaneous nucleation at the higher concentrations where we measured wild-type, and wild-type αβ-tubulin does not elongate measurably at the low concentrations where we were able to measure β:T238A dynamics without excessive nucleation. Mutant and wild-type microtubules nevertheless show similar concentration-dependent elongation rates: fitting lines to mutant and wild-type data reveals that the x-intercepts of the two datasets (0.12 and 0.033 μM for wild-type and β:T238A, respectively) differ by a factor of ~3.5 and that the difference in slope (29.6 and 25.5 μm/hr/μM for wild-type and β:T238A, respectively) is not statistically significant (Figure 2.1D). Because the x-intercept and slope respectively relate to the apparent affinity and association rate constant for elongation, our data indicate that the mutation has little effect on the apparent biochemistry of microtubule elongation. Consistent with this biochemical similarity, negative stain electron microscopy revealed that mutant and wild-type microtubules show similar structure (Figure 2.1C). In striking contrast to the shared elongation behavior, after catastrophe β:T238A microtubules shrink roughly hundredfold more slowly than wild-type (1.1 μm/min for β: T238A compared to 96 mm/min for wild-type, Figure 2.1E, bottom). Thus, the mutation significantly strengthens the lattice contacts that dictate the rate of microtubule shrinking. Finally, β:T238A microtubules also undergo catastrophe much less frequently than wild-type. The lower catastrophe frequency we

observed is especially notable when considering that in these assays the T238A microtubules were growing much slower than wild-type because of the ~threefold lower concentration of αβ-tubulin used for the mutant (Figure 2.1E, top).

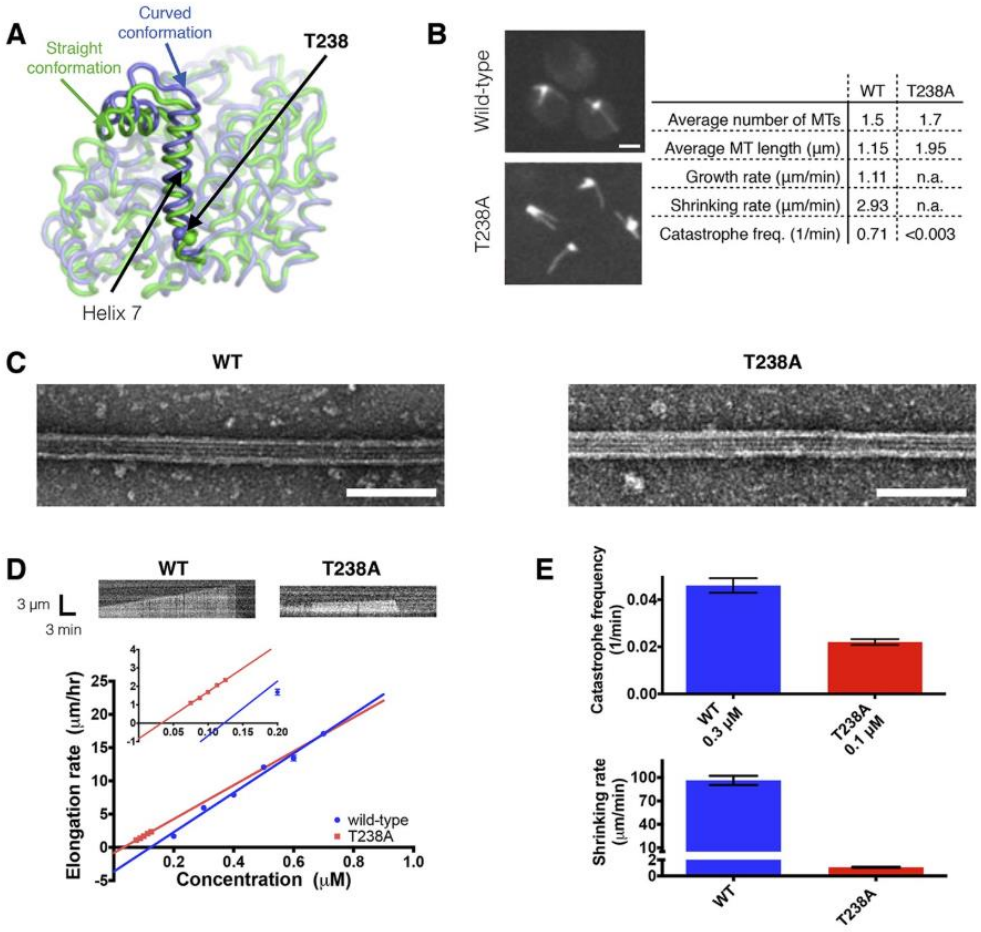

Figure 2.1. αβ-tubulin containing a buried mutation in β-tubulin gives hyperstable microtubules *in vivo* and *in vitro*. (A) Superposition of polymerized ('straight', green, PDB 1JFF) and unpolymerized ('curved', blue, PDB 4FFB) conformations of β-tubulin. T238 is solvent inaccessible and resides on a helix (H7) that undergoes a piston-like movement between the two conformations. The view of β-tubulin shown here is as if from the center of the microtubule looking out, with the plus end at the top. (B) Time-lapse imaging of live yeast shows that cells expressing T238A αβ-tubulin make longer, less dynamic microtubules than their wild-type (WT) counterparts. N = 13, 18 for WT and T238A microtubules respectively, with t = 35, 72 min total time observed. Bar = 2 µm (C) Negative stain electron micrographs (magnification: 23,000x) of wild-type (left) and β: T238A (right) microtubules. Mutant microtubules have normal structure. Bar = 100 nm. (D) *In vitro*, T238A and wild-type microtubules show similar concentration-dependent growth rates (slopes: 29.6 +/- 1.8 µm/hr/µM for wild-type, 25.5 +/- 0.8 µm/hr/µM for β:T238A, the differences between the slopes are not statistically significant; x-intercepts: 0.12 µM for wild-type, 0.033 µM for β:T238A, this difference is statistically significant; significance of differences in regression parameters was evaluated using GraphPad Prism). Representative kymographs are shown above the plots. (N = 12 for all points except 0.2 µM where N = 20; bars show s.e.m.) (E) T238A microtubules catastrophe less frequently than wild-type (top; N = 99, 115 for wild-type and T238A respectively, bars show s.d.) and show a ~hundredfold slower rate of post-catastrophe shrinking (bottom; N = 16 for wild-type and T238A, bars show s.e.m.).

Mutant-induced changes in polymerization dynamics do not result from defective GTPase activity

The β:T238A mutation stimulated spontaneous nucleation and reduced the frequency of catastrophe and the rate of shrinking, all without substantially affecting elongation. It seemed possible that a defective GTPase cycle might explain these observations. We reasoned that if the increased spontaneous nucleation of the β:T238A mutant resulted from slower/defective GTPase activity, then both mutant and wild-type should nucleate with similar efficiency when GTP hydrolysis cannot occur. We initially attempted to use GMPCPP, the hydrolysis-resistant nucleotide of choice for vertebrate microtubules (Hyman et al., 1992), but GMPCPP did not support elongation of yeast microtubules in our dynamics assays. Yeast microtubules polymerized readily in the presence of GTPγS, however, indicating that GTPγS better mimics GTP for yeast microtubules. We observed that even in the presence of GTPγS, wild-type microtubules show substantially less nucleation than T238A microtubules (Figure 2.2A,B). Thus, the abundant nucleation from the mutant cannot be ascribed to a defect in GTPase activity. Instead, the mutation must be affecting some other property that limits spontaneous nucleation in wild-type αβ-tubulin.

To support the idea that the mutation-induced changes in dynamics result from something other than a defect in GTPase activity, we assayed the nucleotide content of wild-type and β:T238A microtubules. We allowed wild-type and β:T238A αβ-tubulin to spontaneously polymerize at 1 or 2 μM concentration (within the range of concentrations tested in Figure 2.2A) in the presence of 32P-GTP. We harvested the microtubules by centrifugation, denatured them to release bound nucleotides, and analyzed the nucleotide content at the exchangeable site using thin layer chromatography (TLC) (Figure 2.2C,D). We probed for a GTPase defect using a-

labeled nucleotide to measure the amounts of GTP and GDP in microtubules, and for a phosphate release defect using γ-labeled nucleotide to measure the amounts of GTP and Pi in microtubules. To avoid possible complications that might arise from the very different catastrophe frequencies and shrinking rates, we initially performed these assays under 'catastrophe free' and slow shrinking conditions by using (unlabeled) GTPγS to support assembly. These experiments revealed that wild-type and mutant microtubules contain similarly low amounts of GTP (2–4% of total exchangeable nucleotide) and Pi (fewer than 3% of exchangeable sites) (Figure 2.2C,D). When we performed these assays using (unlabeled) GTP to support microtubule assembly, β:T238A microtubules contained similarly low amounts of GTP and Pi as we observed with GTPγS but wild-type microtubules appeared to contain a substantially greater amount (~50%) of GTP (Figure 2.2C,D). Yeast microtubules have previously been reported to contain more GTP than vertebrate microtubules (Dougherty, Himes, Wilson, & Farrell, 1998). In control experiments (not shown) we confirmed that vertebrate microtubules contain very little GTP and that individual heterodimers were not pelleting. Because we observed very fast shrinking (Figure 2.1), little 32P-GTP in microtubules grown with GTPγS (Figure 2.2C), and normal plus-end recognition by an EB1 family protein (see below), it seems unlikely that wild-type yeast microtubules contain substantial amounts of GTP. The GTP containing material in our assay might instead reflect oligomers that form more readily for yeast αβ-tubulin. Whatever the mechanism, these experiments demonstrate that β:T238A αβ-tubulin remains competent to hydrolyze GTP, and that the altered nucleation and shrinking behavior cannot be ascribed to an accumulation of GTP or GDP.Pi that might result from a defect in assembly-dependent GTPase activity or phosphate release. Some other, nonenzymatic mechanism must therefore account for the observed changes in polymerization dynamics.

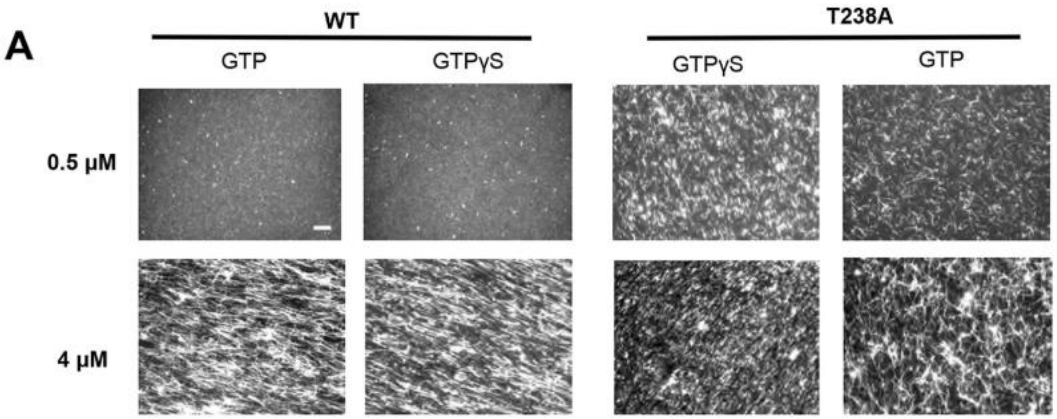

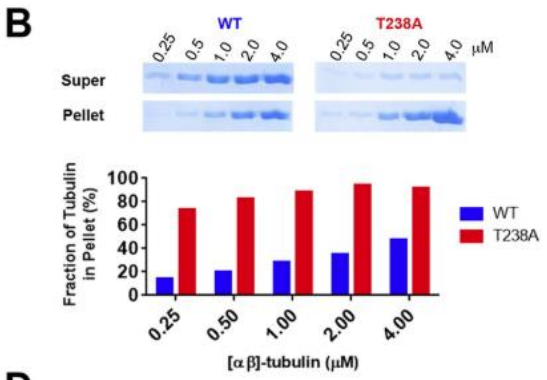

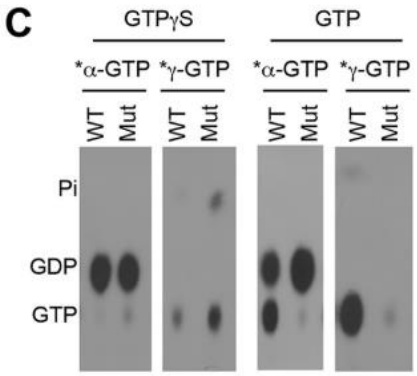

D

Unlabeled nucleotide supporting assembly	GTPγS		GTP	
Tubulin	WT	T238A	WT	T238A
Remaining GTP (%)	2.20 ± 0.75	4.02 ± 0.86	43.63 ± 1.63	2.02 ± 0.45
Remaining Pi (%)	2.31* ± 0.60	1.24 ± 0.91	2.58 ± 0.30	Undetectable

Figure 2.2. T238A αβ-tubulin undergoes spontaneous nucleation more readily than WT, even in the presence of a non-hydrolyzable GTP analog, GTPγS. (A) Fluorescent images of cross-linked microtubules from spontaneous nucleation reactions. Even at low concentrations and in the presence of GTPγS, T238A tubulin shows increased spontaneous nucleation compared to WT. GTPγS reactions are presented next to each other to facilitate a side-by-side comparison. Scale bar in top left is 5 μm. (B) Microtubule spin-down reactions show that under the same concentration range, in the presence of GTPγS, T238A tubulin produces a greater proportion of microtubules which sediment into the pellet. Gel images of supernatant and pellet fractions (top). (C) T238A microtubules do not accumulate GTP or GDP.Pi compared to wild-type. Images show TLC analysis of exchangeable nucleotide content of microtubules grown with GTP or GTPγS. Microtubules were spontaneously assembled using higher concentrations than for the dynamics assays: wild-type microtubules were prepared at 2 μM with GTP and 1 μM with GTPγS. β:T238A microtubules were prepared at 1 μM with either nucleotide. (D) Quantification of TLC data, n = 3 and errors shown represent s.d. *indicates one condition where we could not detect any Pi in one of the replicates; instead of using 0 we used the lower of the two other trials.

The buried T238A mutation in β-tubulin does not detectably 'straighten' unoligomerized αβ-tubulin

Unoligomerized GTP-bound αβ-tubulin adopts a curved conformation that is not compatible with the straight microtubule lattice (Nawrotek et al., 2011; Pecqueur et al., 2012; Ayaz et al., 2012;2014). It seemed possible that the β:T238A mutation might stabilize microtubules by shifting the conformational preference of unpolymerized αβ-tubulin to favor a straight(er) conformation that is more compatible with the microtubule lattice. We used quantitative TOG binding assays (Ayaz et al., 2014) to determine if the β:T238A mutation changed the 'curvature' of unpolymerized αβ-tubulin. The rationale for this approach is based on the fact that TOG domains bind tightly to curved αβ-tubulin but very weakly to straight (Figure 2.3A) (Ayaz et al., 2012; 2014). Accordingly, β: T238A αβ-tubulin should bind less tightly to a TOG domain if the β:T238A mutation appreciably changes the conformation of αβ-tubulin, for example by straightening it. TOG1 and TOG2, two different TOG domains from the yeast microtubule regulatory factor Stu2p (Wang and Huffaker, 1997), show very similar affinity (within a factor of two) for unpolymerized T238A αβ-tubulin as they do for wild-type (Figure 2.3B). In energetic terms, this modest difference in affinity is roughly equivalent to one hydrogen bond. While we cannot state that the mutant and wild-type αβ-tubulin adopt identical conformations, their very similar TOG binding properties indicate that any differences in conformation must be small. Thus, we conclude that the β:T238A mutation does not significantly change the conformation of unpolymerized αβ-tubulin.

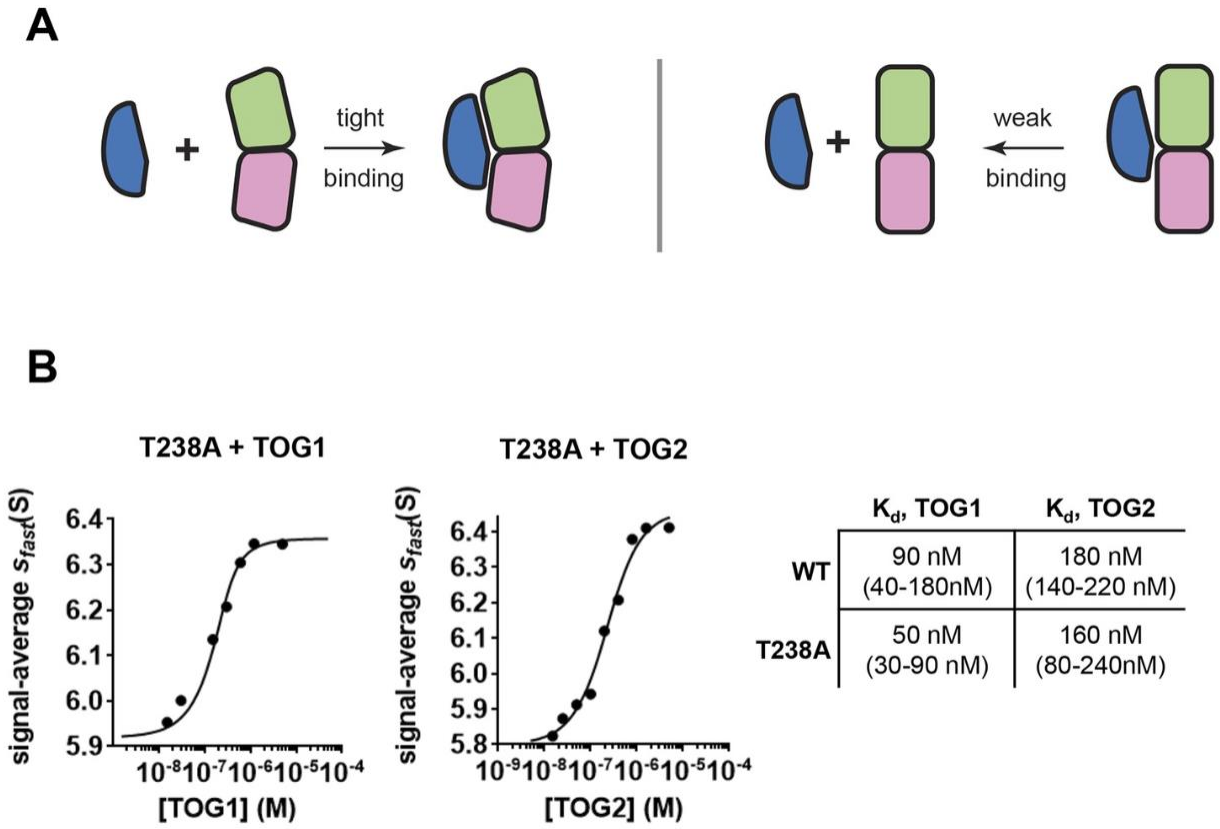

Figure 2.3. The buried β:T238A does not appreciably straighten unpolymerized αβ-tubulin. (A) Cartoon schematics illustrating that TOG domains (blue) bind tightly to curved αβ-tubulin (pink and green; left) but weakly to straight αβ-tubulin (right). (B) Isotherms for individual Stu2 TOG domains binding to T238A αβ-tubulin. Both TOG domains bind with comparable affinity to T238A and WT tubulin. 1 σ confidence intervals for fitted affinities are provided in parentheses

The β:T238A mutation suppresses GTPase-dependent conformational changes in the microtubule lattice

Recent cryo-EM studies of microtubule structure provided atomic models for distinct microtubule lattices containing GTP, GTPγS, or GDP, with GTP favoring an 'expanded' form and GTPγS and GDP favoring a 'compacted' form (Alushin et al., 2014; Zhang et al., 2015). Plus-end tracking proteins in the EB1 family have been shown to discriminate between these GTP-like and GDP-like lattices (Maurer et al., 2011; 2012; 2014; Zanic et al., 2009). We used Bim1p (Schwartz, Richards, & Botstein, 1997), the yeast EB1 protein, to investigate if the β:T238A mutation affected αβ-tubulin conformation in the lattice.

Control experiments revealed that a Bim1-GFP fusion protein tracked the growing end of yeast microtubules, and that Bim1-GFP coated the entire length of GTPγS-containing yeast microtubules with cap-like intensity (Figure 2.4). We therefore infer that like other EB1 proteins on vertebrate microtubules (Maurer, Bieling, Cope, Hoenger, & Surrey, 2011; Zanic, Widlund, Hyman, & Howard, 2013), Bim1 discriminates between GTP and GDP forms of the yeast microtubule lattice (presumably, expanded and compacted). In marked contrast to its behavior on wild-type microtubules, at 50 nM concentration Bim1-GFP coated the entire length of 'dynamic' β:T238A microtubules with cap-like intensity. At lower concentrations (5 nM), the Bim1-GFP coat on the body of β:T238A microtubules is slightly weaker than at the cap but still substantially more intense than on wild-type (Figure 2.4B). This stronger coating reflects tighter Bim1 binding to mutant microtubules, and it occurs in spite of the fact that the mutant microtubules contain very little GTP or GDP.Pi in the exchangeable site (Figure 2.2). Thus, the β:T238A mutation attenuates the conformational response to GTP hydrolysis in the microtubule lattice. The structural consequence of the mutation resembles the effect of taxol binding, which

also promotes an expanded conformation of αβ-tubulin in a GDP lattice (Alushin et al., 2014). Simply put, the mutation appears to have substantially uncoupled the conformational cycle from the nucleotide cycle in the lattice, allowing αβ-tubulin to retain GTP-lattice-like character even in a GDP lattice.

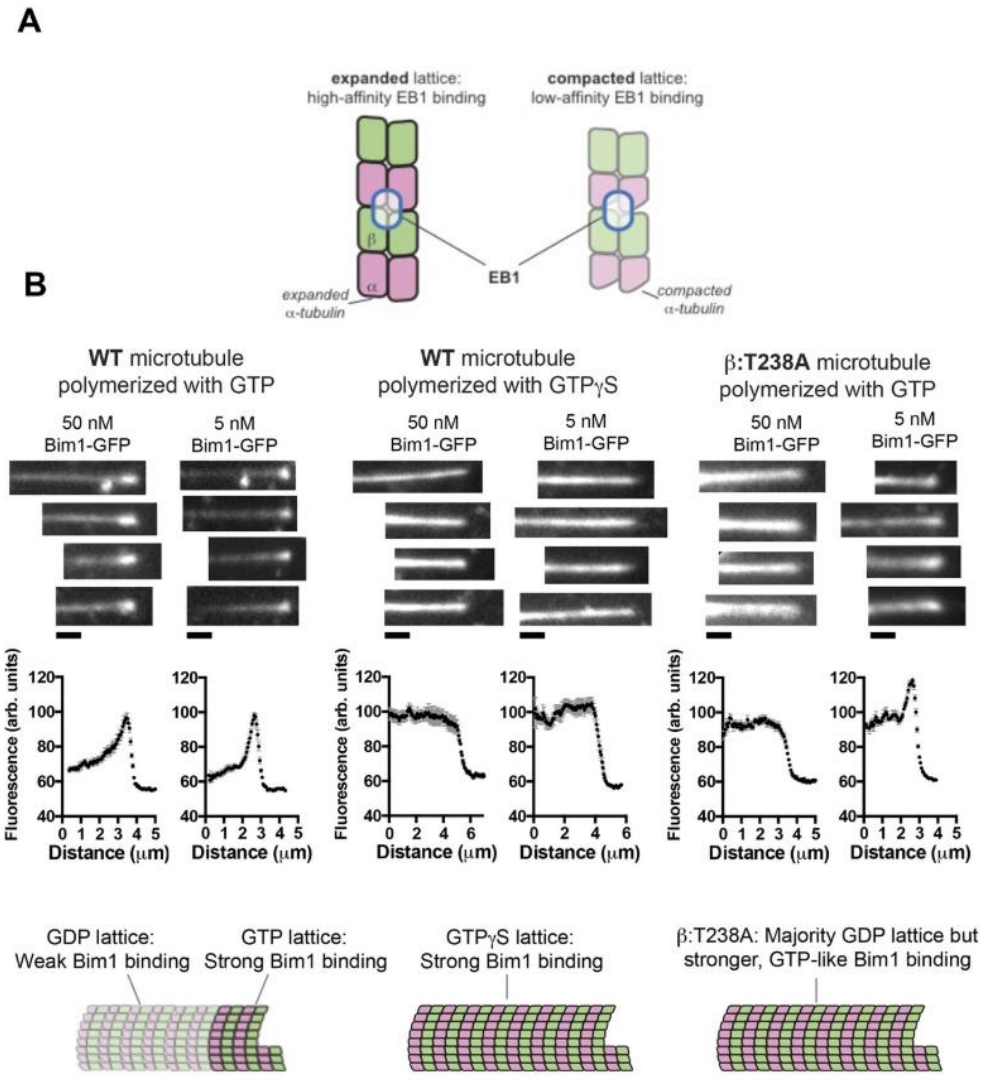

Figure 2.4. The buried β:T238A attenuates the conformational response to GDP in the lattice. (A) Cartoon schematics illustrating the basis of the assay: EB1 proteins (blue outlined ovals) bind tightly to the GTP-lattice conformation of αβ-tubulin (left) but weakly to the GDP-like conformation (right). (B) Images of the distribution of Bim1-GFP (an EB1 family protein) on wild-type (left and center) or mutant microtubules (right). 4 microtubules are shown for each condition, and Bim1-GFP was present at 50 nM and 5 nM concentration for all microtubules. Plots represent average Bim1-GFP intensity on n = 9 microtubules for each condition. Error bars represent s.e.m. Cartoons illustrate the likely lattice conformation inferred from the Bim1-GFP binding. β:T238A microtubules appear GTP-like even though they contain GDP. Scale bars: 1 μm.

The β:T238A mutation affects αβ-tubulin curvature on the microtubule end

The Bim1 experiments described above do not report on the conformation of αβ-tubulin at the very microtubule end because EB1 proteins do not bind there (Maurer et al., 2012; 2014). After fortuitously discovering that isolated TOG domains from the microtubule polymerase Stu2p stimulate the depolymerization of stabilized microtubules in a dose-dependent way, it seemed that TOG domains might provide an alternative way to probe the conformation of αβ-tubulin on the microtubule end. In light of the fact these TOG domains bind preferentially to the curved conformation of αβ-tubulin, we reasoned that the underlying cause of this induced depolymerization was TOG-mediated stabilization of the curved and faster dissociating conformation of αβ-tubulin on the microtubule end (Figure 2.5). According to this view, TOG-induced depolymerization thus provides an assay that probes the linkage (or lack thereof) between changes in αβ-tubulin conformation on the polymer end and microtubule shrinking rate. Using drug-stabilized microtubules as a substrate, the rate of TOG-induced depolymerization increases linearly over at least a 20-fold range of TOG concentration. This linear concentration dependence is consistent with a collisional mechanism in which the rate-limiting step is a TOG domain arriving at the microtubule end. It is not consistent with a mechanism in which the rate-limiting step is some kind of slow αβ-tubulin conformational change. Drug-stabilized β:T238A microtubules depolymerize substantially slower than wild-type at the same concentration of TOG domain (Figure 2.5). Only at higher TOG concentrations do β:T238A microtubules show appreciable dose dependent TOG-induced depolymerization (Figure 2.5). Similar results were obtained using MTs stabilized with GTPγS (Figure 2.5). TOG domains bind with comparable affinity to curved wild-type and mutant αβ-tubulin, so differences in TOG affinity cannot explain the markedly slower TOG-induced shrinking of β:T238A microtubules. Differences in the

amount of curved αβ-tubulin at wild-type and mutant microtubule ends could explain the observed differences in TOG-induced shrinking. In principle there might be other mechanisms that strengthen association without affecting the propensity to be curved on the microtubule end. However, while such 'curvature invariant' mechanisms in αβ-tubulin might explain the slow post-catastrophe shrinking of the mutant, the conformation-selective nature of TOG:tubulin interactions means that this alternative view is not easily reconciled with the observed differences in TOG-induced depolymerization. Thus, a mutant-induced change in the propensity to become/ remain straight on the microtubule end is the simplest way to explain both the slower post-catastrophe shrinking and weaker TOG-induced depolymerization for the mutant. That the conformation of end-bound αβ-tubulins is affected by the β:T238A mutation is also consistent with the Bim1 coating, which demonstrated that the mutation affected αβ-tubulin conformation elsewhere in the lattice.

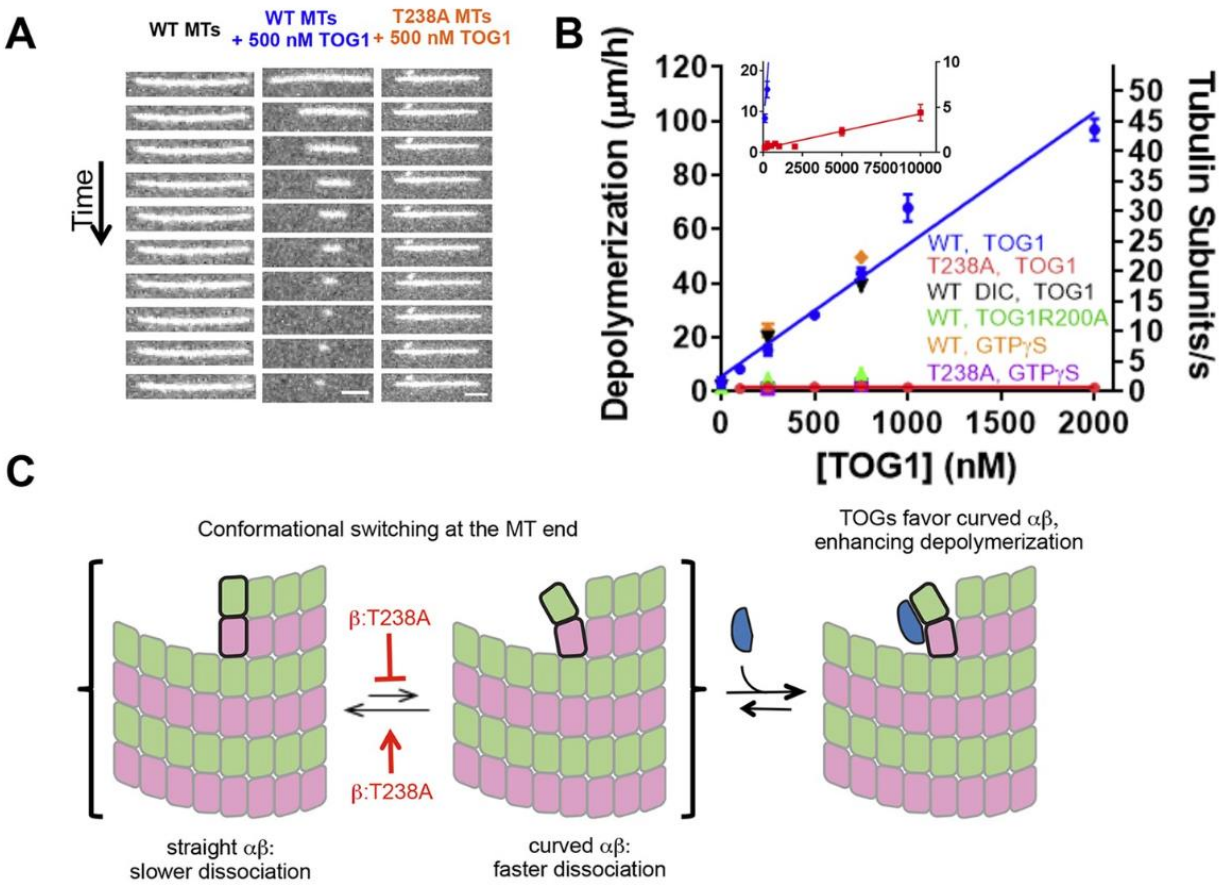

Figure 2.5. β:T238A microtubules are resistant to TOG-induced depolymerization. (A) A time series of images of stabilized fluorescent microtubules show that under the same concentration of TOG1, T238A microtubules depolymerize substantially slower than WT microtubules. Scale bars: 1 mm. (B) Quantification of the dose dependence of the rate of TOG-induced depolymerization. Inset: a plot showing that under higher TOG1 concentrations, T238A microtubules also undergo induced depolymerization. We observed similar rates of TOG induced depolymerization using DIC instead of fluorescence to monitor microtubule length (black triangles), as well as using GTPγS instead of epothilone as a stabilizing reagent (orange diamonds, purple squares). Additional control experiments demonstrate that the TOG-induced depolymerization is greatly reduced when a weakly binding TOG1 mutant (R200A) is used (green triangles). N = 30 for fluorescence measurements of wild-type TOG1-induced depolymerization of wild-type or β:T238A microtubules, N = 20 for the rest. Error bars represent s. e.m. (C) Cartoon model illustrating the mechanism of TOG-induced depolymerization, resulting from TOG stabilization of tubulin subunits sampling curved conformation at the end of the microtubule. T238A microtubules depolymerize slower due to a decrease in tubulin subunits sampling the curved conformation once incorporated into the polymer.

What is the structural origin of the β:T238A effects?

To gain insight into the local interactions responsible for the β:T238A effects on microtubule dynamics, we measured benomyl sensitivity/resistance and *in vivo* microtubule dynamics for serine and valine substitutions at the same position (Figure 2.6). Yeast expressing b:T238S αβ-tubulin are comparably benomyl resistant to β:T238A, but significantly less benomyl dependent (Figure 2.6A). By contrast, yeast expressing β:T238V αβ-tubulin are substantially less resistant to benomyl, and show no benomyl dependence (Figure 2.6A). Measurements of microtubule dynamics *in vivo* are consistent with the benomyl phenotypes: β:T238S microtubules are β:T238A-like (static) whereas β:T238V microtubules are more wild-type-like (dynamic but with somewhat slower shrinking) (Figure 2.6B). The trend with sidechain size and the strong effect obtained from the Thr to Ser mutation at position 238 suggest that some form of 'steric overpacking', not hydrogen bonding, contributes to destabilize the straight, expanded conformation of αβ-tubulin in microtubules containing GDP. Reducing the size of β:C354, a buried sidechain that packs against β:T238 (Figure 2.6C), has also been shown to stabilize microtubules (Gupta, Bode, Dougherty, Marquez, & Himes, 2001; Gupta et al., 2002).Indeed, β:C354A or β:C354S substitutions dramatically reduced the rate of microtubule shrinking and the frequency of catastrophe (Gupta et al., 2002). If these volume-reducing mutations also stabilize the expanded conformation of αβ-tubulin in a GDP lattice, it would provide complementary support for our overpacking-based rationale for the β:T238(A, S, V) effects. We purified β:C354A αβ-tubulin and used Bim1-GFP to probe its conformation in microtubules. β:C354A microtubules showed Bim1-GFP coating similar to what we observed for β:T238A, indicating the two mutations stabilize microtubules through a common conformational mechanism (Figure 2.6C). Positions 238 and 354 in β-tubulin show strong evolutionarily

conservation (yeast numbering; β:238 is 65% T and 34% C whereas β:354 is 99% C), consistent with an important functional role for these residues. Together, the β:T238A and b:C354A results suggest that changes in packing volume near helix H7 can dictate the dynamic properties of microtubules by tuning an allosteric response to GDP.

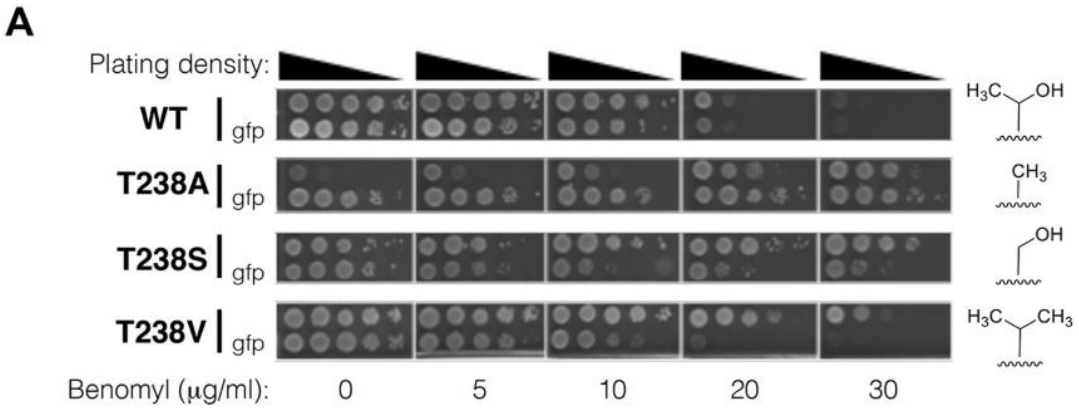

B

	WT	T238A	T238S	T238V
Average number of MTs	1.5	1.7	1.5	1.8
Average MT length (μm)	1.15	1.95	1.21	1.16
Growth rate (μm/min)	1.11	n.a.	n.a.	1.13
Shrinking rate (μm/min)	2.93	n.a.	n.a.	1.47
Catastrophe freq. (1/min)	0.71	<0.003	<0.008	0.3

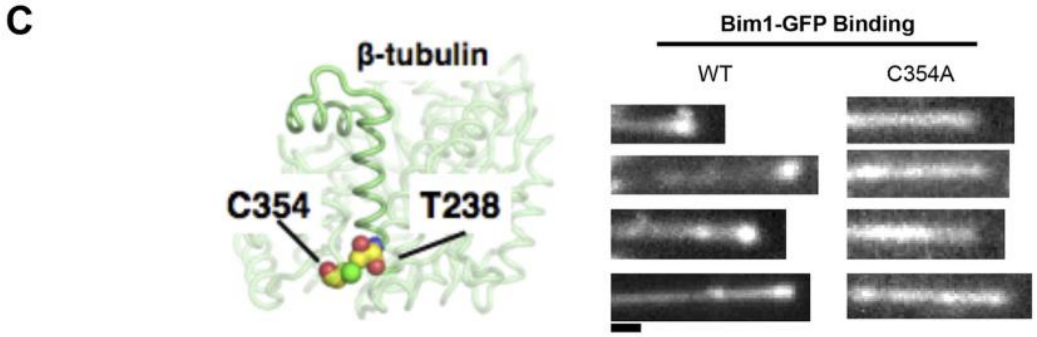

Figure 2.6. Insights into the mechanism underlying the β:T238A effects on the conformational cycle. (A) Yeast with different substitutions for T238 (for each mutant, strains with and without GFP-Tub1p are shown) show intermediate degrees of benomyl resistance/dependence. The volume of the packing defect may be related to the magnitude of the resulting phenotype: T238S has a phenotype closer to T238A whereas T238V has a phenotype closer to wild type. (B) *In vivo* microtubule dynamics of yeast containing T238S and T238V αβ-tubulin. N = 24, 14 for T238S and T238V microtubules respectively, with t = 120, 43 min total time observed. (C) The buried β: C354A mutation immediately proximal to T238 (left) has also been shown to give slowly shrinking microtubules, and also shows an expanded lattice (right). The view of the structure is as if from the center of the microtubule looking out, with the plus end at the top. Scale bar: 1 μm.

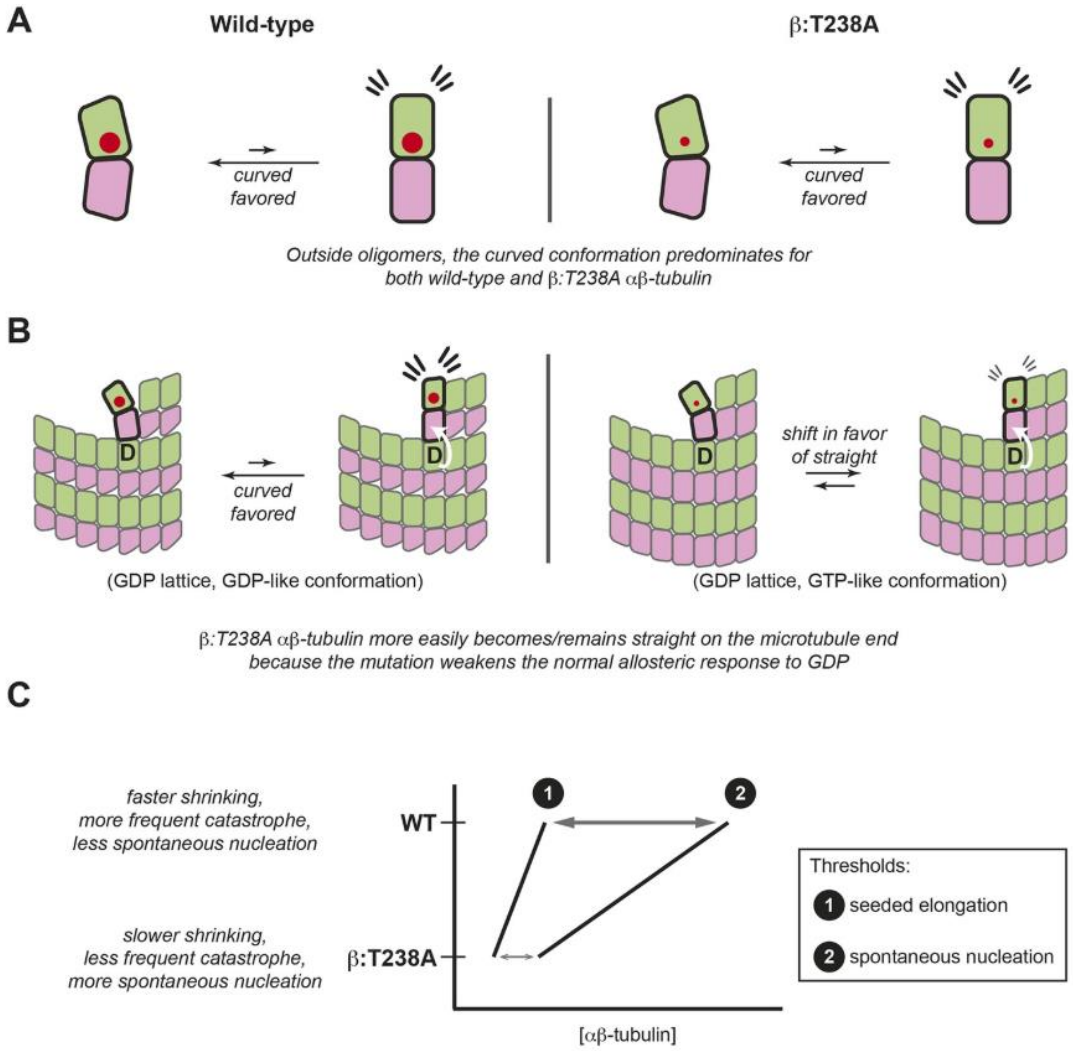

Figure 2.7. The αβ-tubulin conformational cycle and its impact on microtubule dynamics. (A) Unoligomerized wild-type and β:T238A αβ-tubulin both adopt the curved conformation. That the straight conformation is strained (flare marks) even with the mutation-induced reduction in packing volume (cartooned by larger and smaller red circles for wild-type and β:T238A, respectively) suggests that extrinsic factors like interactions with the lattice control straightening. (B) Compared to wild-type, β:T238A αβ-tubulin is better able to populate a straight conformation on the end of GDP containing microtubules. 'D' indicates GDP underneath the bolded terminal subunit, compaction is represented as in Figure 2.4, and the white arrow cartoons trans-acting nucleotide (see text). The increased ability of the mutant to be straight could result from an altered response to GDP on the longitudinal interface, from more favorable interactions with the expanded lattice, or from a combination of both. (C) The schematic phase diagram illustrates that the mutation-induced changes to the αβ-tubulin conformational cycle decrease the threshold concentrations for appreciable elongation against catastrophe (line 1) and for spontaneous nucleation (line 2), and also narrows the gap between them. The normal αβ-tubulin conformational cycle contributes to microtubule dynamics and makes them more amenable to regulation.

Discussion

We demonstrate that relatively conservative buried mutations in β-tubulin can diminish the conformational response to GDP in the lattice, and that this altered structural response yields dramatic effects on microtubule dynamics. By discovering that mutations can uncouple the conformational and nucleotide cycles of αβ-tubulin, our findings provide new insights into ways that the αβ-tubulin conformational cycle dictates microtubule polymerization dynamics (Figure 2.7).

Our experiments using the EB1 family protein Bim1 showed that in the lattice a major effect of the β:T238A mutation is to substantially suppress conformational changes that normally occur as a consequence of GTPase activity (Hyman et al., 1995; Alushin et al., 2014; Zhang et al., 2015). The different responses of yeast and vertebrate microtubules to GMPCPP, and the lack of high-resolution structures for wild-type or mutant yeast microtubules, make it difficult to know the specific conformations involved and how they relate to the nucleotide cycle. However, the stronger binding of Bim1 to GDP-containing β:T238A microtubules indicates that the mutant microtubule lattice retains more GTP-like character than does wild-type. This observation about αβ-tubulin in the body of the microtubule cannot by itself explain the slow shrinking, however, because the rate of shrinking is determined by the properties of incompletely surrounded terminal subunits, on which EB1 does not report. Indeed, understanding how different lattice structures relate to dynamic properties of microtubules remains a significant challenge. Our experiments with TOG domains indirectly probed the conformation of terminal subunits and showed that the β:T238A mutation reduces the propensity of terminal αβ-tubulins to be curved. Thus, the slow shrinking and lower frequency of catastrophe in the mutant most likely result from the attenuated allosteric response to GDP; this in turn results in a straighter and more

strongly associated GTP-like conformation on the microtubule end, despite having GDP at the longitudinal interface (Figure 2.7B).

It is remarkable that the majority of the mutation-induced effects are confined to post-GTPase conformational changes in the lattice. Not observing significant effects on elongation is somewhat surprising, because it had been anticipated that the conformational changes required to enter the lattice would contribute to polymerization dynamics by opposing incorporation into the lattice. The lack of substantial change in the observed concentration-dependence of elongation rates could indicate that the β:T238A mutations do not affect the propensity for αβ-tubulin to 'straighten' on a GTP lattice. However, this is not consistent with increased spontaneous nucleation of β:T238A αβ-tubulin in the presence of GTPγS, which indicated that the mutation did affect conformational transitions that occur in/on a GTP lattice. It could be that we did not observe substantial effects on elongation because the energetics of curved to straight transitions on the microtubule end are not rate-contributing for elongation, perhaps because these transitions occur subsequent to end binding.

The significant mutant-induced structural changes in the lattice were not accompanied by equivalent changes in the conformation of unoligomerized αβ-tubulin. The differential response to the mutation inside and outside of microtubules (Figure 2.7A,B) is consistent with the view that the curved conformation represents the 'ground state' of αβ-tubulin independent of nucleotide state (Ayaz et al., 2012; Buey, Diaz, & Andreu, 2006; Nawrotek, Knossow, & Gigant, 2011; Pecqueur et al., 2012; Rice et al., 2008)), that the nucleotide acts across the longitudinal interface (Rice et al., 2008; Nawrotek et al., 2011), and that nucleotide-dependent interactions with the microtubule lattice are what drive αβ-tubulin conformational transitions (Rice et al., 2008; Buey et al., 2006; Nawrotek et al., 2011). Indeed, the changes we observed can largely be

explained by an impaired allosteric response to GDP in the lattice. It will be interesting to discover in future work if other mutations in β-tubulin can straighten unpolymerized αβ-tubulin or modulate the allosteric response(s) to nucleotide in the lattice, and to determine if mutations in α-tubulin can yield similar effects.

In summary, we showed that buried mutations of or near β:T238 alter the allosteric response to GDP in the microtubule lattice, with dramatic consequences for catastrophe frequency and shrinking rate. By describing microtubules with identical interface composition that nevertheless undergo strikingly different polymerization dynamics, our data demonstrate that allostery in the lattice dictates functionally important aspects of microtubule polymerization dynamics (Figure 2.7C). Based on the central role of allostery in controlling the frequency of catastrophe and the rate of shrinking, we speculate that cooperative conformational linkage in the lattice amplifies the individual response to nucleotide. Together, the allosteric response to GDP and the intrinsic bias of αβ-tubulin toward the curved conformation elevate and separate the threshold concentrations for persistent elongation and for spontaneous nucleation (Figure 2.7C), and underlie the fast shrinking rate that makes catastrophe more decisive. These allosteric contributions to microtubule dynamics make microtubules more amenable to regulation by cellular factors that enhance elongation, trigger catastrophe, and promote nucleation.

II. Exploring the structure and function of β: T238A microtubules using human tubulin

Abstract

Microtubules switch randomly between phase of growing and shrinking, a property called dynamic instability that is essential for proper microtubule function. Dynamic instability is controlled by the GTPase activity of tubulin subunits in the lattice, which cycle through multiple conformations as they enter and exit the polymer. Does this conformational cycle dictate microtubule dynamics, or is it simply a consequence of microtubule dynamics? Recently, our group published insight into this question by characterizing a point mutation in yeast β-tubulin, T238A, that strongly reduced microtubule shrinking rate and catastrophe frequency. Using EB-binding and other biochemical assays, we discovered that altering the strength of the allosteric response to GDP in the lattice retunes microtubule dynamics. To determine whether our observations in yeast tubulin generalize to other tubulins, we produced recombinant human tubulin containing the equivalent mutation. Initial characterization of the polymerization dynamics of the mutant human microtubules revealed similar dynamic changes as previously seen for *S. cerevisiae* microtubules: substantial decrease in catastrophe frequency and shrinking rate with little effect on elongation. To determine the structural basis of these effects, I am working towards solving high-resolution cryo-EM structures of both wild-type and β: T238A mutant human microtubules in various nucleotide states. Determining the exact structural changes that occur in β: T238A microtubules will guide an understanding of how the conformational cycle controls dynamics and how these changes influence conformational-specific binding partners, such as the EB1-family proteins.

Experimental Procedures

Protein Expression and Purification

Plasmids to express wild-type human αβ-tubulin with a single, TEV cleavable H6-tag the C-terminus of β-tubulin in the pFastBacDual vector were generously gifted from the Kapoor Lab (Rockefeller University). A plasmid to express the T238A mutation in human β-tubulin was made by QuikChange mutagenesis, using the human β-tubulin construct as a template and with primers designed according to the manufacturer's instructions. The integrity of all constructs were confirmed by DNA sequencing. The construct for EB1-GFP was generously loaned from the Kapoor Lab (Rockefeller University).

Human TubA1B (non-tagged) and Tubb3 (C-terminal TEV site and His6 tag) in pFastBacDual were used to make recombinant bacmid by transforming plasmids into DH10Bac competent cells and plating on LB/Kanamycin/Gentamycin/Tetracycline/ IPTG/X-gal plates to perform a blue-white screen. Plates were incubated for 48 h, 37°C and white colonies were harvested from plate and inoculated into liquid culture in LB media with identical additives as in plate. Cultures were grown for 48 h, 37°C, 200 rpm. Bacmid was extracted using Maxi Prep Kit (Qiagen) and transfected into Sf900 Insect cells to make baculovirus. For expression, 20 mL of P2 baculovirus was transfected into 1L Tni Insect Cells at a density of 2 x 10^6 cells/mL. Cultures were incubated for 40-42 hrs, 27°C, 190 rpm. Pellets were then harvested by centrifugation and washed/frozen with PBS (137 mM NaCl, 2.7 mM KCl, 10 mM Na_2HPO_4, 1.8 mM KH_2PO_4).

Frozen cell pellets of human tubulin were thawed in room temperature water bath. Three times the volume of lysis buffer (25 mM HEPES pH 7.4, 30 mM Imidazole, 1 mM $MgSO_4$, 500 mM NaCl, 50µM GTP) to pellet mass was added and mixture was incubated on ice for 20 min.

Cells were transferred to glass douncer and cracked open using pestle B for 40 full strokes. Lysates were centrifuged at 18k rpm, 4°C for 30 min. Supernatant was loaded onto a 5 mL Ni column, pre-equilibrated in lysis buffer. After loading, the Ni column was washed in 100 mL of high salt buffer (50 mM HEPES pH 7.4, 30 mM Imidazole, 10 mM $MgSO_4$, 500 mM NaCl, 50µM GTP) followed by a wash in 100 mL low salt buffer (25 mM PIPES pH 6.9, 30 mM Imidazole, 1 mM $MgSO_4$, 50 µM GTP). Samples were eluted over 6 column volumes (CV) in elution buffer (25 mM PIPES pH 6.9, 300 mM Imidazole, 1 mM $MgSO_4$, 50 µM GTP). To cleave the H6 tag from the sample, TEV protease was added to the Ni pool to a final concentration of 0.2 mg/mL. The sample was mixed thoroughly and incubated on ice for 2 hrs. Prior to loading onto a SourceQ ion exchange column, the cleaved sample was filtered through a 0.45 µm syringe filter. Filtered sample was loaded onto a 4 mL SourceQ column, equilibrated in 20% buffer B (buffer A: 25 mM PIPES pH 6.9, 1 mM $MgSO_4$, 2 mM EGTA, 50 µM GTP; buffer B: buffer A + 1M NaCl). A gradient was run from 20-60% over 10 CV with clean tubulin eluting near ~40%B. Peak fractions were pooled, concentrated to ~15 µM and dialyzed into BRB80 (80 mM PIPES pH 6.9, 1 mM $MgCl_2$, 1 mM EGTA, 50 µM GTP) using a 2mL, 7K MWCO Zeba spin desalting columns (Thermo Scientific) and flash frozen for storage at -80°C.

Expression and purification of EB1-GFP was performed similar to previous description (Forth et al. 2014 Cell). Expression of EB1-GFP was induced in the BL21(DE3) string of *E. coli* with 0.5 mM IPTG for 4 hrs at 18°C and harvested. Single pellets were resuspended in 50 mM Na_2HPO_4, 300 mM NaCl, 40 mM imidazole and sonicated for 30 min in the presence of PMSF. Lysates were clarified by centrifugation. Cleared lysate was loaded onto a His60 Superflow Column (Clontech) and the final sample was eluted in 250 mM imidazole. Elution samples were loaded over an S200 10/300 25 mL column, equilibrated in BRB80 (80 mM K-PIPES, pH 6.9, 1

mM $MgCL_2$, 1 mM EGTA) with 150 mM KCl. Samples at the correct elution volume based on molecular weight standards were pooled, analyzed by SDS-PAGE and concentrated using a 4 mL, 30 kDa MWCO concentrator. Samples were cleaved with TEV protease overnight at 4°C while rotating in the presence of 1 mM TCEP and 5:1 TEV: EB1-GFP. The following day, cleavage samples were hard spun and passed over a His60 Superflow Column, where the cleaved EB1-GFP elution was collected, pooled and re-concentrated. Samples were dialyzed into RB100 using a 2mL, 7K MWCO Zeba spin desalting columns (Thermo Scientific) and flash frozen for storage at -80°C.

Dynamic Assays with Human Tubulin and EB1-GFP

To monitor microtubule dynamics, *in vitro* reconstitution microscopy assays were performed. GMPCPP-stabilized seeds were used as the seeding substrate. A 5:1:1 mixture of unlabeled animal tubulin, Alexa 647-labeled animal tubulin and biotin-labeled animal tubulin (all purchased from PurSolutions) were polymerized in 1X PEM (100 mM PIPES pH 6.9, 1 mM EGTA, 1 mM $MgSO_4$) with 2 mM GMPCPP. Samples were allowed to polymerize for a minimum of 2 hrs at 37°C before use.

Flow chambers were prepared as follows. Streptactin-HRP Conjugate (BioRad, 1:100 in BRB80) was incubated in the chamber for 10 min, followed by incubation with 1% Pluronic F-127 in BRB80 for 5 min, followed by a wash with warm BRB80 (maintained at 37°C). GMPCPP-stabilized animal MTs were introduced into the chamber and incubated for 10 min, followed by a wash with warm BRB80 to remove unbound MTs. Solutions containing a range of wild-type or β: T238A concentrations in assay buffer (1X BRB80, 1 mM GTP, 0.2 mM

$MgCl_2$ 0.1 mg/mL BSA, .1% methyl-cellulose, 50 mM KCl) were then introduced into the chamber which was sealed with VALAP (Vaseline, lanolin and paraffin mixture). For assays in the presence of EB1-GFP, the chamber and samples were prepared as described above, with the addition 50 nM EB1-GFP and an oxygen scavenging system to the assay buffer (antifade reagents include glucose, glucose oxidase and catalase) (Gell et al., 2010).

Control samples in the absence of EB1-GFP were monitored under differential interference contrast (DIC) microscopy using an Olympus IX81 microscope (Olympus Optical) with a U Plan ApoS 100X/1.40 numerical aperture objective lens and DIC prisms with illumination at 550 nm. Images were taken on a Photometrics Prime 95B CMOS camera (Photometrics Cameras). All reactions were temperature controlled at 30°C using a WeatherStation temperature controller with enclosure fit to the microscope's body. Micro-Manager 2.0 (Edelstein, Amodaj, Hoover, Vale, & Stuurman, 2010) was used to control the microscope. Images of MTs were taken in continuous streaming mode for 30 minutes (~18000 images). During image acquisition, images were averaged in batches of 10 using MicroManager's 'On the Fly' FrameCombiner plug-in (Edelstein et al., 2010) to improve signal:noise. 200 defocused background images were taken at the end of each movie to be used in background correction. During data processing, the intensity for all images were normalized to the mean; the entire movie was then divided by the background. A flat-field image was by applying a Gaussian filter to the original background image. This flat-field image was then used to correct for temporal illumination variation over the course of acquisition. Kymographs were created in ImageJ (Schneider, Rasband, & Eliceiri, 2012) using the ReSlice function. Growth rates and shrinking rates were manually calculated by measuring the change in microtubule

length over time. Catastrophe frequency was calculated as the number of observed catastrophes divided by the sum total of lifetimes

Interactions of EB1-GFP with human MTs were imaged by total internal reflection fluorescence microscopy using an Olympus IX81 microscope with a TIRF ApoN 60x/1.49 objective lens, a 491 nm 50 mW solid-state laser (Olympus) and Photometrics Prime 95B CMOS camera (Photometrics Cameras). Samples were temperature controlled at 30°C and the microscope was operated as described above. Images of MTs under TIRFM conditions were taken every 5 sec from 15-20 min. Kymograph images were created in ImageJ (Schneider et al., 2012) using the ReSlice function to determine EB1 location and behavior on dynamic human microtubules.

Cryo-EM Sample Preparation and Grid Freezing

To prepare GMPCPP stabilized microtubules, wild-type or β:T238A human tubulin was polymerized in 1X PEM (100 mM PIPES pH 6.9, 1 mM EGTA, 1 mM $MgSO_4$) with 2 mM GMPCPP. Initial samples also included 4% DMSO. Samples were allowed to polymerize at 37°C for 30 min before being applied to grid. To prepare dynamic, GDP microtubules, wild-type or β:T238A tubulin was polymerized in 1X PEM (described above) with 2 mM GTP; initial samples also included 4% DMSO. If DMSO was present, samples were incubated at 37°C for 2 hrs; if DMSO was not present, samples were incubated at 37°C for 20 min. Cryo-EM grids were prepared by applying 3 µL of microtubules to a glow-discharged Quantifoil R1.2/1.3 300-mesh gold holey carbon grid (Ted Pella Inc.) and blotted for 4.5-5.0 s under 100% humidity at 30°C before being plunged into liquid ethane using a Mark IV Vitrobot (FEI).

Cryo-EM Imaging and Analysis

Preliminary data sets of wild-type human tubulin, with GTP and DMSO, and β:T238A human tubulin, with GTP and DMSO, were collected on a Talos Arctica microscope (FEI) operated at 200 kV with a K2 Summit direct electron detector (Gatan). Serial EM software (David Mastronarde, J. Richard McIntosh, http://bio3d.colorado.edu/SerialEM/) was used to manually collect micrographs. Images were recorded at 28,000X magnification using a defocus from -1.5 µm to -3 µm. All micrographs were dose-fractionated to 20 frames with a dose rate of about 6 electrons per pixel per second, with a total exposure time of 10 s. Micrographs were processed using RELION v2.1 (Scheres, 2012): images were motion corrected using MotionCor2 and dose-weighting, and CTF estimation was performed using CTFFIND4. Particles were manually picked on ~15 micrographs to extract a small initial data set that was used to construct a 2D class for particle picking. A single 2D Class was selected and used as the reference model for particle picking of the entire data set. Extraction of all particles was performed such that the box size was 5 tubulin dimers in length (410Å box) and boxes were separated by a single tubulin dimer (80Å), such that each new box contained a unique tubulin dimer in the center. 2D and 3D classifications were performed, eliminating 'noisy' particles at each step. Helical symmetry was applied through 3D reconstruction steps. Using helical symmetry is non-ideal, as it will scramble α- and β-tubulins, and will reconstruct a microtubule lattice that lacks a seam and proper skew angle. Modifications to preserve the seam and separate α- and β-tubulin will be described in Chapter 4. 3D refinements of selected classes were performed to further eliminate 'junk' particles and allow for minor improvements in helical parameters to achieve higher resolution.

Micrographs of β: T238A human microtubules, polymerized in the presence of GTP with and without DMSO, were also collected on a Titan Krios microscope (FEI) operated at 300 kV with a K2 Summit direct electron detector (Gatan). EPU automated software (FEI) was used to manually collect data. Images were recorded at 130,000X under energy filter TEM settings, using a defocus from -2 to -3.5 µm. Micrographs were dose-fractionated to 30 frames, with a dose rate of approximately 5 electrons per pixel per second, with a total exposure time of 15 s. Micrographs were processed using RELION v2.1 as described above to determine data quality. Once it was determined data quality was high (yielding reconstructions with resolution higher than 4Å), a new approach to solving 3D reconstructions will be worked through and implemented, based on work from the Nogales lab (Zhang & Nogales, 2015).

Results

β:T238A in human tubulin preserves hyperstability of the microtubule lattice

To determine how the mutation affected microtubule dynamic instability, we measured polymerization dynamics of human wild-type and human β :T238A mutant tubulin *in vitro* using time-lapse DIC microscopy (Figure 2.8A). Dynamic microtubules were grown from stabilized GMPCPP animal seeds adhered to a coverslip. Characterization of wild-type human microtubules revealed growth rates with a slope of 0.091 µm/min/µM and catastrophe frequencies near 0.15 per min, or roughly 9 catastrophes per hour (Figure 2.8B, C, blue). Wild-type microtubules exhibited a fast shrinkage rate of 56 µm/min (Figure 2.8D, blue). These characterizations are similar to previously published data (Ti et al., 2016) and provide a baseline with which to compare mutant data.

β: T238A tubulin shows robust spontaneously nucleation at higher concentrations preventing direct comparisons at identical concentrations. We therefore measured the dynamic properties of β: T238A microtubules at lower concentrations relative to wild-type in order to ensure that spontaneous nucleation did not prevent controlled growth from seeds. β: T238A exhibited an altered growth rate relative to wild-type, with a fit slope of 0.32 μm/min/μM (Figure 2.8B, red). Shifts in the growth rate parameters indicate changes in the biochemistry of elongation, in this case consist with an increased k_{on} as evidenced by dramatic changes in the slope of the line. These differences may reveal the formation of stronger lattice contacts allowing for more efficient assembly into the microtubule lattice. Catastrophe frequencies for this mutant were approximately 30-fold lower than wild-type, at only 0.0046 per minute, or approximately 1 catastrophe every 4 hours (Figure 2.8C, red). Shrinking events following the switch to catastrophe was notably slower than wild-type, with microtubules shrinking at a rate of ~3 μm/min (Figure 2.8D, red). This demonstrates an almost 20-fold decrease in the shrinking rate when compared to wild-type data, consist with hyper-stabilization of the microtubule lattice. These findings demonstrate that, as previously seen in yeast tubulin, the β:T238A mutation in human tubulin also results in hyperstabilizing the microtubule lattice against catastrophe. This is evidenced by a decrease in the catastrophe frequency and significantly slower shrinking rates that are approximately 30-fold slower than wild-type samples.

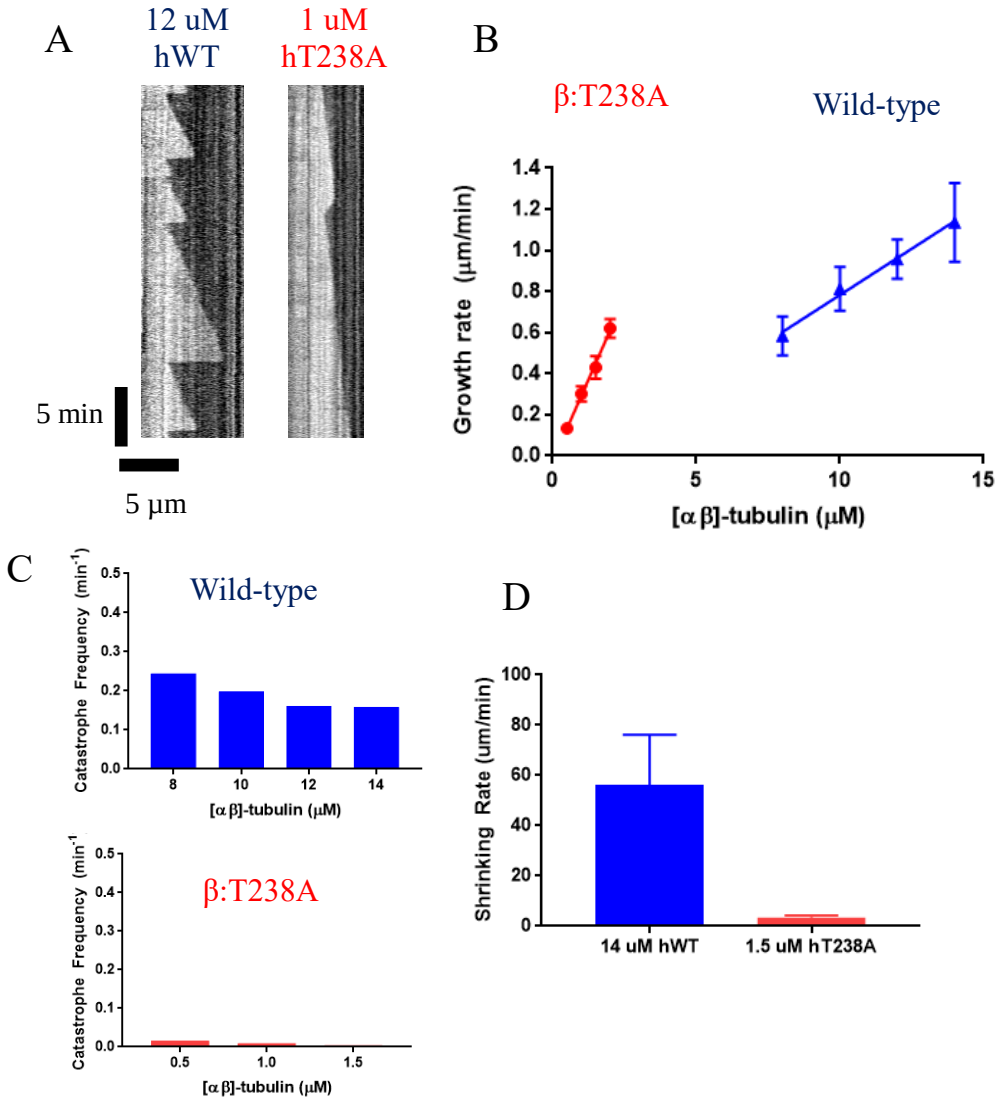

Figure 2.8: The β:T238A mutation hyperstabilizes human microtubules by lowering the catastrophe frequency and decreasing the rates of shrinking. A. Kymographs of dynamic wild-type (left) and mutant (right) microtubules under DIC assays. Note the presence of several fast shrinking events in wild-type samples but few, slow shrinking events in mutant samples. Scale bar is 5 min (y) and 5 µm (x). B. Mutant (red) and wild-type (blue) human microtubules do not show similar concentration-dependent growth profiles (slopes: 0.091 +/- 0.01 µm/min/µM for wild-type, 0.32 +/- 0.2 µm/min/µM for β:T238A, differences between slopes are statistically significant; x-intercepts: 1.3 µM for wild-type, 0.08 µM for β:T238A this difference is statistically significant; significance of differences in regression parameters was evaluated using GraphPad Prism) N = 40; bars show STD. C. T238A microtubules (bottom, red) undergo catastrophe less frequently than wild-type (top, blue). Catastrophe frequencies, in both samples, decrease as a function of concentration. D. T238A microtubules (right, red) show a ~30-fold slower rate of post-catastrophe shrinking (bars show STD) in comparison to wild-type microtubules (left, blue)

β: T238A mutation works through a unique mechanism on human microtubules

EB1-family proteins bind with high affinity to specific conformational states of the microtubule lattice. I used the human EB1-GFP to probe the conformation state of our human wild-type and mutant microtubules. Wild-type human microtubules showed the formation of a classic EB1-comet structure on the growing microtubule end (Figure 2.9A). This is consistent with EB1 binding to its high-affinity 'compacted and twisted' conformational state in the microtubule lattice. These findings have also been shown in published data from numerous labs (Maurer et al., 2012; Zhang et al., 2015). In our prior work using yeast tubulin and the yeast homologue Bim1, assays with dynamic β: T238A microtubules revealed Bim1 lattice coating under conditions where Bim1 comets were present in wild-type yeast tubulin samples. Strikingly contrary to this result, β: T238A human microtubules revealed comet structures with no lattice coating (Figure 2.9B). The presence of comets were independent of assay buffer conditions including changes to potassium chloride (KCl) concentration, the addition of dimethyl sulfoxide (DMSO) and the removal of methylcellulose (data not shown). In human tubulin, although the mutation elicits a stabilizing effect to the lattice, it does not appear to be grossly perturbing the conformational cycle in the body of the microtubule, nor does it appear to have uncoupled the conformational cycle from nucleotide hydrolysis. Instead, the mutation in human tubulin must be working by a unique mechanism that will be further speculated on in the discussion below. This result is critical in that it reveals that the mutation is still produces lattice stabilization, but may indicate the presence of a distinct mechanism of stabilization that may not be fully conserved across species. Alternatively, the mechanism of stabilization may be conserved, but the change we saw in yeast tubulin was highlighting a differential property specific to yeast. We must now explore different avenues to determine the stabilizing function of the mutation in human tubulin.

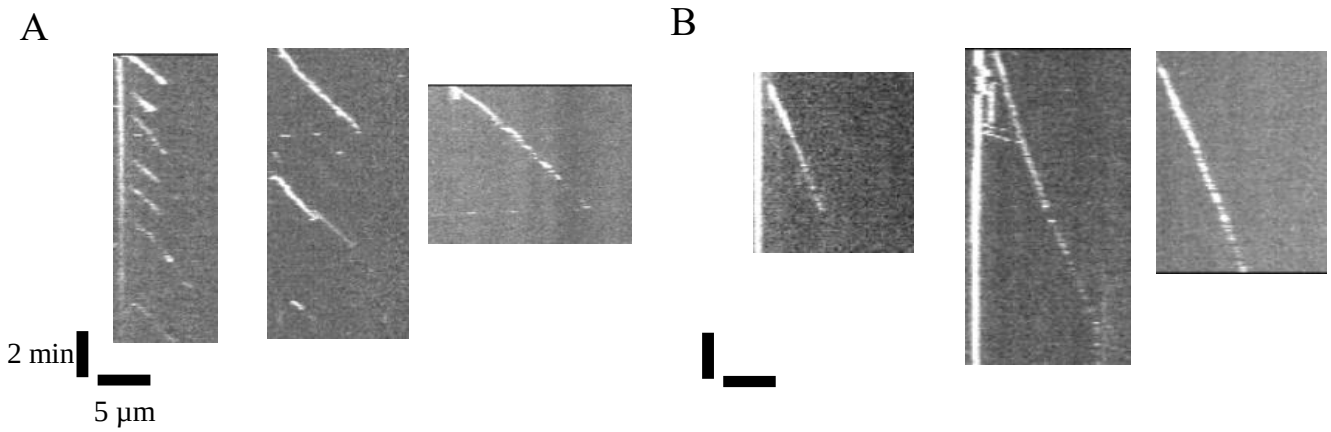

Figure 2.9: EB1-GFP comets are present on both dynamic wild-type and β:T238A human microtubules. A. Kymographs from TIRFM experiments were constructed from samples containing 12 µM wild-type human tubulin and 50 nM EB1-GFP reveal the presence of end comets on growing microtubule ends. Microtubules are growing from the seed at the left side of the image to the right. Scale bar is 2 min (in y) and 5 µm (in x). B. Contrary to Bim1-GFP on β:T238A yeast microtubules, human EB1-GFP produces end comet structures on dynamic, human β:T238A microtubules. Kymographs were constructed from samples containing 2 uM β:T238A human tubulin and 50 nM EB1-GFP. Scale bar is identical from A.

Preliminary reconstructions of wild-type and mutant microtubules

Previous biochemical studies with yeast tubulin pointed to the idea that the mutation was inducing lattice stabilization by delaying structural changes that normally accompany GTP hydrolysis. I prepared cryo-EM grids of dynamic, GTP microtubules for wild-type and β:T238A human microtubules to determine whether we could see mutant-induced structural changes in the 'GDP' lattice state. In both of these data sets, the tubulin samples are His-tagged on β-tubulin. Initial data sets of both wild-type and mutant microtubules were collected on a Talos Arctica with Gatan K2 Direct Detector; later samples of β:T238A in the presence and absence of DMSO were collected on a Titan Krios with Gatan K2 Direct Detector.

Initial helical reconstructions for both wild-type and β:T238A human microtubules (containing His-tag on β-tubulin) from the Talos Arctica yielded 14-protofilament microtubule lattices with the following fit RELION helical parameters after 3D refinement: 5.91 Å rise and -257.17° twist for wild-type, 5.89 Å rise and -257.17° twist for β:T238A. Converting these parameters from RELION's form to biochemical properties results in a dimer rise of 83.6 Å and a twist of -25.7°. This is consistent with a 14-protofilament microtubule and a lattice that appears to be in a more expanded state. These early wild-type and β:T238A structures were refined to resolutions of 4.5 Å for wild-type and 5.8 Å for T238A, respectively. Although these initial data sets were useful in allowing me to gain a familiarity with data collection and processing using RELION, they were not ideal because the samples included a stabilizing reagent, DMSO. We were concerned that the presence of DMSO may have altered the lattice structure or parameters of the microtubules. Testing our samples in dynamic assays allowed us to determine the right buffer conditions under which we could see dynamic instability and microtubule growth without

the need for DMSO. I then used these refined conditions to make new sets of grids, focusing on collecting higher quality data for our mutant microtubules.

New, higher quality data sets taken on the Titan Krios of β:T238A microtubules (also contain His-tag on β-tubulin) without DMSO demonstrated improved resolution and similar fit helical parameters. Microtubule density on the grids was good, with a higher number of microtubules in every image but without too many overlapping segments that are not able to be used for particle extraction (Figure 2.10A). Extraction of particles, boxes containing five tubulin dimer with a box spacing of 80Å, yielded approximately 52,000 particles. Analysis of the β:T238A dataset in GTP without DMSO revealed relatively high signal to noise 2D class averages (Figure 2.10B) and produced a reconstruction of a 14-protofilament lattice with fit RELION helical parameters of 5.9 Å rise (83.6Å dimer rise) and -257.17° twist (-25.7°) (Figure 2.10C). After minimal rounds of 3D refinement, the current helically reconstructed lattice has a calculated average resolution of 3.8 Å (as determined by FSC at 0.143, Figure 2.10D).

The data we have collected here are a promising start, but further refinements and modifications are still required (this will be discussed further in Chapter 4). While the lattice parameters of all data sets currently indicate an expanded lattice, comparisons of GMPCPP equivalent data sets are needed. Additionally, all of the samples we have analyzed so far contain a C-terminal His-tag on β-tubulin. In the dynamic assays and EB1-comet assays described above the tubulin samples have been cleaved and no longer contain a His-tag on β-tubulin, as differences were seen in dynamic instability in the absence and presence of the tag (data not shown). Data sets on the untagged wild-type and β:T238A data sets need to be collected and reconstructed to determine if the tag is influencing microtubule structure.

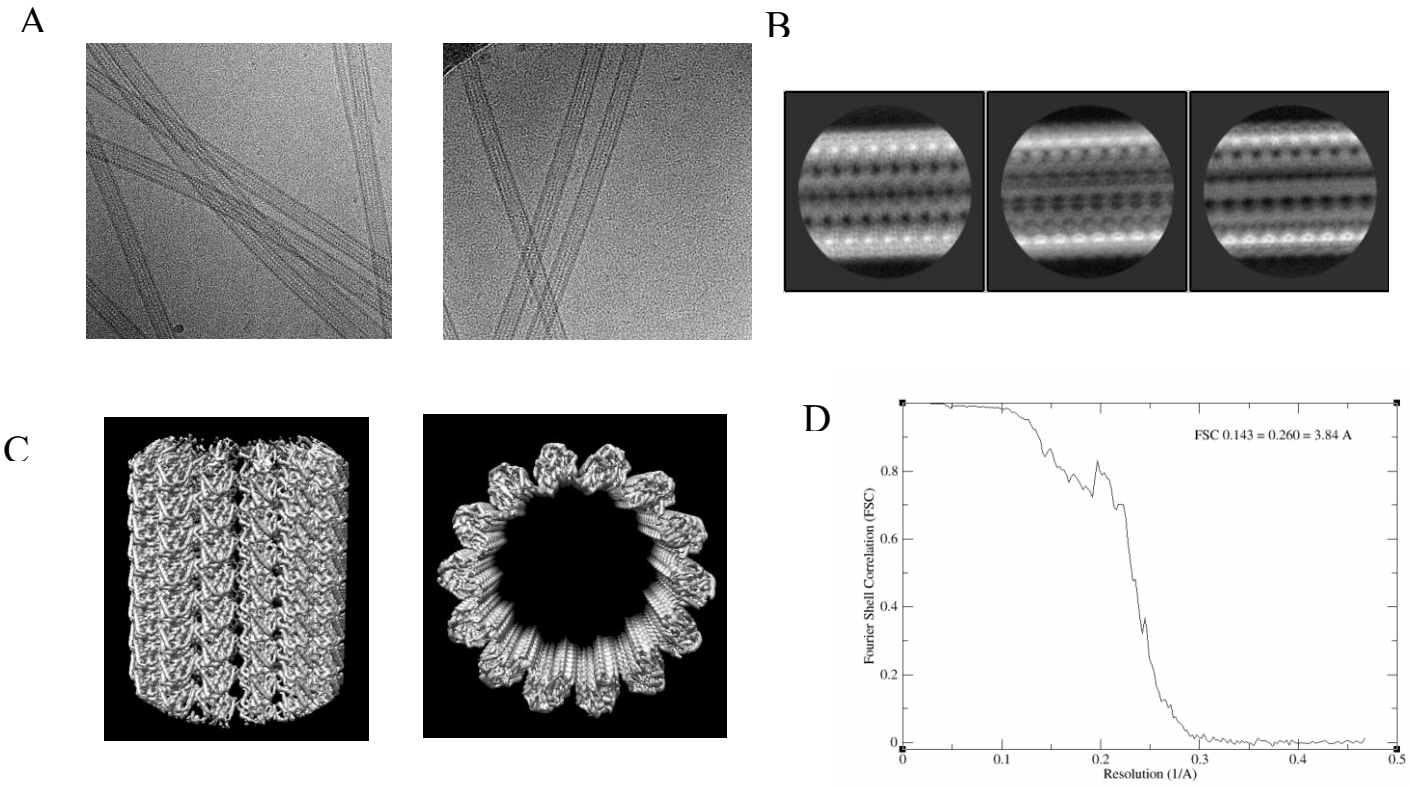

Figure 2.10: Initial cryo-EM characterization of β:T238A human microtubules in 'GTP' after helical reconstruction in RELION 2.1. A. Micrographs demonstrate high data quality and good sample preparation, as there are a high number of disperse microtubules and no visible ice or grid defects. B. 2D class averages from RELION 2.1 show high signal to noise of small data subset. These 2D classes were used for particle picking and extraction by RELION. C. 3D reconstruction of β:T238A human microtubule demonstrates that the structure is high resolution and contains 14-protofilaments (image on right). Because this structure was solved using helical symmetry reconstructions, α- and β-tubulin have been mixed and there is no seam. All of these artifacts result in a lower overall resolution. D. Fourier shell correlation analysis from 3D refinement runs estimate the average resolution of the structure to be near 3.8 Å (FSC 0.143)

Discussion

Here, we have shown that the mutation of a highly conserved tubulin residue (β:T238A) produces hyperstable microtubules in both lower eukaryotic (*S. cerevisiae)* and higher eukaryotic (human) systems. This mutation was originally discovered in yeast genetic screens (Thomas et al., 1985) and our *in vitro* characterization of this mutant tubulin was performed using yeast tubulin proteins. To determine whether the hyperstable phenotype of the mutation was universal, we have now characterized the identical mutation using human tubulin proteins expressed in insect (Tni) cells. Analysis of the mutation using *in vitro* reconstitution methods to study the properties of dynamic instability revealed that the effects of the mutation are conserved across species. β:T238A resulted in microtubules that were highly resistant to catastrophe (Figure 2.8C). When mutant microtubules do undergo a catastrophe, the shrinking events following the switch into catastrophe were almost 30-fold slower than wild-type human microtubules (Figure 2.8D). These results are very similar to those using yeast tubulin (Figure 2.1). Contrary to our findings in yeast, the growth rates of human wild-type and mutant microtubules differed in a statistically significant manner, such that the slopes of the growth rates as a function of concentrations yielded unique fit k_{on} parameters (Figure 2.8B). The abundance of spontaneous nucleation products at relatively low concentrations, in both yeast and human mutant samples, are consistent with the idea that polymer contacts in β:T238A occur more favorably and more stably. Overall, conservation of hyperstable microtubules between yeast and human samples reveals that the mutation functions in a universal manner.

Although the hyperstable phenotype appears to be conserved across species, it will be crucial to dissect the mechanism by which the mutation is functioning in human to determine whether there are species-specific differences, or if differences in our current data sets reflect

some additional, non-essential behavior that occurs solely in yeast microtubule dynamics. Differences in the binding of the EB1 family proteins to the mutation show that EB1 interactions that are sensitive to the tubulin variant. Our studies of β:T238A in yeast revealed that in the presence of Bim1, the EB1 yeast homologue, where wild-type yeast microtubules produced a Bim1 comet, mutant microtubule lattices were completely coated in Bim1. EB1-family proteins tightly bind the compacted and twisted intermediate conformation in the microtubule lattice, and bind with very low affinity to other lattice conformations. Therefore, experiments with yeast microtubules and Bim1 demonstrated that the mutation was working to stabilize the lattice by preventing the necessary conformational changes into a fully compacted state following GTP hydrolysis. Our studies using human tubulin, however, reveal that EB1 forms comets in the presence of both wild-type and β:T238A mutant samples. These data suggest that there are no dramatic conformational changes in the body of human mutant microtubules.

There are several possible avenues that may explain these differences. The mechanism of β:T238A hyperstability in human microtubules may more strongly impact the end structure of the microtubule, rather than the conformational state throughout the microtubule lattice. Here, I would not expect to see changes in EB1 binding. Instead, I would anticipate more 'blunt' end microtubule structures in the mutant samples when compared with wild-type microtubules, which may be more 'ragged' in appearance with longer protofilaments growing in many directions at the plus end. This would be consistent with the idea that the mutation makes it 'easier' to incorporate into the lattice, possibly by forming stronger lateral interactions. Because the mutation creates a pocket in the cavity of β-tubulin, transitions through the conformational cycle from expanded to compacted in the lattice may still occur, but produce less overall strain on αβ-tubulin. The mutant microtubules then become very stable, lacking an increase in strain to

help drive them from the microtubule lattice and back into a low energy curved conformation. Alternatively, it may be that changes to the conformational cycle, or the coupling of the conformational cycle to GTP hydrolysis may still exist, but for some reason yeast lattices are much more sensitive to small perturbations and elicit a larger overall response. As we have not yet carefully measured the comet sizes between wild-type and β:T238A human microtubules in the presence of EB1, it could be that in the mutant, the EB1 comets are slightly longer in length without completely coating the microtubule lattice. We may have not yet seen these small differences in comet size because so far we have been anticipating that the mutant lattice would become completely coated with EB1. Finally, there are subtle differences in the binding sites between the EB1 and Bim1 proteins (Howes et al., 2017) that may impact the overall read out of these experiments. It was shown that while EB1 primarily binds at the intersection of four tubulin dimers, Bim1 binds between *and* among tubulin dimers (Howes et al., 2017). This allows Bim1 to bind to twice as many sites as EB1. Given this, and coupled to the possibility that small perturbations in yeast may elicit larger allosteric changes, it is possible that these two factors may over amplify the effect of the mutation in yeast, resulting in lattice coating by Bim1. Further studies looking at the interaction of tubulin dimers at the microtubule end, and the overall plus end architecture, will be needed to elaborate the mechanism of action of β:T238A in human tubulin.

High resolution structures of wild-type and mutant human microtubules will allow us to gain insight into any conformational changes that may be occurring in the mutant. My preliminary microtubule data sets, analyzing both wild-type and β:T238A samples, are a very promising start, as the sample and grid conditions have been optimized to produce reliable preparations that yield high quality data. The resolution we obtained from performing a 3D

helical reconstruction estimates that the overall structures range from 3.8-6 Å (dependent on structure, sample conditions and imaging system). Although this approximates the samples to produce fairly high resolution reconstructions, the resolutions estimated from our current helical reconstructions are actually an underestimation. By using helical symmetry to reconstruct the microtubule lattice, RELION cannot separate α- and β-tubulin because the low resolution features that the program uses to drive the alignment are not distinct enough to distinguish the two tubulin monomers. 'Scrambling' the tubulin monomers and averaging them together incorrectly lowers the overall resolution of the reconstruction. Additionally, helical symmetry assumes the microtubule is a perfect helix, which it is not. The presence of the seam breaks the perfect helical symmetry. Now that we are confident in our data collection and analysis abilities and have high quality data that will yield a high resolution structure, we need to modify our 3D reconstructions to prevent mixing of α- and β- tubulin, and to determine the proper location of the seam in the microtubule lattice. This will allow us to reconstruct a microtubule that is 'biologically relevant' in the sense that the tubulin monomers are unique entities and the microtubule contains a seam, as it does *in vivo*. I will describe how we are altering our reconstruction algorithm in depth in Chapter 4.

CHAPTER THREE

Design Principles of a Microtubule Polymerase

There are a large number of microtubule associated proteins *in vivo,* each functioning in a unique way to regulate microtubule structure and function. For example, certain kinesins, such as MCAK and Kip3, function as microtubule depolymerizers and regulate microtubule length at mitotic spindles. Other proteins, such as the yeast rescue factor Stu1 (suppressor of tubulin, 1) allow for the growth of longer, more stable microtubules as it promotes the transition from shrinking back into a growth phase (Majumdar et al., 2018). One such group of proteins that alter microtubule dynamics *in vivo* are the XMAP215/Stu2 family. XMAP215, the higher eukaryotic Xenopus homologue, has been characterized *in vitro* and shown to function as a microtubule polymerase, utilizing its tubulin-binding TOG domains to increase the growth rates of microtubules. A less studied member of this family is the *S. cerevisiae* homologue, Stu2. Although Stu2 and XMAP215 behave analogously by increasing the growth rates of microtubules, little work has been done to understand how the full-length proteins function from a highly detailed mechanistic view. Prior work from our lab investigated the structure and activity of each of the separate TOG domains of Stu2 (TOG1 and TOG2) (Ayaz et al., 2014; Ayaz et al., 2012). While these results were critical in the process to dissecting the action of these proteins, Stu2 is composed of and requires many more features, in addition to TOG domains, to act as a microtubule polymerase. In this chapter, I will discuss my work using mutational analysis and *in vitro* reconstitution to quantitatively dissect the underlying molecular mechanism of the full-length yeast microtubule polymerase, Stu2.

The work in this chapter was re-produced from:

Geyer, E. A., Miller, M. P., Brautigam, C. A., Biggins, S., & Rice, L. M. (2018). Design principles of a microtubule polymerase. *Elife, 7*. doi:10.7554/eLife.34574

Abstract

Stu2/XMAP215 microtubule polymerases use multiple tubulin-binding TOG domains and a lattice-binding basic region to processively promote faster elongation. How the domain composition and organization of these proteins dictate polymerase activity, end localization, and processivity is unknown. We show that polymerase activity does not require different kinds of TOGs, nor are there strict requirements for how the TOGs are linked. We identify an unexpected antagonism between the tubulin-binding TOGs and the lattice-binding basic region: lattice binding by the basic region is weak when at least two TOGs engage tubulins, strong when TOGs are empty. End-localization of Stu2 requires unpolymerized tubulin, at least two TOGs, and polymerase competence. We propose a 'ratcheting' model for processivity: transfer of tubulin from TOGs to the lattice activates the basic region, retaining the polymerase at the end for subsequent rounds of tubulin binding and incorporation. These results clarify design principles of the polymerase.

Experimental Procedures

Protein expression and purification

Plasmids to express wild-type and β:T238A yeast αβ-tubulin were previously described (Johnson et al., 2011; Ayaz et al., 2012; Geyer et al., 2015). Plasmids to express the β:F281A

mutation of Tub2p (yeast β-tubulin) and α:H284A mutation of Tub1p (yeast α-tubulin) were made by QuikChange (Stratagene) mutagenesis, using expression plasmids for wild-type Tub2 and Tub1 as template and with primers designed according to the manufacturer's instructions. Three Stu2p constructs, in pHAT vector containing N-terminal H6 tag, C-terminal eGFP-tag followed by a Strep-tag II, were a gift from Dr. Gary Brouhard: Stu2 residues 1–658 (Δcc; monomer); Stu2 residues 1–761 (Δtail; dimer, no C-terminal tail); Stu2 residues 1–888 (WT, full-length; dimer). Mutations were introduced into the monomeric (658) or fully dimeric (888) background using QuikChange (Stratagene) mutagenesis or traditional restriction-based cloning after PCR. The TOG1-TOG1 Stu2FL plasmid was made using NEBuilder HiFi DNA Assembly (New England Biolabs, Ipswich, MA). A gene block (gblock) encompassing TOG1 (residues 1–272) and the Stu2 basic domain (560-661) was purchased from IDT DNA (Coralville, IA). The 'transplanted' region encompasses the structured TOG1 domain with a C-terminal extension of ~20 additional amino acids from the linker sequence; shorter constructs that did not include this linker sequence proved to be unstable upon purification. The parent plasmid, excluding the region coding for the to-be-replaced TOG2 sequence, was amplified in a second reaction with primers sharing overlap to the gene block. The two products were mixed, incubated and transformed according to the manufacturer's instructions. The integrity of all expression constructs was confirmed by DNA sequencing.

Wild-type and all tubulin mutants (β:T238A, Δ:T175R/V179R, β:F281A, α:H284A, α:T350E) yeast αβ-tubulin were purified from inducibly overexpressing strains of *S. cerevisiae* using Ni-affinity and ion exchange chromatography, as previously described (Johnson et al., 2011; Ayaz et al., 2012, 2014; Geyer et al., 2015). Tubulin samples were stored in storage buffer for dynamics assays (10 mM PIPES pH 6.9, 1 mM $MgCl_2$, 1 mM EGTA) containing 50 µM GTP

or storage buffer for analytical ultracentrifugation experiments (25 mM Tris pH 7.5, 100 mM NaCl, 1 mM $MgCl_2$, 1 mM EGTA) containing 20 μM GTP. Expression of all Stu2p constructs, wild-type and mutant, were induced in E. coli using Arctic Express Cells with N-terminal His6 tags and C-terminal eGFP and Strep-tag II. Samples were induced with 0.5 mM IPTG for 24 hr at 10˚C. Cell pellets were resuspended in lysis buffer (50 mM Na_2HPO_4, 300 mM NaCl, 40 mM imidazole, 5% glycerol) and sonicated for 30 min in the presence of PMSF before clarification by centrifugation. Cleared lysate was loaded onto a His60 Superflow Column (Clontech) and the final sample was eluted in lysis buffer containing 300 mM imidazole. Pooled elution fractions containing Stu2 were loaded onto a 3 mL Strep-Tactin Superflow column (IBA, Germany) and eluted in RB100 (25 mM Tris pH 7.5, 100 mM NaCl, 1 mM $MgCl_2$, 1 mM EGTA) containing 5 mM desthiobiotin. For storage, final samples were exchanged into RB100 with 2 mL, 7K MWCO Zeba spin desalting columns (Thermo Scientific). Expression of purification of TOG1 domain from Stu2 ('TOG1-tail', 1–317) was previously described (Ayaz et al., 2012, 2014).

In vitro reconstitution assays using TIRFM

Flow chambers were prepared as described previously (Gell et al., 2010), with the exception that sea urchin axonemes (Waterman-Storer, 2001) were used to seed growth of yeast microtubules. Chambers were rinsed with BRB80 (80 mM PIPES pH 6.9, 1 mM $MgCl_2$, 1 mM EGTA), followed by 10 min incubation with sea urchin axonemes. Chambers were then blocked with 1% F-127 Pluronic in BRB80 for 5 min, and washed with 1X PEM (100 mM PIPES pH 6.9, 1 mM EGTA, 1 mM $MgSO_4$) containing 1 mM GTP. Reaction chambers were sealed with VALAP after addition of Stu2p and αβ-tubulin samples.

Samples of Stu2p wild-type or mutant proteins, along with wild-type or β:T238A yeast αβ-tubulin were prepared in imaging buffer (1X PEM +50 mM GTP +0.1 mg/mL BSA +antifade reagents (glucose, glucose oxidase, catalase) (Gell et al., 2010) A subset of samples were performed in the presence of either 50 mM GTPγS in place of GTP, or with the addition of 1 or 4 mM epothilone-B. For the majority of experiments, Stu2 concentration ranged from 25 to 400 nM, while tubulin concentrations were kept constant throughout the experiment (either 500 nM, 800 nM, 1 μM).

Microtubule (MT) dynamics and Stu2 location/signal were imaged by total internal reflection fluorescence (TIRF) microscopy using an Olympus IX81 microscope with a TIRF ApoN 60x/1.49 objective lens, a 491 nm 50 mW solid-state laser and Hamamatsu ORCA-Flash2.8 CMOS camera (Olympus). In assays where Stu2 signal was not detectable on growing MTs or no Stu2 was present in the reaction, MT dynamics were imaged by differential interference contrast microscopy (DIC) using an Olympus IX81 microscope with a TIRF ApoN 60x/1.49 objective lens and DIC prisms. Illumination at 550 nm was obtained by inserting a bandpass filter of 550/100 nm (Olympus) in the light path. Temperature for all assays were maintained at 30˚C using a WeatherStation temperature controller with enclosure fit to the microscope's body. Micro-Manager 1.4.16 (Edelstein et al., 2010) was used to control the microscope.

In TIRF assays, MT dynamics were recorded by taking an image every 3–5 s for 15–30 min. MT growth rates were measured manually by creating kymographs using the ReSlice plugin for ImageJ (Schneider et al., 2012). From the kymographs, MT growth rates were manually measured by taking the length of the MT from the start of the Stu2 tip-tracking region at the MT end to the base of the axoneme, and repeating this measurement at a later time, t. Changes in MT

length as a function of time were then calculated. In DIC assays, MT dynamics were recorded by taking an image every 500 ms for 30 min. At the end of each movie, a set of 100 out-of-focus background images was taken for background subtraction. To improve signal to noise, batches of 10 raw images were averaged using ImageJ (Schneider et al., 2012) and intensity normalized before background subtraction. MT length was measured manually using a PointPicker plugin for ImageJ. Rates of MT elongation were determined as described previously (Walker et al., 1988). Average growth rates as a function of Stu2 concentration, for each given experiment, were then analyzed in GraphPad Prism 7.01 fitting experimental data with an altered Michaelis-Menten equation set to specify the change in overall fold offsets in growth rate. Fold-offset changes and Km values were fit parameters.

End intensity dynamic assays

Flow chambers were prepared as described above. Samples of Stu2p (wild-type or mutant) with wild-type yeast αβ-tubulin were prepared in imaging buffer. For all single molecule end-intensity experiments, Stu2 concentration was held at 5 nM and wild-type yeast αβ-tubulin was used at 1–1.5 μM. For measuring end intensity as a function of Stu2 concentration, concentrations of Stu2 between 10 and 300 nM were used; wild-type yeast tubulin concentration was held constant at 800 nM.

MT dynamics and Stu2 location were imaged at 30˚C by TIRF microscopy as described above but using an Andor EMCCD iXon (Andor) camera. Images were recorded every 3 s over a period of 10– 15 min. End intensity measurements to determine the number of Stu2 molecules at the end of a MT were all manually measured in ImageJ (Schneider et al., 2012). In single

molecule (5 nM Stu2eGFP signal tracking) Stu2 assays, all experimental data sets were background subtracted using the Mosaic Background Subtractor plugin for ImageJ (Schneider et al., 2012).

End intensity values for Stu2 at a growing MT end were measured using the Measure feature in ImageJ (Schneider et al., 2012), where the end of the MT was measured and marked by a single pixel. For experiments where populations of Stu2 molecules reside at the growing MT end (Stu2 concentrations above 5 nM), the intensity of the entire Stu2 comet at the end of a growing MT was measured using the Oval marker and Measure feature in ImageJ (Schneider et al., 2012).

Single molecule processivity assays

Flow chambers were prepared and imaged as described above. For ‘strict’ single molecule processivity experiments, Stu2 concentration was held at 5 nM and wild-type yeast αβ-tubulin was used at 1–1.5 μM. For ‘spike’ single molecule processivity experiments at higher overall Stu2 concentration, 5 nM Stu2-eGFP was added along with 195 nM unlabeled Stu2-KCK, with 800 nM wild-type yeast αβ-tubulin.

MT dynamics and Stu2 location and processivity were imaged by TIRF microscopy at 30˚C using an Andor EMCCD iXon (Andor) as described above. Images were recorded using streaming acquisition with a 100 ms exposure for 30–60 s.

End processivity times of Stu2 proteins were measured manually, by creating kymographs using the ReSlice plugin for ImageJ (Schneider et al., 2012). The length of time Stu2 was present at the end of a MT was recorded. In total, ‘strict’ single molecule wild-type

Stu2 dimer experiments were repeated over four independent experiments, with each experiment yielding 100 Stu2 end-time measurements (n = 400). For ‘saturation’ single molecule assays, experiments were repeated over two independent sets, with each experiment yielding 100 Stu2 end-time measurements (n = 200). For Stu2 mutants, experiments were repeated over two independent sets, with each experiment yielding 100 Stu2 end-time measurements (n = 200). Time measurements were then sorted by the whole second, data were converted to percentage of molecules by diving the number of molecules at each time point by the total number of molecules analyzed in the set. Percentage of molecules data was imported and analyzed using GraphPad Prism 7.01. Data sets were fit with a one phase exponential decay, constraining the fit such that the plateau must be greater than 0.

Stable MT Flow-In experiments

To prepare stable wild-type yeast MT, wild-type yeast αβ-tubulin was polymerized in the presence of 500 mM GTPγS in assembly buffer (see above). The mixture was incubated for 90 min at 30˚C.

Flow chambers were prepared as described above. Stable microtubules were attached to the cover slip using His-Tag Antibody (1:200, Gentech), which was incubated in the chamber for 10 min before blocking with 1% Pluronic F-127 in BRB80 for 5 min, followed by a wash with BRB80. Preformed, GTPγS-stabilized wild-type yeast MTs were incubated in the chamber for 10 min, followed by a wash with BRB80 to remove unbound MTs. Solutions containing a range of Stu2 concentrations, with or without free wild-type yeast αβ-tubulin in imaging buffer were mixed, incubated on ice for 10 min, then introduced into the chamber immediately prior to data

collection. MT fields were imaged at 30˚C by TIRF microscopy as described above using an Olympus IX81 microscope with a Hamamatsu ORCA-Flash2.8 CMOS camera (Olympus), to view the presence and location of Stu2- eGFP molecules; fields were also imaged by DIC microscopy as described above. Images of MTs under TIRF and DIC fields were taken every 30 s for about 5 min. MT images were viewed using ImageJ (Schneider et al., 2012).

Depolymerization experiments using this assay setup were performed as previously described (Geyer et al., 2015), using the Hamamatsu ORCA-Flash2.8 CMOS camera (Olympus). MT depolymerization was measured manually using ImageJ (Schneider et al., 2012), using the average rate of MT depolymerization over the course of imaging to determine the depolymerization rate over an hour time frame.

Binding experiments

Gel filtration binding experiments were performed by loading 500 mL samples of TOG, tubulin wild-type or mutants (α:H284A or β:F281A) or mixtures of TOG:tubulin samples onto a Shodex KW-803 column equilibrated in BRB80 (80 mM PIPES pH 6.9, 1 mM $MgCl_2$, 1 mM EGTA) with 50 µM GTP. Samples tested contained either 1 µM TOG1-tail (1-317), 1 µM tubulin wild-type or mutant alone (α:H284A or β:F281A), and 1 µM TOG1-tail with 1 µM tubulin wild-type or mutant (α:H284A or β:F281A). All samples were prepared, allowed to equilibrate on ice for 20 min and then loaded onto the column.

Samples for analytical ultracentrifugation (Stu2 TOG1-tail, wild-type yeast αβ-tubulin, ‘long-blocked’ yeast αβ-tubulin mutant β:T175R/V179R, ‘side-blocked’ yeast αβ-tubulin mutant, β: F281A) were dialyzed into final buffer conditions of RB100 (25 mM Tris pH 7.5, 1

mM $MgCl_2$, 1 mM EGTA, 100 mM NaCl) containing 20 µM GTP with a 2 mL, 7K MWCO Zeba spin desalting columns (Thermo Scientific). The samples shown in Figure 5—figure supplement 1 contain 0.3 µM WT yeast αβ-tubulin and 0.1, 0.3, 1.2, 3 µM TOG1-tail or 0.3 µM β:T175R/V179R or β:F281A yeast αβ-tubulin and 0.1, 0.3, 0.9, 1.5, 3 µM TOG1-tail. Samples were mixed and incubated at 4˚C for at least one hr prior to the experiment. All analytical ultracentrifugation experiments were carried out in an Optima XL-I centrifuge using an An50-Ti rotor (Beckman-Coulter). Approximately 390 mL of each sample were placed in charcoal-filled, dual-sector Epon centerpieces. Sedimentation (rotor speed: 50,000 rpm) was monitored using absorbance at 229 nm and centrifugation was conducted at 20˚C after the centrifugation rotor and cells had equilibrated at that temperature for at least 2.5 hr. Protein partial-specific volumes, buffer viscosities, and buffer densities were calculated using SEDNTERP (Laue et al., 1992). Data were analyzed using the c(s) methodology in SEDFIT (Schuck, 2000; Schuck et al., 2002). The distributions were integrated in GUSSI (Brautigam, 2015) and analyzed in SEDPHAT (Schuck, 2010) with a 1:1 effective-particle model, fixing the s-values of the αβ-tubulins and the TOG1-tail and allowing the s-value of the αβ-tubulin:TOG1 complex to refine.

Microtubule pelleting assays

To test the ability of lateral yeast tubulin mutants (α:H284A or β:F281A) to form MTs, experiments were performed as previously described (Geyer et al., 2015). Briefly, samples containing 1 µM of a single yeast tubulin variant, either wild-type Tub2-H6, wild-type internal Tub1-H6, Tub1:H284A or Tub2:F281A, were incubated in assembly buffer (100 mM PIPES pH 6.9, 10% glycerol, 2 mM $MgSO_4$, 0.5 mM EGTA, 50 µM GTP) at 30˚C for 90 min. Samples

were hard-spun in a pre-warmed, TLA-100 rotor (Beckman-Coulter), resuspend and analyzed by SDS-PAGE gel analysis.

Yeast strains and plasmids

Saccharomyces cerevisiae strains used in this study are described in Supplementary file 1 and are derivatives of SBY3 (W303). Construction of Stu2-3HA-IAA7 and a LEU2 integrating plasmid containing wild-type pSTU2-STU2-3V5 (pSB2232) are described in (Miller et al., 2016). Stu2 variants were constructed by mutagenizing pSB2232 as described in (Liu & Naismith, 2008; Tseng, Lin, Wei, & Fang, 2008) resulting in pSB2254 (pSTU2-STU2(D1–281)3V5, i.e. TOG1D), pSB2257 (pSTU2-STU2(D282– 550::GDGAGL)3V5, i.e. TOG2D), pSB2306 (pSTU2-STU2(R200A)3V5), pSB2307 (pSTU2-STU2 (R519A)3V5), pSB2620 (pSTU2-STU2(D12–245::321–559)3V5, i.e. TOG2-TOG2), pSB2817 (pSTU2- STU2(D326–550::1–272)3V5, i.e. TOG1-TOG1).

Spotting assay

For the spotting assay, the desired strains were grown overnight in yeast extract peptone plus 2% glucose (YPD) medium. The following day, cells were diluted to OD600 ~1.0 from which a serial 1:5 dilution series was made and spotted on YPD + DMSO or YPD + 500 mM IAA (indole-3-acetic acid dissolved in DMSO) plates. Plates were incubated at 23˚C for 3 days.

Results

Stu2 polymerase activity does not require different TOG domains or dimerization

Stu2 forms a homodimer, with each monomer containing (from N to C) a TOG1 domain, a TOG2 domain, a basic region, and a coiled-coil that mediates dimerization (Figure 3.1A). In an earlier study, we found that Stu2 variants with either TOG1 or TOG2 inactivated for tubulin-binding rescued the loss of wild-type Stu2 in a genetic assay, but monomeric forms of Stu2 showed much poorer rescue activity (Ayaz et al., 2014). These results suggested that the presence of two functional TOG domains was not always sufficient for full polymerase activity, and consequently that dimerization and/or how the TOGs were linked was essential for function. To investigate more directly how altering the design of Stu2 (number and type of TOGs, and oligomerization state) affects polymerase activity, we developed an all yeast protein *in vitro* reconstitution assay analogous to the one reported by (Podolski et al., 2014). Our assay uses sea urchin axonemes to seed yeast microtubules; the polymerization dynamics of yeast tubulin with different amounts of Stu2-eGFP variants are monitored by total internal reflection fluorescence (TIRF) microscopy (Figure 3.1B, left). Using a slightly shorter construct, and as observed by others (Podolski et al., 2014; Brouhard et al., 2008), we confirmed that the eGFP tag did not affect polymerase activity (Figure 3.1—figure supplement 1A,D). These assays revealed, consistent with prior work (Al-Bassam et al., 2006; Podolski et al., 2014), that Stu2 variants track the growing ends of microtubules (Figure 3.1B, right) and show dose-dependent stimulation of polymerization rates, reaching about 6-fold at saturation (Figure 3.1C; Figure 3.1— source data 1).

To determine whether polymerase activity depends on the number or identity of TOG domains (TOG1 versus TOG2), we measured the polymerase activity of Stu2 variants containing

R->A mutations (R200A in TOG1, denoted TOG1*; R519A in TOG2, denoted TOG2*) that inactivate the individual TOG domains for tubulin binding (Ayaz et al., 2014, 2012). Stu2(TOG1*-TOG2) yielded ~40% maximal fold-stimulation of elongation compared to wild-type (Figure 3.1C,F); Stu2 (TOG1-TOG2*) yielded ~60% (Figure 3.1C,F). Both variants retained high-affinity end-binding (Figure 3.1F), as evidenced by the hyperbolic activity vs concentration behavior. Inactivating TOG1 gives a slightly stronger effect compared to TOG2, perhaps because TOG1 binds more tightly to tubulin (Ayaz et al., 2014). Consistent with this idea, substituting TOG1 with a second copy of TOG2 (denoted Stu2(TOG2-TOG2)) yielded a polymerase that is only slightly weaker than wild-type (5.1-fold maximal stimulation for TOG2-TOG2 compared to 6.1-fold for wild-type) (Figure 3.1E,F, see also Figure 3.1—figure supplement 1; Figure 3.1—figure supplement 1—source data 1). Substituting TOG2 with a second copy of TOG1 (denoted Stu2(TOG1-TOG1)) also yielded an active polymerase, although less so than for TOG2-TOG2 (Figure 3.1E,F). The 'transplanted' TOG1 domain contained ~25 residues outside the core TOG1 domain (see Materials and methods); this extra difference may account for the lower activity of TOG1-TOG1 compared to TOG2-TOG2, and will be discussed in the next section. In summary, different kinds of tubulin-binding TOG domains are not required to support activity, and reducing the number of 'active' TOGs from 4 to 2 reduced polymerase activity approximately 2-fold without weakening end-association.

While these dimeric Stu2 variants with TOG1 or TOG2 inactivated displayed modest decreases in activity but normal end-binding affinity, a monomeric Stu2 variant (Stu2-Δcc, truncated before the coiled-coil segment that mediates dimerization) behaved differently. Stu2-Δcc displayed a substantial decrease in activity as well as greatly reduced end-binding affinity compared to dimeric variants (Figure 3.1D,F). Why did dimeric polymerases operating with two

active TOGs (Stu2(TOG1*-TOG2) or Stu2(TOG1-TOG2*)) show robust activity whereas the monomeric Stu2-Δcc polymerase, which also has two active TOG domains, did not? We speculated that reduced basic charge might account for the poor activity of the monomeric variant. Indeed, Stu2-Δcc only has a single basic region but dimeric variants have two (one from each monomer). We therefore measured the activity of Stu2-Δcc-2xBasic, wherein the unstructured basic region was mutated to have twice the normal positive charge, equivalent to what would be found in a dimer. 'Supercharging' the basic region restored high-affinity end-binding (Figure 3.1D,F). The supercharged monomeric polymerase also showed maximal fold-stimulation of elongation rates comparable to the dimeric Stu2(TOG1*-TOG2) or Stu2 (TOG1-TOG2*) polymerases that also operate with only two active TOGs (Figure 3.1D).

The experiments described in this section demonstrate that the polymerase activity of Stu2: (i) does not strictly require different kinds of TOG, (ii) is approximately proportional to the number of tubulin-binding TOG domains (when positioned as in wild-type), and (iii) is modulated by the 'strength' of the basic region (Figure 3.1G). The observation that monomeric and dimeric 'two TOG' polymerases show comparable activity as long as their respective basic regions have similar charge indicates that how the active TOGs are linked is of little importance for polymerase activity. Indeed, in Stu2(TOG1-TOG2*) the active TOG1s are linked via the coiled-coil by the natural linker, the 'dead' TOG2 domains, and the basic regions (see TOG1-TOG2* cartoon in Figure 3.1C). Such loose requirements on the elements linking the TOGs suggests that dimeric polymerases like Stu2/Alp14 and monomeric polymerases like XMAP215/chTOG share a common mechanism despite having different oligomerization states. These findings are broadly consistent with the tethering model we proposed previously (Ayaz et al., 2014).

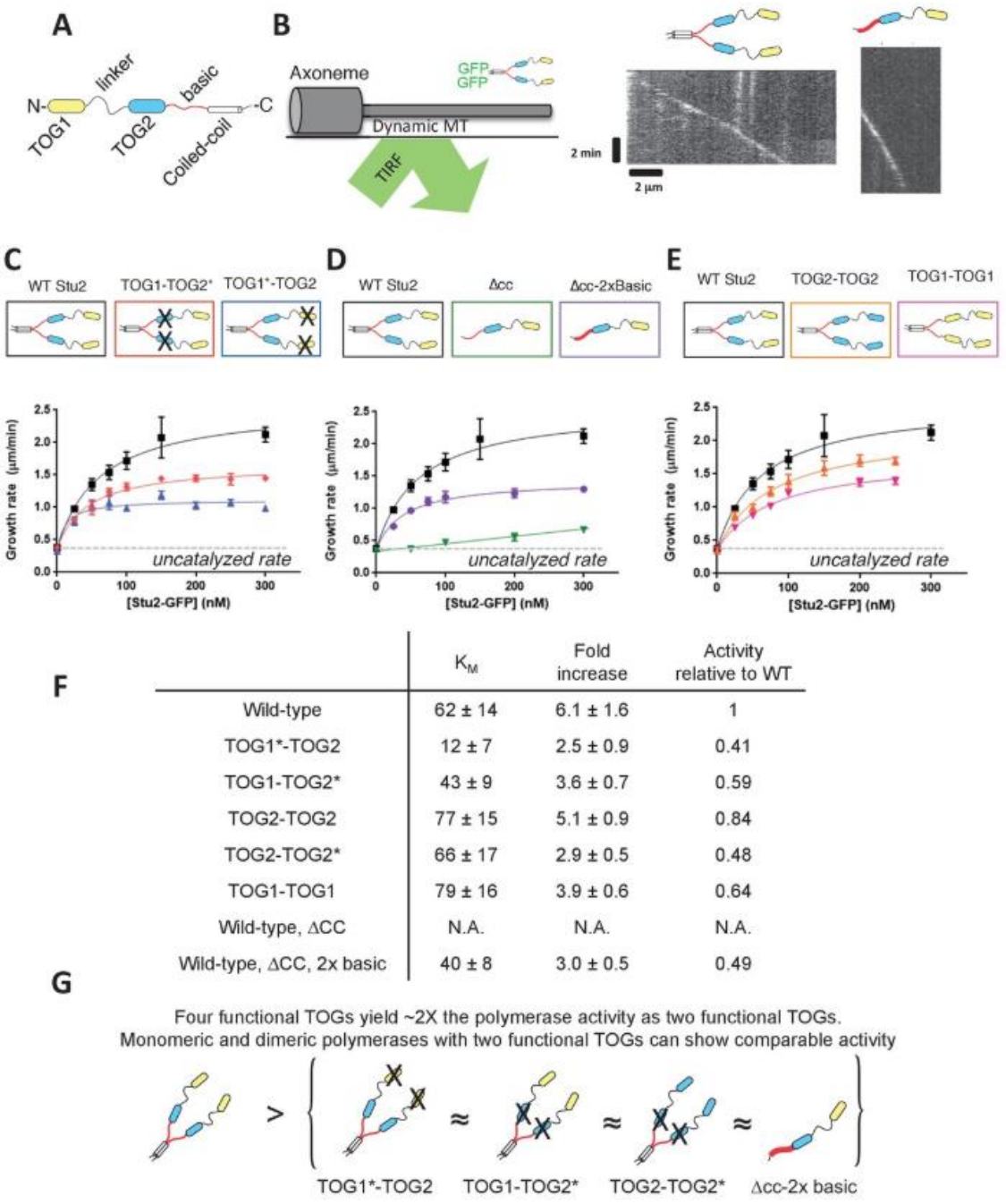

F

	K_M	Fold increase	Activity relative to WT
Wild-type	62 ± 14	6.1 ± 1.6	1
TOG1*-TOG2	12 ± 7	2.5 ± 0.9	0.41
TOG1-TOG2*	43 ± 9	3.6 ± 0.7	0.59
TOG2-TOG2	77 ± 15	5.1 ± 0.9	0.84
TOG2-TOG2*	66 ± 17	2.9 ± 0.5	0.48
TOG1-TOG1	79 ± 16	3.9 ± 0.6	0.64
Wild-type, ΔCC	N.A.	N.A.	N.A.
Wild-type, ΔCC, 2x basic	40 ± 8	3.0 ± 0.5	0.49

G

Figure 3.1. Polymerase activity requires at least two TOGs that need not be different, and a basic region; dimerization is not essential. (A) Domain organization of Stu2, from N- to C-terminus. (B) All-yeast *in vitro* reconstitution assay. (left) Schematic of the TIRF assay. Axonemes seed unlabeled yeast microtubules in the presence of Stu2-eGFP. (right) Representative kymographs for wild-type Stu2 and for a monomeric Stu2 variant. Microtubule growth rates are determined by tracking the Stu2-eGFP spot on the microtubule end. (C) Inactivating TOG1 (blue box/points, TOG1* indicates the R200A mutation) or TOG2 (red box/points, TOG2* indicates the R519A mutation) weakens the polymerase activity of the dimer compared to the wild-type dimer (black).

Smooth curves indicate a hyperbolic fit to the data. Black: each point represents n = 45 microtubules measured from three different chambers; red/blue: n = 20 microtubules. Error bars are SEM. (D) Eliminating dimerization reduces polymerase activity by sharply weakening end binding affinity (green). End-binding affinity is restored by increasing the charge in the basic domain (purple). Data were fit as in C., and the WT data are repeated from that panel. Green: n = 45 microtubules measured from three different chambers; purple: n = 25 microtubules. Error bars are SEM. (E) Functional Stu2 variants containing only TOG2 (TOG2-TOG2, orange) or only TOG1 (TOG1-TOG1, pink). Smooth curves indicate a hyperbolic fit to the data. Data were fit as in C., and the WT data are repeated from that panel. Orange: n = 30 microtubules measured from two different chambers; pink: n = 20 microtubules measured. Error bars are SEM. See also Figure 3.1—figure supplement 1. (F) Summary statistics from the hyperbolic fits shown in C, D and E. See also Figure 3.1—figure supplement 1. The maximal activity decreases when the number of TOGs is reduced. Apparent end binding affinity (KM) does not depend strongly on the number of type of active TOGs. (G) Cartoon illustrating that polymerases with two tubulin-binding TOGs are about half as active as WT with its four TOGs.

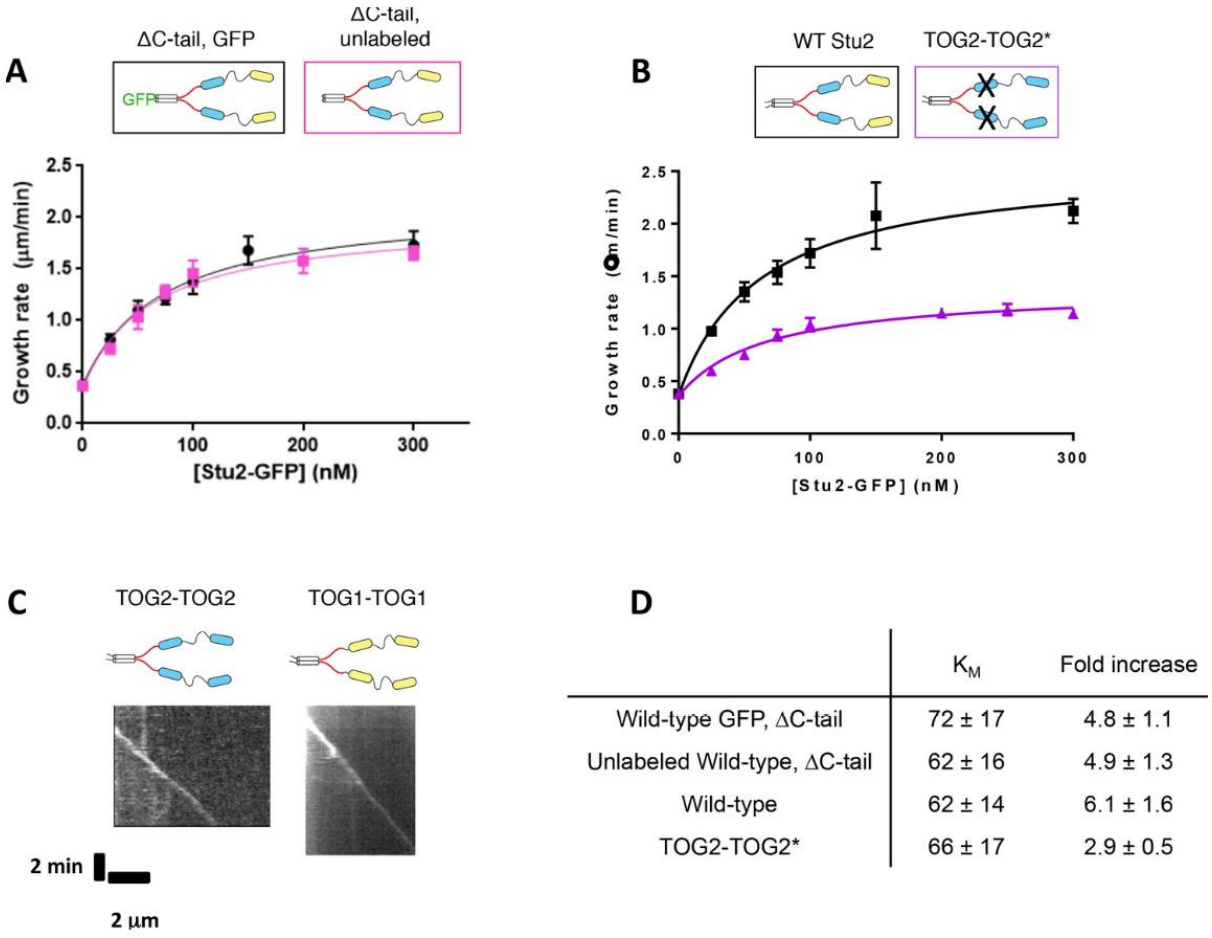

	K_M	Fold increase
Wild-type GFP, ΔC-tail	72 ± 17	4.8 ± 1.1
Unlabeled Wild-type, ΔC-tail	62 ± 16	4.9 ± 1.3
Wild-type	62 ± 14	6.1 ± 1.6
TOG2-TOG2*	66 ± 17	2.9 ± 0.5

Figure 3.1-figure supplement 1: Additional data supporting the activity of various Stu2 constructs. (**A**) A Stu2-eGFP variant lacking the C-terminal tail (ΔC-tail) exhibits similar polymerase activity with (black) or without (pink) a C-terminal eGFP tag. Smooth curves indicate a hyperbolic fit to the data. Black: N = 45 measured from three different chambers, pink: N = 25. Error bars show SEM. (**B**) Mutating the basic-proximal TOG2 in an all TOG2 polymerase (TOG2-TOG2*, purple) results in a slight decrease in polymerase activity. Black: N = 45 measured from three different chambers; purple: N = 20 measurements. Error bars show SEM. Smooth curves indicate a hyperbolic fit to the data. (**C**) Both TOG2-TOG2 polymerases (kymograph, left) and TOG1-TOG1 polymerases (kymograph, right) can tip-track growing microtubule ends. Representative kymographs for each sample contain 100 nM Stu2 mutant and 800 nM wild-type yeast tubulin. (**D**) Summary statistics of hyperbolic fits to the activity measurements shown in A and B.

The TOG domain adjacent to the Stu2 basic region controls end localization

Based on the similarity of their structural and biochemical interactions with tubulin, we argued previously that TOG1 and TOG2 were likely to be interchangeable in the polymerase mechanism (Ayaz et al., 2014). Here, we observed roughly comparable activity for Stu2(TOG1-TOG2*) and Stu2 (TOG1*-TOG2). To better understand how inactivating TOG1 or TOG2 affects the activity of a polymerase, we sought to measure the specific activity – measured activity normalized to the number of polymerases at the microtubule end – of these variants. Such measurements require quantification of the amount of wild-type or variant Stu2 on the microtubule end.

We first measured fluorescence intensity as a function of concentration for the wild-type Stu2- eGFP spot on the microtubule end, using the same TIRF assay (Figure 3.2A). The intensities showed saturation behavior with increasing concentration (Figure 3.2A). A hyperbolic fit to the concentration dependent fluorescence yielded a concentration at half-maximal intensity of 20 nM. The concentration-dependence of end-binding for Stu2 is comparable to the concentration-dependence we observed for activity (60 nM, see Figure 3.1F). If we assume (supported by photobleaching analysis, see next section) that the intensity measurements at 5 nM Stu2 reflect individual Stu2 dimers on the microtubule end, then the saturating fluorescence corresponds to ~6 Stu2 dimers on the microtubule end. Thus, the microtubule end can support approximately one Stu2 dimer for every two protofilaments.

Unexpectedly, Stu2(TOG1*-TOG2) and Stu2(TOG1-TOG2*) variants accumulated to different extents on the microtubule end. Whereas Stu2(TOG1*-TOG2) was present in amounts comparable to wild-type, Stu2(TOG1-TOG2*) only reached about half that level (Figure 3.2B; Figure 3.2—source data 1). These differences could reflect the identity of the active TOG, the

position of the active TOG in the primary sequence, or both. Stu2(TOG2-TOG2*) (wherein the natural TOG1 domain was replaced with a TOG2) accumulated to comparable levels as TOG1-TOG2* (Figure 3.2B). Thus, installing a TOG2 domain in the N-terminal position where TOG1 normally resides did not compensate for the inactivation of TOG2 in its natural position. This provides clear evidence that a positional effect – for example proximity to the basic region - contributes to specify the degree of end accumulation. The differential accumulations at the microtubule end means that there are more substantial differences in specific activity than were apparent from our measurements of 'bulk' polymerase activity. Indeed, after normalizing by the different saturating amounts of polymerase on the microtubule end, Stu2(TOG1-TOG2*) shows 20% higher specific activity than wild-type Stu2 (Figure 3.2C), despite having half as many active (non-mutated) TOGs. On a per-active-TOG basis, the specific activity of Stu2(TOG1-TOG2*) is over two-fold higher than wild-type (Figure 3.2C).

Why does inactivating TOG2 for tubulin-binding lead to an increase in specific activity? We speculated that a region of TOG2 outside the conserved tubulin-binding interface might be required for plus-end recognition/localization, and that tubulin binding to TOG2 might antagonize this role. If true, then deleting TOG2 should yield different and stronger effects than mutating TOG2. We therefore prepared Stu2 variants in which the basic-proximal TOG2 domain was deleted (e.g. Stu2(TOG1- ΔTOG2)). Control experiments demonstrated that deleting TOG2 did not compromise the ability of TOG1 to bind curved tubulin, or of the basic region to bind the lattice (Figure 3.2—figure supplement 1B; Figure 3.2—figure supplement 1—source data 1). However, deleting the TOG2 domain completely abolished polymerase activity and end association/tracking (Figure 3.2D, Figure 3.2—figure supplement 1A). This dramatic loss of function could not be rescued by installing a TOG2 domain in place of TOG1 (Figure 3.2D), so

the lack of activity must reflect the positioning of the active TOG domain relative to the basic region, not the nature of the active TOG. To more directly test the idea that proximity to the basic domain impacts polymerase activity, we purified a Stu2 mutant that contains a flexible spacer (16 aa, GSSGGSSSGSSGGGSG) between the end of TOG2 (residue 560) and the start of the basic domain (residue 561)(Figure 3.2—figure supplement 1D). The spacer-containing polymerase retained the ability to tip-track and stimulate elongation, but it was substantially less active than wild-type (Figure 3.2—figure supplement 1D,E). These data, together with the data from Stu2(TOG1-TOG1) that also introduced extra sequence between the basic region and the preceding TOG (Figure 3.1E), indicate that proximity of a TOG domain to the basic region is important.

A genetic rescue assay provides additional support for the special nature of the basic-proximal TOG2 domain: deleting TOG2 compromised rescue most severely whereas mutating TOG2, or deleting or mutating TOG1 domain, affected rescue less severely (and comparably to each other) (Figure 3.2E). Stu2 function does not appear to have an absolute requirement for a TOG2 domain next to the basic region, because Stu2(TOG1-TOG1), a construct entirely lacking TOG2 domains, showed appreciable rescue activity (Figure 3.2—figure supplement 1C; slightly different domain boundaries for the transplanted TOG1 were used in the rescue constructs compared to the *in vitro* experiments described above, see Materials and methods). As in the *in vitro* assays (Figure 3.1E), in the rescue assay Stu2(TOG1-TOG1) was less active than Stu2(TOG2-TOG2). We conclude that there is a special requirement for a basic-proximal TOG domain, and that there might be some separation of function between TOG1 and TOG2 at this position.

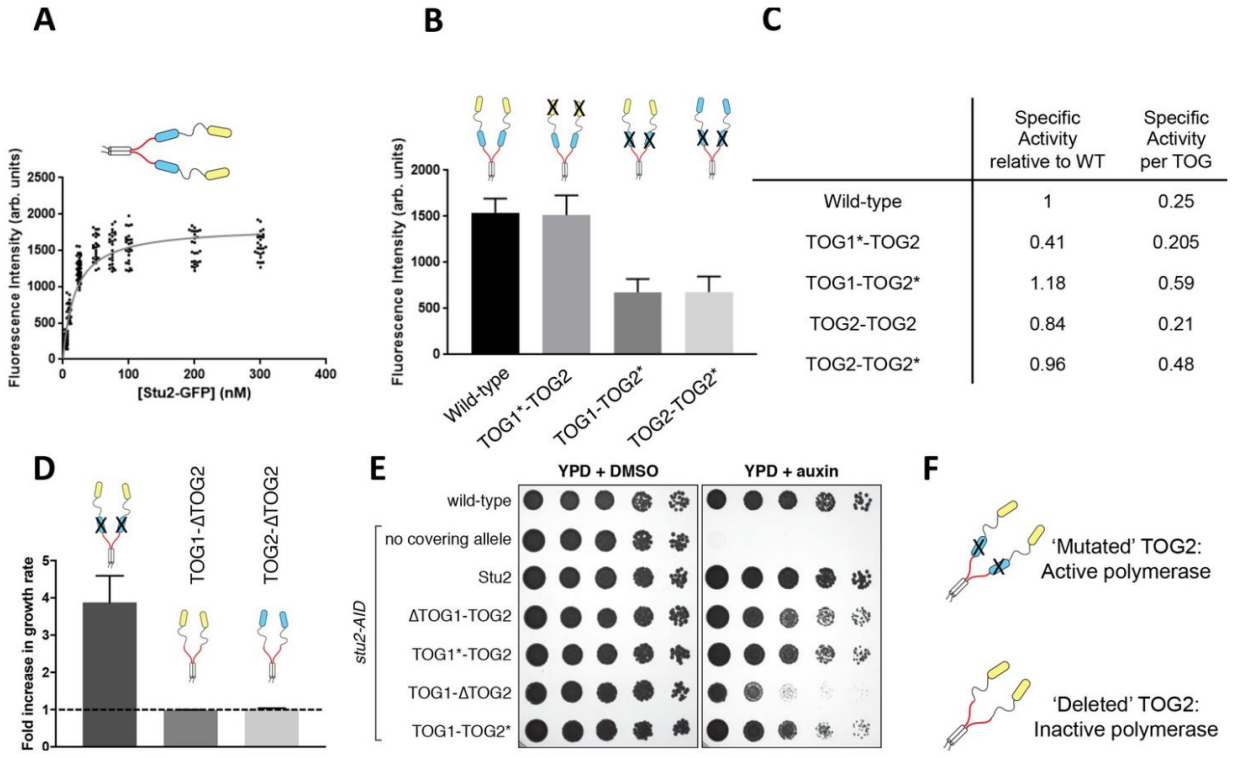

Figure 3.2. A unique functional role for the basic-proximal TOG domain. (A) Fluorescence intensity of wild-type Stu2-eGFP dimers on the microtubule end. Intensities were determined as a function of Stu2 concentration by measuring the fluorescent 'spot' at the end of a growing microtubule. The data were fit with a hyperbolic function, yielding a half-maximal concentration of 19 nM, comparable to the half-maximal concentration for activity of 62 nM. N = 200 measured from two different chambers for 5 nM, N = 25 for 10, 50–300 nM, N = 50 measured from two different chambers for 25 nM (B) Interfering with tubulin binding by the basic-proximal TOG (TOG2*; R519A mutation) decreases the amount of Stu2 on the microtubule end, but interfering with tubulin binding by the N-terminal TOG (TOG1*; R200A mutation) does not detectably change the amount of Stu2 on the end. The reduced accumulation of TOG1-TOG2* cannot be ascribed to the loss of tubulin binding by TOG2, because TOG2-TOG2* also shows reduced accumulation of the microtubule end. Samples were analyzed with 200 nM Stu2 in the presence of 0.8 µM tubulin in dynamic assays. N = 50 for all. Error bars are SEM. (C) Specific activity of Stu2 variants relative to wild-type, on a per-polymerase (left) and per functional TOG (right) basis. Specific activity was obtained by dividing the values from the last column of Figure 3.1F by the relative amount of polymerase on the microtubule end (as determined in Figure 3.2B; one for WT and Stu2(TOG2-TOG2), 0.5 for Stu2(TOG1-TOG2*) and Stu2(TOG2-TOG2*)). Stu2 variants with the basic-proximal TOG inactivated show higher specificity. (D) Deleting the basic-proximal TOG domain (ΔTOG2) abolishes polymerase activity and interaction with the microtubule lattice (see Figure 3.2—figure supplement 1), whether the N-terminal TOG domain is TOG1 or TOG2. Changes in polymerase activity may be attributable to the distance between the most basic-proximal TOG and the basic domain (see Figure 3.2—figure supplement 1D) The fold-increase in elongation rate is plotted for different polymerase variants. The dashed line indicates the rate of elongation for the 'no Stu2' control. N = 25 measurements for all; error bars

are SEM. Samples contained 0.8 µM tubulin and 200 nM Stu2 variants. (E) Wild-type (SBY3), stu2-AID (SBY13772) and stu2-AID cells expressing various STU2-3V5 alleles from an ectopic locus (wildtype, SBY13901; TOG1D, SBY13904; R200A, SBY13919; TOG2D, SBY13907; R519A, SBY13925) were serially diluted (5-fold) and spotted on plates containing either DMSO or 500 mM auxin. Stu2 constructs deleted for TOG1 (ΔTOG1-TOG2) or with TOG1 inactivated for tubulin binding (TOG1*-TOG2) display a mild defect in rescuing the loss of WT Stu2. A Stu2 construct deleted for TOG2 (TOG1-ΔTOG2) shows a more severe loss of rescue activity. A Stu2 construct with TOG2 inactivated for tubulin binding (TOG1- TOG2*) yields full rescue activity. See also Figure 3.2—figure supplement 1. (F) Schematic cartoon summarizing that polymerase activity and Stu2 function requires a TOG domain adjacent to the basic region, even if that TOG is compromised for binding to unpolymerized tubulin.

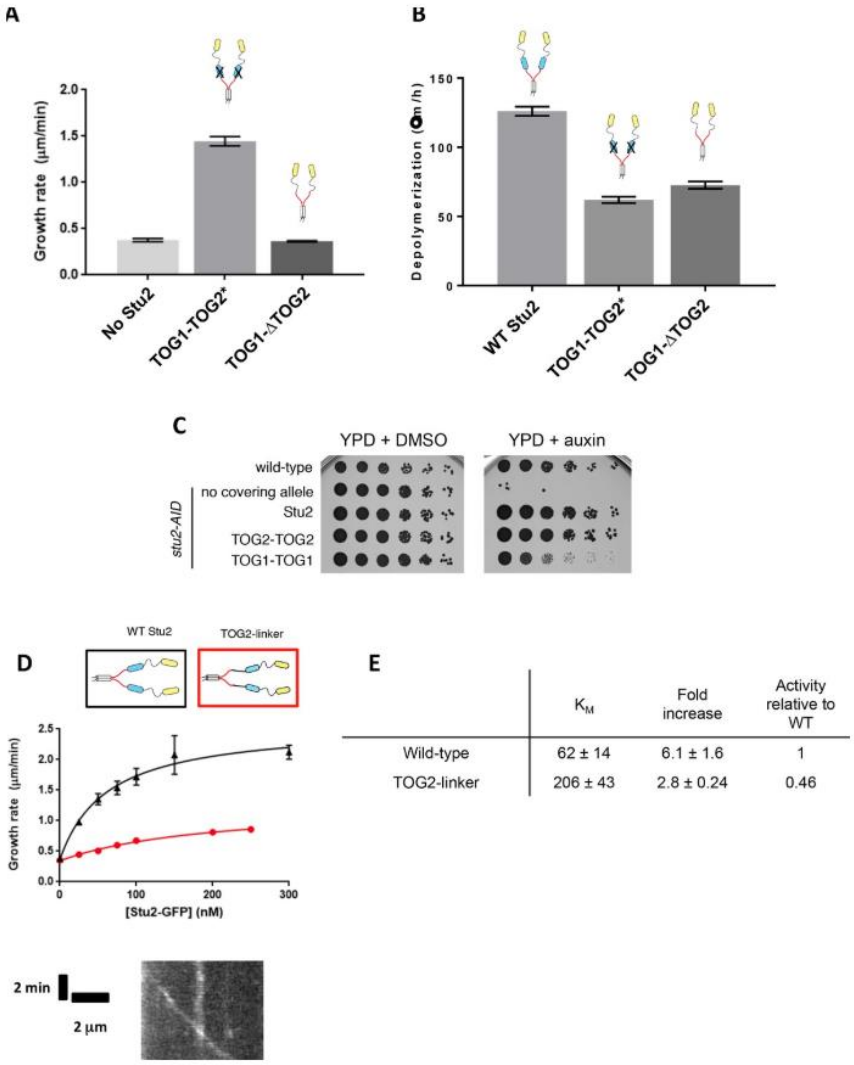

Figure 3.2-figure supplement 1: Effects of inactivating, deleting, or replacing the basic-proximal TOG domain.

(**A**) Deleting the TOG2 domain (Stu2(TOG1-ΔTOG2)) abolishes polymerase activity. Polymerase activity is retained when the TOG2 domain is inactivated by mutagenesis. Samples were analyzed with 200 nM Stu2 in the presence of 0.8 µM tubulin in dynamic assays. N = 25 end measurements for all; error bars are SEM. (**B**) Deleting the TOG2 domain (Stu2(TOG1-ΔTOG2)) does not compromise the tubulin binding activity of TOG1 as judged in a 'depolymerase' assay wherein TOG domains cause the depolymerization of stable microtubules. Samples were analyzed with 200 nM Stu2 in the presence unlabeled GTPγS stabilized MTs. N = 20 measurements for all. Error bars show SEM. (**C**) Wild-type (SBY3), *stu2-AID* (SBY13772) and *stu2-AID* cells expressing various *STU2-3V5* alleles from an ectopic locus (wildtype, SBY13901; TOG1Δ, SBY13904; TOG2-TOG2, SBY16931; TOG1-TOG1, SBY17595) were serially diluted (5-fold) and spotted on plates containing either DMSO or 500 µM auxin. A Stu2 variant in which TOG2 is replaced with a second copy of TOG1 (Stu2(TOG1-TOG1)) partially rescues the loss of endogenous Stu2 in a genetic rescue assay, but to a lesser

degree than that of a Stu2(TOG2-TOG2) variant. (**D**) Inserting a flexible, 16 amino acid spacing linker between the end of TOG2 and the basic domain weakens the polymerase activity of Stu2 bud does not abolish end localization, shown in the representative kymograph (bottom). Black: N = 45 measured from three different chambers; red: N = 20 measurements. Error bars show SEM. Smooth curves indicate a hyperbolic fit to the data. (**E**) Summary statistics of hyperbolic fits to the activity measurements shown in D.

Processivity and the amount of end resident polymerase together determine maximal achievable activity

The mechanisms of processivity in Stu2/XMAP215 family polymerases are not well understood. We wondered if differences in processivity might explain why Stu2(TOG2-TOG2*) and Stu2(TOG1*- TOG2) differ more than 2-fold in specific activity, despite both using TOG2 as their only tubulin-binding TOG. The hyperbolic fit to the fluorescence intensity of Stu2 on the microtubule end indicates that when the concentration of Stu2 is 5 nM (1/4 of the apparent dissociation constant for tip binding, see Figure 3.2A), there should be on average 1.2 Stu2 dimers on the microtubule end. This suggested that 5 nM Stu2 would be a reasonable concentration for performing single-molecule measurements of Stu2 on the microtubule end. We confirmed using photobleaching analysis that the Stu2 'spots' on dynamic microtubules had intensity comparable to individual Stu2 dimers that bleached in two steps (Figure 3.3A). At this low concentration we observed short 'tracks' of Stu2 fluorescence, with gaps of variable length in between (Figure 3.3B). We fit a one-phase exponential decay to the histogram of end residence times, which yielded a characteristic residence time of 2.2 s (Figure 3.3B, black, 3.3D; Figure 3.3—source data 1). At the low concentration of 5 nM, Stu2 is not meaningfully affecting microtubule growth rates. We performed 'spike' experiments (5 nM Stu2- GFP + 195 nM unlabeled Stu2) to monitor the behavior of individual Stu2 polymerases under conditions where Stu2 was substantially increasing growth rates. We observed short fluorescent Stu2 'tracks' in these 'spike' experiments, and the distribution of dwell times yielded a characteristic residence time of 1.98 s (Figure 3.3B, orange, 3.3D). The characteristic residence times for Stu2 at high and low concentrations are quite similar, and are also the same order of magnitude as that measured for XMAP215 (3.8 s). 200 nM Stu2 increases the microtubule elongation rate ~1.8

mm/min over the control (equivalent to 49 tubulins per second), and at this concentration we estimate that there are ~6 Stu2 polymerases on the end. If 6 Stu2s on average account for ~98 tubulins in 2 s (the measured residence time), then each Stu2 adds ~16 tubulins. Thus, like XMAP215, Stu2 is a modestly processive polymerase.

To determine if inactivating TOG1 or TOG2 for tubulin-binding affected end residence, we repeated the same assay using 5 nM of Stu2(TOG1*-TOG2) or Stu2(TOG1-TOG2*). Inactivating the TOG1 domain yielded a modest decrease in dwell times (1.7 s for Stu2(TOG1*-TOG2) compared to 2.2 s for wild-type) (Figure 3.3C,D). In contrast, inactivating the TOG2 domain almost doubled the polymerase dwell time (to 4.0 s for Stu2(TOG1-TOG2*)) (Figure 3.3C,D). This enhanced end residence of Stu2(TOG1-TOG2*) could not be ascribed to some TOG1-specific property, because Stu2(TOG2- TOG2*) also showed a nearly two-fold increase in end-residence time (3.9 s for Stu2(TOG2-TOG2*) compared to 2.2 s for wild-type) (Figure 3.3C,D). Thus, inactivating tubulin binding by the basic-proximal TOG domain actually increases dwell time (and presumably processivity); deleting the TOG2 domain (Stu2(TOG1-ΔTOG2)) abolished end tracking entirely. This counterintuitive behavior is consistent with the idea that TOG2:tubulin engagement antagonizes some other, end-specific function of TOG2; it probably also accounts for the differences in specific activity we measured.

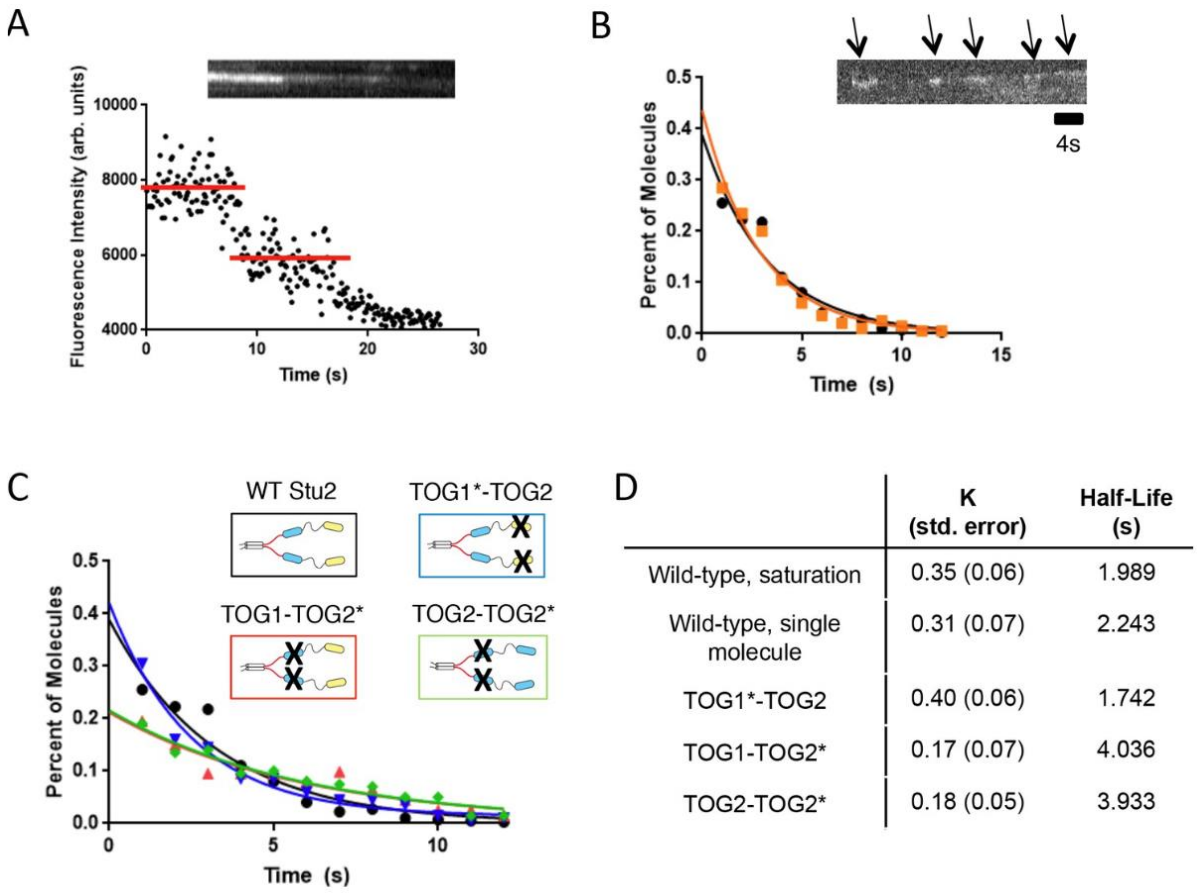

	K (std. error)	Half-Life (s)
Wild-type, saturation	0.35 (0.06)	1.989
Wild-type, single molecule	0.31 (0.07)	2.243
TOG1*-TOG2	0.40 (0.06)	1.742
TOG1-TOG2*	0.17 (0.07)	4.036
TOG2-TOG2*	0.18 (0.05)	3.933

Figure 3.3. Inactivating tubulin binding by the basic-proximal TOG domain enhances processivity of Stu2. (A) Example raw fluorescence intensity trace showing two-step photobleaching of a stationary, homodimeric Stu2-eGFP. (B) Lifetime distribution for single Stu2-eGFP molecules on the growing microtubule end under single molecule conditions (5 nM Stu2, black) or 'spiked' into a higher concentration reaction (200 nM Stu2 of which only 5 nM is labeled, orange). Inset kymograph illustrates instances of Stu2 'runs' (arrows). Histogram summarizes n = 400 measurements (four independent trials at 1 µM tubulin) for 5 nM Stu2-eGFP and n = 200 measurements (two independent trials at 0.8 µM tubulin) made using 5 nM Stu2-eGFP with 195 nM Stu2- KCK unlabeled. Data, which are plotted as percent of total for comparative purposes, were fit with an exponential, yielding an average residence time of 2.2 s (see also D) for single molecule eGFP and 2.0 s (see also D) for the spike measurements. Scale bar is 4 s. (C) Lifetime histograms for Stu2 variants. Compromising tubulin binding by the basic-proximal TOG (TOG1-TOG2*, red trace) yields a roughly 2-fold increase in end residence time. Compromising the N-terminal TOG (TOG1*-TOG2, blue trace) does not increase end-residence time. TOG2-TOG2* (green trace) also shows an increase in end residence time. All samples contained 5 nM Stu2-eGFP variants and 1 µM unlabeled yeast tubulin. Two independent trials of n = 100 measurements for all mutants, yielding a total n = 200. Samples were fit with exponential as done in B to extract average residence times. (D) Tabulated summary of results from all exponential fits to residence time distributions in C.

The strength of interactions between the basic domain and the MT lattice depend on whether TOGs are engaged with αβ-tubulin

Current models for XMAP215/Stu2 family polymerases assume that lattice binding by the basic domain is independent of tubulin binding by the TOGs (e.g [Ayaz et al., 2014; Widlund et al., 2011]). However, our data demonstrating a need for a TOG domain proximal to the basic region raise the possibility that TOG:tubulin binding may influence basic:lattice interactions, thereby suggesting that TOG:tubulin and basic:lattice interactions may not be independent after all. To begin investigating if basic:lattice interactions are influenced by TOG:tubulin engagement, we prepared a 'doubly dead' Stu2 variant (denoted Stu2(TOG1*-TOG2*)) in which both TOGs were inactivated for tubulin binding. As expected, the doubly dead variant failed to stimulate growth rate (Figure 3.4—figure supplement 1; Figure 3.4—figure supplement 1—source data 1). Unexpectedly, the doubly dead variant robustly coated the lattice, without detectable end preference (Figure 3.4). These results indicate that interactions between TOGs and unpolymerized tubulin attenuate lattice binding by the basic region of Stu2.

Does tubulin-induced attenuation of lattice binding require that all four TOGs engage with tubulin? Dimeric polymerases with TOG1 or TOG2 inactivated (Stu2(TOG1*-TOG2) or Stu2(TOG1- TOG2*)) showed robust tip localization with little binding to the bulk lattice (Figure 3.4). The monomeric Stu2-Δcc-2xBasic behaved similarly. However, when one of the two TOGs in this monomeric construct was mutated (e.g. Stu2(TOG1*-TOG2)Δcc-2xBasic), we observed strong binding to the lattice without detectable tip preference (Figure 3.4); polymerase activity was also lost (Figure 3.4— figure supplement 1). Thus, at least two TOG:tubulin interactions are required to attenuate the lattice binding activity of Stu2.

We next tested a panel of tubulin mutants (Figure 3.5A) to define the tubulin elements required for attenuating lattice-binding by the basic region. We were particularly interested in mutations on tubulin:tubulin interfaces. Such mutants often do not polymerize efficiently (e.g. [Johnson et al., 2011] and Figure 3.5—figure supplement 1A), which means we could not apply the 'dynamics' assay we had been using. Consequently, for these assays with tubulin mutants we used GTPγS-stabilized wild-type microtubules as the 'substrate' for lattice binding. Control experiments recapitulated the effects we observed on dynamic microtubules: Stu2 coated the lattice of stabilized microtubules when there was no unpolymerized tubulin present in the assay, and this lattice coating was lost with the addition of unpolymerized wild-type tubulin (Figure 3.5B, left).

We first speculated that the negatively charged C-terminii of TOG-bound tubulins might themselves bind to the basic region, effectively competing with the microtubule lattice for the basic region. To test this idea, we purified 'tail-less' tubulin lacking the C-terminii of α- and β-tubulin. This tail-less tubulin also inhibited Stu2 binding to the lattice (Figure 3.5B, middle panel). Thus, competing interactions between the basic region and the charged C-terminii of the TOG-bound tubulins cannot explain the tubulin-induced attenuation of lattice binding.

We next considered the possibility that interactions between the TOG-bound tubulins mediate the attenuation of lattice binding. To test if tubulin:tubulin contacts are important, we performed assays with tubulins containing mutations that block or weaken longitudinal (head-to-tail) or lateral (side-to-side) tubulin:tubulin interfaces. Gel filtration (Figure 3.5—figure supplement 1B) and analytical ultracentrifugation binding experiments both show that longitudinal (β:T175R, V179R) and lateral (β:F281A) mutants bind Stu2:TOG1 comparably to wild-type (Figure 3.5—figure supplement 1C,D). Longitudinal interactions between the TOG-

bound tubulins do not appear to be important for the tubulin-induced attenuation of lattice binding, because tubulin 'blocked' on its minus-end (T350E α-tubulin; [Johnson et al., 2011], Figure 3.5B) or on its plus-end (T175R, V179R β-tubulin; [Johnson et al., 2011], Figure 3.5—figure supplement 2) attenuated lattice binding by Stu2 comparably to wild-type tubulin. By contrast, Stu2 remained bound to the lattice in the presence of tubulin carrying mutations at the site of lateral interactions between heterodimers (Alushin et al., 2014) (H284A on α-tubulin, Figure 3.5—figure supplement 2; or F281A on β-tubulin, Figure 3.5B, left) Thus, lateral contacts between TOG-bound tubulins are important for the tubulin-induced antagonism of basic:lattice interactions.

The data described in this section reveal that for Stu2, there is antagonistic coupling between TOG:tubulin and basic:lattice interactions: when at least two TOGs on a given polymerase each engage a tubulin, lateral interactions (possibly transient) between those TOG-bound tubulins substantially reduce lattice-binding affinity (Figure 3.5C). We wondered if this antagonism between TOG: tubulin association and lattice binding might represent a more general property of the polymerase family? We obtained mCherry-tagged Zyg-9, the XMAP215/Stu2 family member from C. elegans (Matthews, Carter, Thierry-Mieg, & Kemphues, 1998; Srayko, Kaya, Stamford, & Hyman, 2005),to begin addressing this question. Like Stu2, Zyg-9 coated microtubules in the absence of unpolymerized tubulin, and lattice binding by Zyg-9 was greatly attenuated in the presence of unpolymerized tubulin (Figure 3.5D). Thus, it appears that reciprocal antagonism between lattice binding and TOGs engaging unpolymerized tubulin is a conserved feature of the Stu2/XMAP215 family of polymerases. This antagonism provides a new way to think about mechanisms of processivity, discussed below.

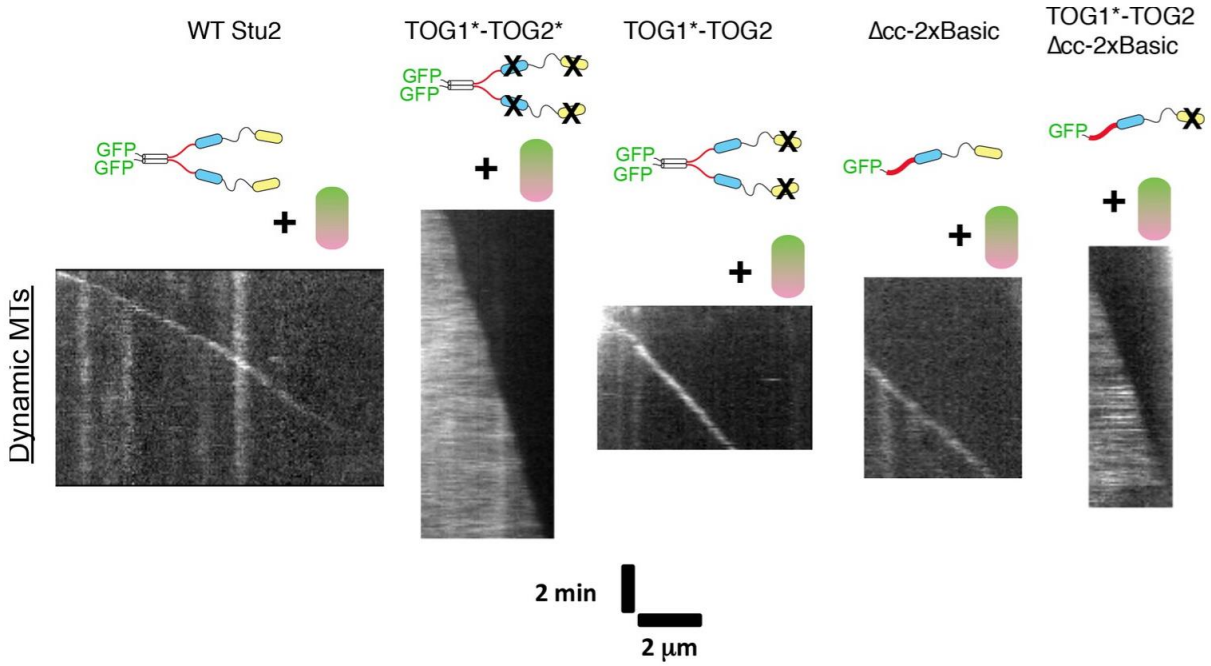

Figure 3.4: Polymerase elements required for preferential plus-end localization of Stu2. Polymerase assays were carried out using wild-type tubulin (0.8 μM) and a panel of polymerase mutants (200 nM each). Representative kymographs are shown for Stu2 variants. Plus-end localization requires at least two tubulin-binding TOGs (WT, TOG1*-TOG2, Δcc-2xBasic) and is not sensitive to how they are linked (compare TOG1*-TOG2 to Δcc-2xBasic). Unexpectedly, polymerases with 0 (TOG1*-TOG2*) or one active TOGs (TOG1*-TOG2-Δcc-2xBasic) robustly coat the body of the microtubule. See also Figure 3.4—figure supplement 1.

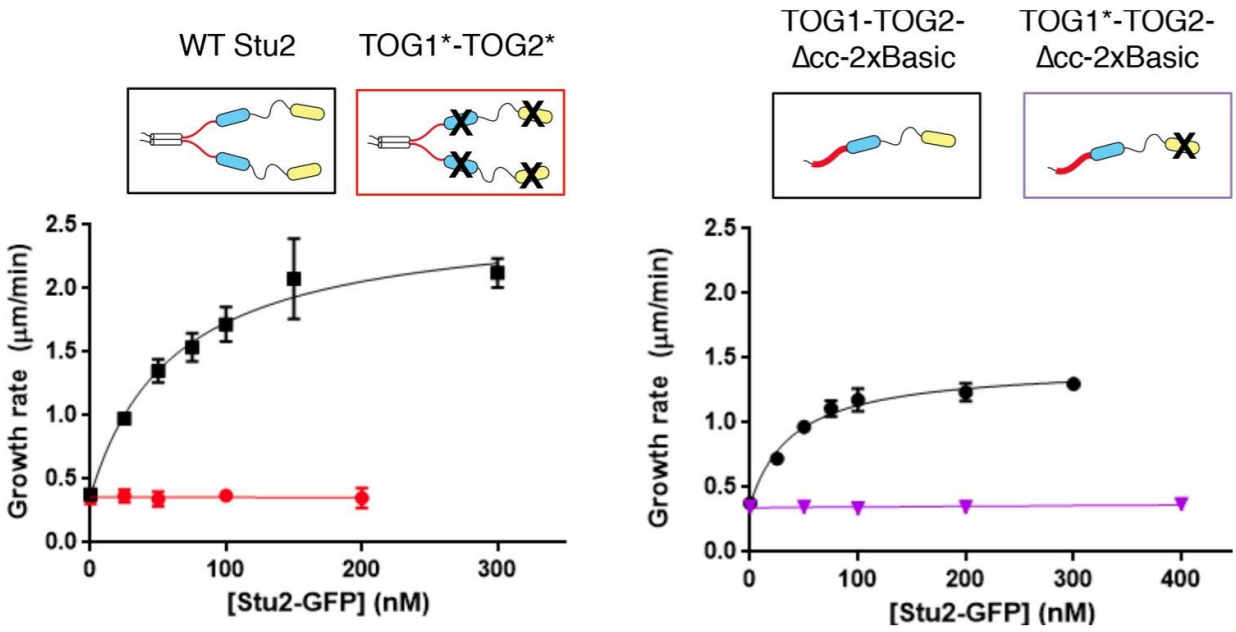

Figure 3.4-figure supplement 1: Additional data from assays using mutated TOGs. 'Double dead' Stu2 (TOG1*-TOG2*) (left) with both TOGs inactivated does not show polymerase activity (red). Data for wild-type Stu2 (black) are reproduced from Figure 3.1. Stu2(TOG1*-TOG2)-Δcc-2xBasic (right), which contains a single active TOG domain, does not show polymerase activity (purple). Data for Stu2(TOG1*-TOG2)-Δcc-2xBasic (black; this construct has two active TOGs) are reproduced from Figure 3.1. Black: N = 45 from three independent chambers; Red and Purple: N = 20 measurements. All error bars are SEM. Smooth curves indicate a hyperbolic fit to the data.

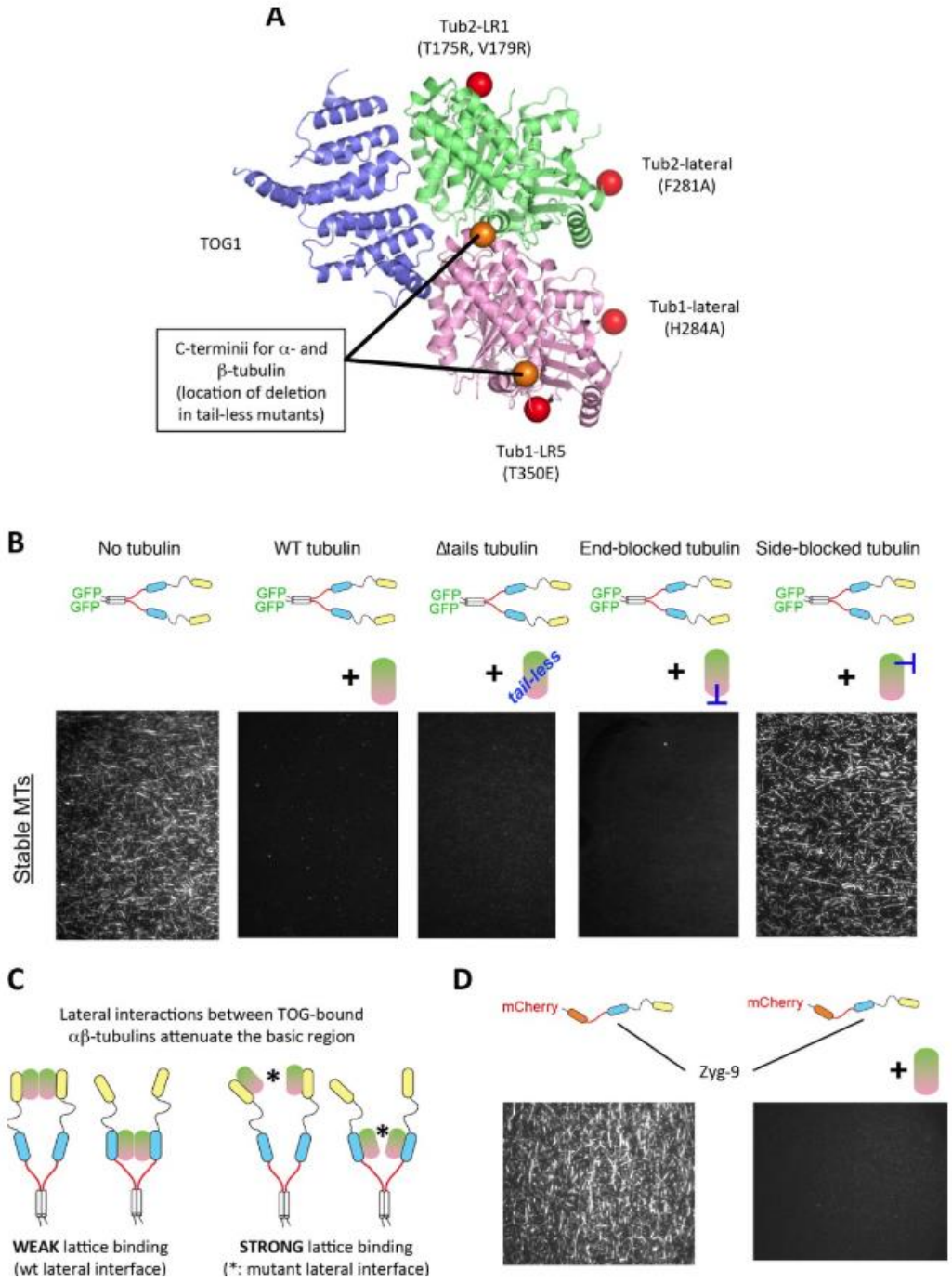

Figure 3.5. Unexpected antagonism between TOG: αβ-tubulin engagement and basic:lattice interactions. (A) The structure of Stu2:TOG1 (slate) bound to yeast αβ-tubulin (α-tubulin in pink and β-tubulin in lime; PDB code 4FFB) is shown in cartoon representation. Red spheres indicate the approximate position of interface blocking mutations on the plus- (β:T175R,V179R) or minus-end (α:T350E) and of perturbing mutations on lateral interaction surfaces (α: H284A, β: F281A). All interface mutations are distant from the TOG-interacting surface. Orange spheres

indicate the positions of the structured C-terminii of α- and β-tubulin that precede the charged ‘tails’. (B) Tubulin elements required to antagonize lattice binding by Stu2. Stu2:microtubule binding assays were monitored by TIRF and performed using stabilized microtubules as the substrate, 100 nM Stu2-eGFP, and 1 μM of tubulin mutants. Stu2 coats the stabilized microtubules when no unpolymerized tubulin in present (‘No tubulin’). Lattice-binding is substantially eliminated when wild-type tubulin is included as a competing binding partner (‘WT tubulin’). This tubulin-induced antagonism of lattice binding does not require the tubulin tails (‘Δtails tubulin’) or longitudinal contacts (‘end blocked tubulin’). Tubulin perturbed on the lateral interface does not effectively antagonize lattice binding by Stu2 (‘side blocked tubulin’), indicating that lateral contacts between TOG-bound tubulins are important. See also Figure 3.5—figure supplement 2. (C) Cartoon illustrating that lateral tubulin interactions (possibly transient) between TOG-bound tubulins antagonize interactions between the basic domain and the MT lattice. Tubulins bound to either the TOG1 or TOG2 domains are illustrated; other combinations of two tubulin-binding TOGs tested yield a similar result. (D) Control of lattice binding by unpolymerized tubulin is not an idiosyncratic property of Stu2. Zyg-9, a monomeric Stu2 family polymerase from *C. elegans,* also shows this tubulin-induced attenuation of microtubule lattice binding. 50 nM Zyg-9-mCherry was used with unlabeled GTPγS-stabilized yeast microtubules; 5 μM bovine tubulin was the competing binding partner.

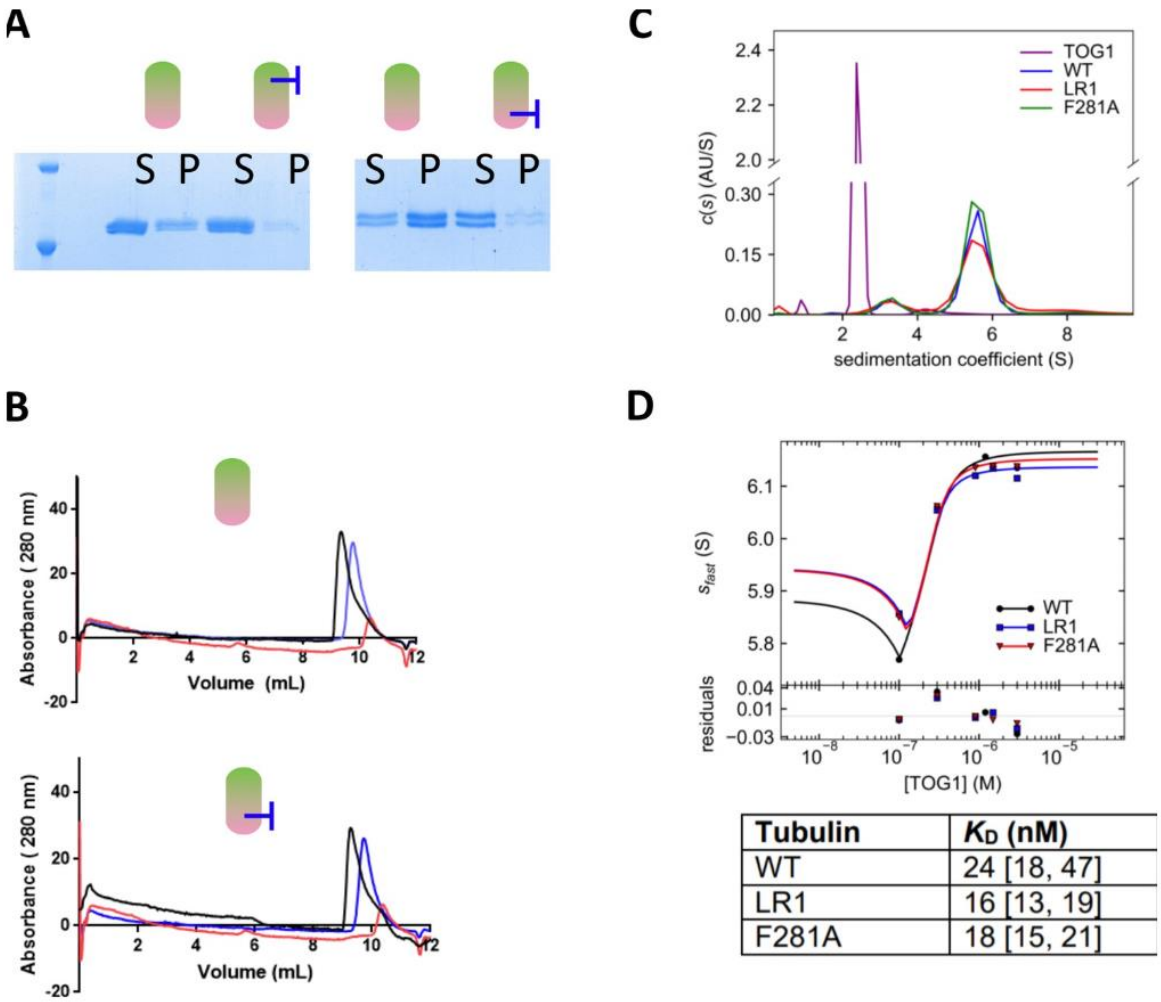

Tubulin	K_D (nM)
WT	24 [18, 47]
LR1	16 [13, 19]
F281A	18 [15, 21]

Figure 3.5-figure supplement 1: Assays characterizing the assembly and TOG-binding properties of tubulin with a mutated lateral interface. (**A**) 'Spin-down' assays for microtubule assembly reveal by SDS-PAGE that mutations on the lateral interface of β-tubulin (left, F281A) or α-tubulin (right, H284A) reduce the extent of microtubule assembly compared to wild-type. S = supernatant, p=pellet. Assays were performed using 1 μM tubulin. (**B**) A gel filtration binding assay demonstrate that a lateral tubulin mutant, Tub1-H284A, binds a TOG domain comparably to wild-type tubulin. Left: Overlaid gel filtration traces of WT tubulin alone (blue), TOG1 alone (red), and the tubulin + TOG mix (black). The shift to earlier elution volumes indicates formation of a larger complex. Right: Overlaid gel filtration traces of α-H284A tubulin alone (blue), TOG1 alone (red, repeated from left panel), and the tubulin + TOG mix (black). A similar shift in elution indicating the presence of a TOG:tubulin complex was observed. All samples contain 1 μM tubulin variant and 1 μM TOG1. (**C**) Analysis of TOG1:αβ-tubulin interactions by sedimentation velocity. The plot shows c(s) distributions (color coded by sample) for each control sample: TOG1 alone (2 μM, purple), WT tubulin (0.3 μM, blue), 'LR1' plus-end blocked tubulin (β-tubulin: T175R, V179R) (0.3 μM, red) and 'F281A' (β-tubulin: F281A) (0.3 μM, green). (**D**) Isotherms for Stu2 TOG1 domain binding to WT tubulin (black), plus-end blocked tubulin 'LR1' (β-tubulin:T175R,V179R) (blue) and side-block tubulin 'F281A' (β-

tubulin:F281A) (red). TOG1 binds with comparable affinity to all three tubulin variants including the two tubulin mutants (plus-end and side-block) and WT tubulin. Fitted binding affinities and 1 σ confidence intervals for fitted affinities (in parentheses) are shown in the table on the right.

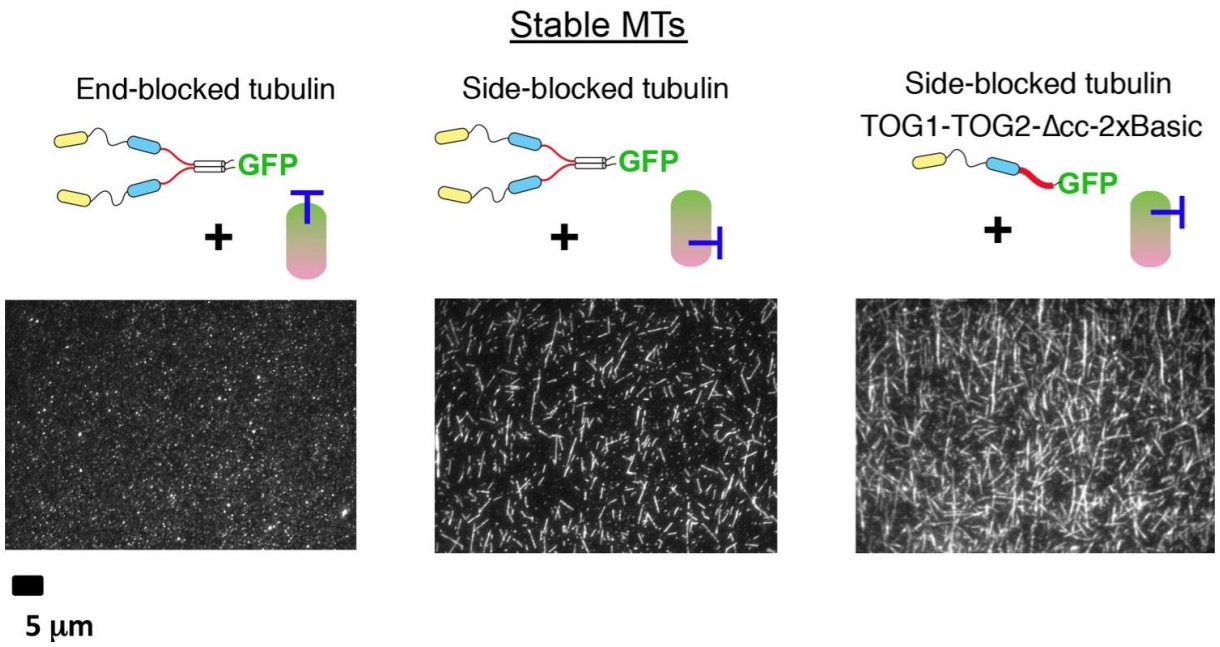

Figure 3.5-figure supplement 2: Additional data from assays using mutated tubulins. More experiments testing whether tubulin mutated on the lateral or longitudinal tubulin interfaces can antagonize interactions between the basic region and the microtubule. Results are consistent with Figure 3.5 in showing that lateral interactions between TOG-bound tubulins are important: lattice binding by Stu2 is attenuated in the presence of plus-end blocked tubulin (β-tubulin:T175R,V179R, left); lattice binding by dimeric or monomeric forms of Stu2 is not attenuated in the presence of a mutation on the lateral interface (α-tubulin:H284A, middle and right). Samples contain 100 nM Stu2-eGFP variant and 1 μM tubulin mutant; unlabeled, GTPγS-stabilized yeast microtubules were used as the MT binding substrate.

Allosteric perturbations that stabilize tubulin:tubulin associations cause futile cycling of the polymerase

Microtubule end recognition and binding to unpolymerized tubulin are mediated by preferential binding of polymerase TOG domains to the curved conformation of tubulin (Ayaz et al., 2014, 2012). However, whether the tubulin conformation cycle impacts polymerase activity in other ways has yet to be investigated. We previously characterized a tubulin 'conformation cycle' mutant, Tub2: T238A (henceforth β:T238A) (Geyer et al., 2015). This mutant retains a curved conformation in the unpolymerized state, but it stabilizes microtubules by adopting a more GTP-like conformation in the GDP lattice. These effects are reminiscent of how the small molecule taxol allosterically stabilizes microtubules (Alushin et al., 2014). Because taxol has been observed to potentiate the activity of XMAP215 (Zanic et al., 2013), we examined whether Stu2 would likewise be a more potent polymerase on β:T238A microtubules.

To our surprise, Stu2 barely stimulated elongation and showed weak to no plus-end specificity on dynamic β:T238A microtubules (Figure 3.6A,B; Figure 3.6—source data 1). Instead, Stu2 coated the lattice of these mutant microtubules, reminiscent of what we observed for the 'doubly dead' polymerase Stu2(TOG1*-TOG2*), the TOGs of which are inactivated for tubulin binding. In this case, however, the mutation in β-tubulin does not cause a defect in the interactions between individual TOGs and β:T238A tubulin: isolated TOG1 or TOG2 domains bind to wild-type and to β:T238A tubulin with comparable affinity (Geyer et al., 2015). Thus, the β:T238A mutation must antagonize the polymerase activity and preferential end binding of Stu2 through some mechanism that does not entail weakened interactions with the individual TOGs.

We had expected based on prior XMAP215/taxol experiments (Zanic et al., 2013) that Stu2 would be a better, not worse, polymerase on β:T238A microtubules. Perhaps the β:T238A

mutation in yeast tubulin does not faithfully mimic the effects of taxol binding? We addressed this possibility using Epothilone B, a natural product that affects yeast microtubule structure and stability similarly to the way taxol (which does not bind to yeast microtubules) acts on mammalian microtubules (Howes et al., 2017). Polymerase assays using wild-type yeast tubulin with a low concentration (4 mM) of Epothilone B yielded results very similar to those obtained with β:T238A tubulin: Stu2 coated the lattice, and polymerase activity and plus-end tracking were greatly reduced (Figure 3.6A,B). Thus, two independent perturbations that promote tubulin:tubulin interactions increase lattice binding by Stu2 while decreasing its polymerase activity. We infer that normal polymerase function requires not only that the TOG-bound tubulins be curved, but also that they resist self-association-induced straightening enough to ensure that their release from the polymerase occurs only at the microtubule end (Figure 3.6C).

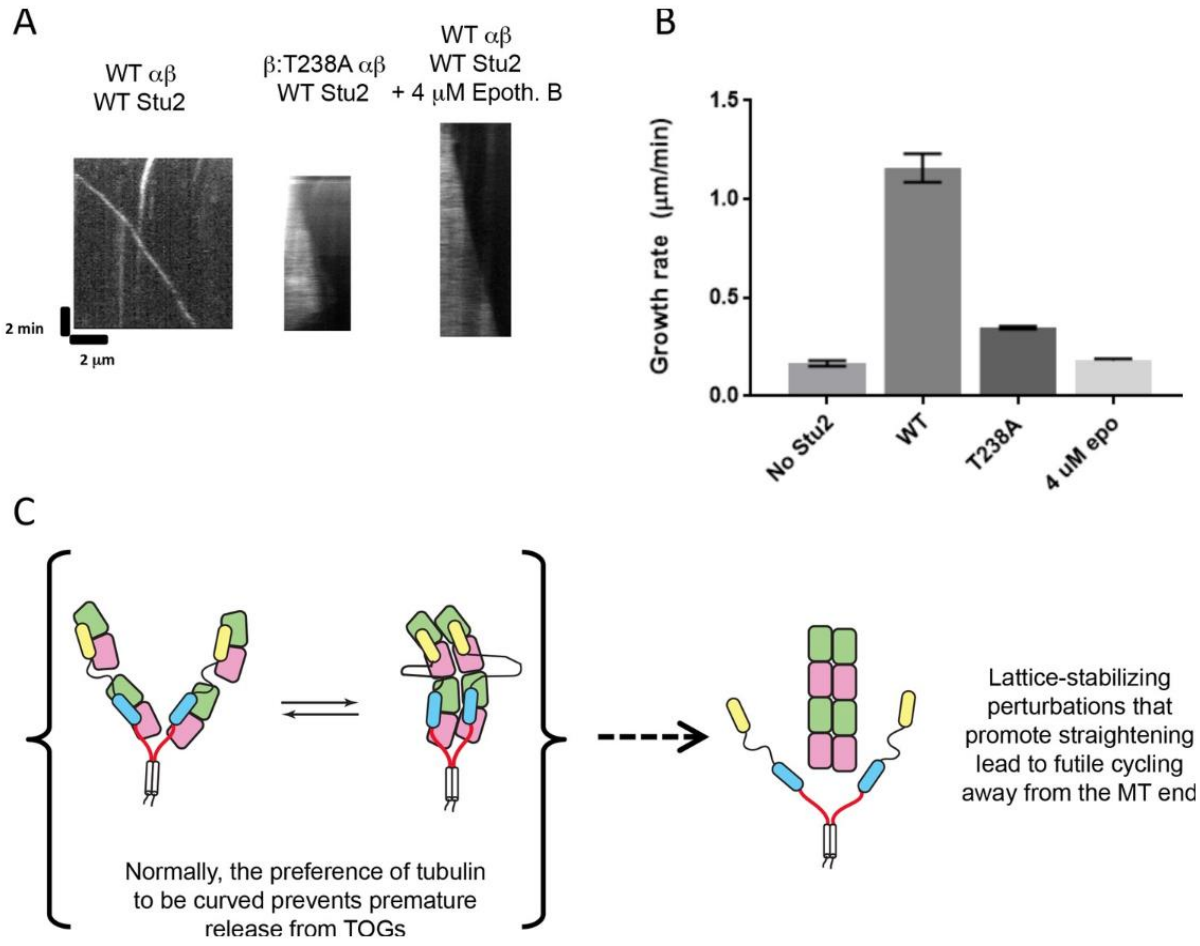

Figure 3.6. Mutation- or drug-induced perturbations that strength tubulin interactions result in loss of Stu2 polymerase activity and tip-tracking. (A) Representative kymographs showing normal end tracking, with little lattice binding by Stu2 with wild-type yeast tubulin (left). End-tracking is lost, and lattice binding is enhanced, when β:T238A mutant tubulin was used (right; this mutant stabilizes tubulin:tubulin interactions). Loss of end-tracking and gain in lattice binding also occurred in the presence of wild-type tubulin plus the microtubule-stabilizing drug Epothilone-B (right). Kymographs contain 100 nM Stu2-eGFP and 500 nM yeast tubulin (wild-type or mutant as indicated). 4 mM Epothilone B was added to right panel. (B) Stu2 shows reduced polymerase activity in the presence of Epothilone-B or β:T238A mutant tubulin. Measurements were made with 500 nM tubulin (either wild-type or T238A) and 200 nM Stu2-eGFP. N = 25 measurements for all. All error bars are SEM. (C) Cartoon illustrating a 'futile cycling' to explain the gain in lattice binding associated with perturbations that strengthen tubulin:tubulin interactions. The preference of tubulin to be curved normally prevents release from TOGs away from the microtubule end. When tubulin:tubulin interactions are strengthened by drug- or mutation-induced perturbation, straightening becomes easier and Stu2 can prematurely release its TOG-bound tubulins away from the microtubule end.

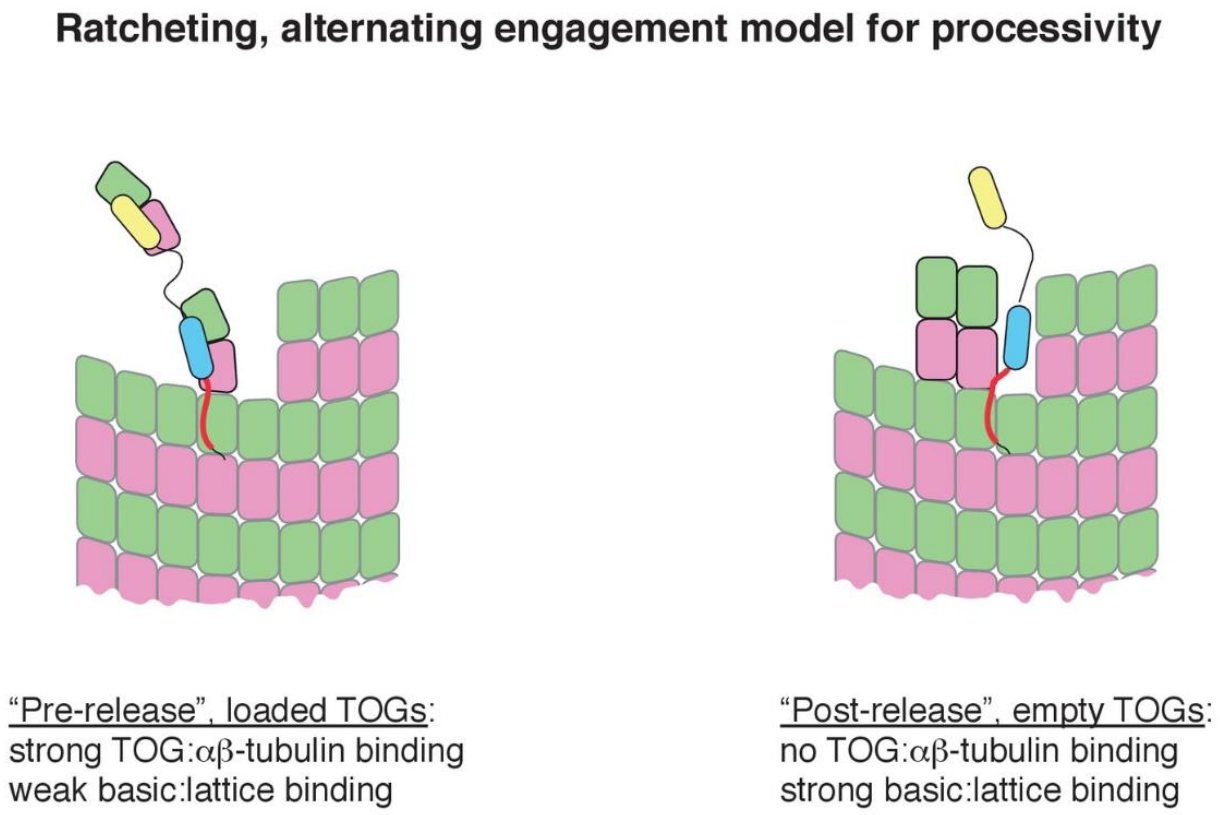

Figure 3.7. Speculative 'ratcheting' model for processivity. The model was inspired by the fact that the TOG:tubulin engagement status regulates the lattice-binding activity of the basic region. We assume two limiting states for Stu2 on the microtubule end: a 'loaded' state wherein the basic region binds weakly to the lattice because at least two TOGs are engaged with tubulins, and an 'empty' state wherein the basic region binds strongly to the lattice because the TOGs have released their tubulins to the microtubule. In this 'post-release' state, strong interactions between the basic region and the lattice help retain the empty polymerase near the growing end where it is poised to capture 'fresh' unpolymerized tubulins for another round of activity. Capture and incorporation of fresh tubulins drives movement with the growing end.

Discussion

Stu2 variants with TOG1 or TOG2 as the only active TOGs (i.e. competent to bind tubulin) were each functional polymerases. Thus, the quantitative measurements of polymerase activity reported here show that while polymerase activity requires at least two TOG domains, the two TOGs need not be different types. Monomeric Stu2 variants with a 'dimer equivalent' basic domain stimulate elongation to a comparable extent as homodimeric variants with an equal number of tubulin-binding TOG domains, so polymerase activity also does not depend strongly on oligomerization state. That monomeric and dimeric Stu2 variants can have comparable activity indicates that polymerase activity is largely insensitive to the way that the TOGs are linked. Indeed, in the monomeric Stu2-Δcc-2xBasic variant TOG1 is linked to TOG2 by the natural ~70 amino acid linker. However, in the dimeric Stu2 (TOG1-TOG2*) variant the two active TOG1s are linked by two much longer segments that encompass the natural linker, the mutated TOG2 domain, and the ~100 amino acid basic region that connects to the coiled-coil. These new findings are broadly consistent with the tethering-based mechanism we proposed previously (Ayaz et al., 2014).

We made multiple observations that were not predictable from structural and biochemical properties of isolated TOGs. These include (i) the 'positional' separation of function between the N-terminal and basic-proximal TOG domains in Stu2, (ii) the antagonism between TOG:tubulin and polymerase:lattice binding, and (iii) the loss of polymerase activity that accompanies perturbations that strengthen tubulin:tubulin interactions. These findings provide new insights into the molecular logic and functional design of these polymerases, and their implications for mechanism will be discussed in subsequent sections.

A positional separation of function is important for polymerase activity

Stu2(TOG1*-TOG2) and Stu2(TOG1-TOG2*) were present on the microtubule end in different amounts (Figure 3.2B), showed different processivity (Figure 3.3C,D), and had different specific activity (Figure 3.2C). Polymerase activity was completely lost when the basic-proximal TOG2 domain was deleted (TOG1-ΔTOG2 or TOG2-ΔTOG2), even though inactivating TOG2 mutations were tolerated (Stu2(TOG1-TOG2*) or Stu2(TOG2-TOG2*)). Our data clearly demonstrate position-dependent requirements for TOG function: the loss of polymerase activity caused by deletion of the TOG2 domain (TOG1-ΔTOG2) was not rescued by replacing TOG1 with TOG2 (TOG2-ΔTOG2). There may also be a weaker separation of function along TOG identity: Stu2(TOG1-TOG1), an 'all TOG1' variant, was less active than Stu2(TOG2-TOG2) *in vitro* and in genetic rescue assays (Figure 3.1E). That polymerase activity necessitates a TOG domain next to the basic region – even if that TOG has been inactivated for tubulin binding – indicates that some yet-to-be-determined distinctive feature there is important for polymerase activity.

Deletion of the TOG2 domain eliminated plus-end selective localization (Figure 3.2D) in addition to abolishing polymerase activity (Figure 3.2—figure supplement 1A). Yet Stu2(TOG1-ΔTOG2) retains what we thought should have been the minimal requirements for plus-end localization: TOG domains that bind preferentially to the curved conformation of tubulin (two TOG1s in the case of Stu2(TOG1-ΔTOG2); Stu2(TOG2-ΔTOG2) polymerases also did not localize to the plus end) and a basic region that provides lattice-binding affinity. Stu2 variants that only contained a single 'active' TOG domain (e.g. Stu2(TOG1*-TOG2)-Δcc-2xBasic) also failed to show plus-end specific localization or polymerase activity. Thus, plus-end specific localization requires at least two active TOGs and interactions with unpolymerized tubulin, the

same requirements for polymerase activity. The simplest explanation for these shared minimal requirements is that plus-end specific localization actually depends on polymerase activity.

Unpolymerized tubulin controls lattice binding by the basic region

A synthetic polymerase can be constructed from TOG1-TOG2 and an unrelated basic element (Widlund et al., 2011). For this and other reasons, the basic region has been assumed to be an independently acting appendage to the TOGs. However, under otherwise identical conditions, we showed that 'empty' polymerases (no tubulin bound to the TOGs) were robustly recruited along the entire length of the microtubule but 'full' polymerases (TOGs engaged with unpolymerized tubulin) only bound at the tip. That lattice binding is antagonized by TOG:tubulin interactions represents an unexpected design principle of the polymerase that appears to be conserved in polymerases from higher eukaryotes (Figure 3.5D). These findings indicate that there is a more intimate relationship between the TOGs and the basic region than previously thought, but we can only speculate about the underlying molecular mechanism. Tubulin-induced antagonism of lattice binding requires interactions between the TOG-bound tubulins (Figure 3.5B,C); it seems possible that these tubulin:tubulin interactions could either alter the overall conformation of Stu2 or provide a hybrid binding site that can compete for the basic region. Other models are possible, and more work will be required to unambiguously define the mechanism.

Stu2 and XMAP215 can both diffuse on the microtubule lattice in a way that depends on their basic regions and on the negatively charged C-terminal tails of α- and β-tubulin (Brouhard et al., 2008; Podolski et al., 2014), but our data now show that these lattice interactions are

attenuated when the TOGs are engaged with unpolymerized tubulins. Thus, compared to empty polymerases, polymerases carrying tubulins must be specifically disadvantaged for diffusing on the lattice. This in turn means that polymerases diffusing to the microtubule end will for the most part arrive 'empty'. Consequently, diffusive 'tubulin shuttling' to the end will make little contribution to polymerase activity.

Futile cycling of the polymerase occurs when tubulin self-assembly contacts are too strong

Surprisingly, mutation- or drug-induced perturbations that promote tubulin self-association and 'straightening' (Bode et al., 2002; Elie-Caille et al., 2007; Geyer et al., 2015) led to a substantial reduction in maximal polymerase activity. These perturbations also caused Stu2 to coat the microtubule lattice in the presence of unpolymerized tubulin. This concomitant loss of plus-end localization and polymerase activity provides additional evidence consistent with the idea that end localization and polymerase activity are inseparable. Whether in the presence of epothilone and wild-type tubulin, or in the presence of β:T238A tubulin, Stu2 behaved as if its TOG domains were empty. Yet both TOG1 and TOG2 bind to β:T238A tubulin with comparable affinity as they bind to wild-type (Geyer et al., 2015), so some other mechanism must account for the loss of polymerase activity with these perturbations.

The ability of a single polymerase to bind multiple tubulins results in a high local concentration of tubulin. How might perturbations that favor tubulin self-association actually reduce polymerase activity? Under normal circumstances (wild-type tubulin without Epothilone present), even the high local concentration of TOG-bound tubulins is presumably not sufficient to overcome the energetic cost of tubulin straightening. This barrier to straightening must help

prevent premature tubulin release from TOGs away from the microtubule end. Consequently, the preference of tubulin to be curved antagonizes polymerase binding along the body of the microtubule. By contrast, in the presence of mutation- or drug-induced perturbations that strengthen tubulin self-association and straightening, Stu2 behaves as if it were empty: it binds the lattice without detectable end preference. Thus, diminishing the energetic cost of self-association-induced tubulin straightening must lead to nonproductive release of polymerase-bound tubulins away from the microtubule end. That this nonproductive release also eliminates preferential end binding by Stu2 reveals an unanticipated link between polymerase mechanism and the tubulin conformation cycle. If tubulin straightens too easily, polymerase activity is lost to futile cycling, in which straightening-induced release from TOGs is no longer restricted to the microtubule end.

Concluding remarks

Stu2/XMAP215 family polymerases have been compared to formins (Brouhard et al., 2008), which are unrelated polymerases that promote fast elongation of actin filaments (reviewed in (Goode & Eck, 2007)). This comparison no longer seems apt. For the highly processive formins, end localization can be separated from polymerase activity (Kovar, Harris, Mahaffy, Higgs, & Pollard, 2006; Li & Higgs, 2003; Otomo et al., 2005; Pruyne et al., 2002). However, in modestly processive Stu2, end localization and polymerase activity appear to be inseparable. This and other findings about Stu2 are reminiscent of a different actin polymerase, Ena/VASP. Indeed, Ena/VASP proteins enhance actin elongation through a tethering mechanism (Breitsprecher et al., 2011; Hansen & Mullins, 2010; Winkelman, Bilancia, Peifer, & Kovar, 2014) that uses WH2-like domains, some of which operate analogously to TOGs because they

bind preferentially to unpolymerized (actin) subunits ((Bachmann, Fischer, Walter, & Reinhard, 1999; Huttelmaier et al., 1999). Ena/VASP proteins share three other functional characteristics with Stu2 that formins do not: (i) Ena/VASP proteins are only weakly processive, (ii) their polymer 'side binding' is attenuated in the presence of unpolymerized monomers, and (iii) their end localization requires interactions with unpolymerized monomers (Hansen and Mullins, 2010). For both Stu2 and for Ena/ VASP, it seems that processivity emerges from the ability of the polymerase to alternate between stronger and weaker states of lattice association in a way that is controlled by whether or not unpolymerized subunits are bound (Figure 3.7; see also [Hansen and Mullins, 2010; Breitsprecher et al., 2011]). While for Stu2 it is clear that tethering-based transfer of monomers from TOGs to the polymer end can promote faster elongation, some other post-delivery mechanism is required to maintain the polymerase at the microtubule end for subsequent rounds of delivery. Ratcheting by alternating engagement between TOGs and the basic region is a design principle of the polymerase that provides a simple conceptual model to explain its processive action.

CHAPTER FOUR

Conclusions and Future Directions

Studying a stabilizing mutation in β-tubulin

Our quantitative characterization of the β-tubulin mutant, T238A, was one of the first *in vitro* studies performed on a tubulin mutant. Overexpression of this mutant from *S. cerevisiae* allowed us to selectively purify and explore the effects of this mutation in the context of both free tubulin heterodimers and microtubule dynamic instability. Characterization of its dynamics *in vitro* revealed that the mutation produces hyperstable microtubules. Mutant microtubules grew very similarly to wild-type tubulin, indicating that the biochemistry of elongation between the two samples was very similar. However, the mutant tubulin produced microtubules that were highly resistant to catastrophe and shrank approximately 100-fold slower than wild-type yeast microtubules. Biochemical analyses showed that there were no significant changes to the conformational state of tubulin in solution nor throughout the microtubule lattice, as assessed by AUC experiments with the TOG domains from Stu2 and negative stain electron microscopy. Extensive radio ligand GTP experiments failed to detect gross changes in either the GTP hydrolysis rate or the sequestering of inorganic phosphate (Pi) after hydrolysis in mutant microtubules relative to wild-type. Depolymerization assays of stabilized mutant microtubules with TOG domains showed that mutant microtubules were far less susceptible to tubulin removal by the TOGs when compared to wild-type microtubules. Major changes in the body of the microtubule were seen in the presence of Bim1. Under conditions where wild-type microtubules showed fluorescent Bim1 comets bound near the microtubule end, mutant microtubules were completely covered with Bim1 over the entire lattice. This suggested that the mutation, by providing additional room in the core of β-tubulin, had uncoupled nucleotide hydrolysis

cycle from the conformational cycle. Although the mutant microtubules were capable of hydrolyzing GTP comparably to wild-type, they remained 'stuck' in an intermediate lattice state that retained high affinity for Bim1 (presumably the compacted/twisted intermediate state). For the first time, our results demonstrated the role of allostery within the microtubule lattice to control and maintain the rapid switching of states and rate of shrinking in dynamic instability. Additionally, our results also suggest a role for the conformational cycle in not only driving depolymerization from the microtubule lattice, but in acting as an allosteric 'amplifier' –if nucleotide hydrolysis is not linked to some type of physical change in the microtubule, the time scale of microtubule assembly and disassembly would be much slower than what is typically seen. This could have dramatic implications on cell organization and division, as microtubules and their capacity to quickly reorganize within the cell are crucial components to cell survival.

Future Directions and Preliminary Results

Refining our helical reconstructions to account for the seam

To gain further insight into the structural changes that may accompany β:T238A microtubules, we are attempting to solve high resolution structures of β:T238A human microtubules (described in Chapter 2). Preliminary cryo-EM reconstructions using helical symmetry have yielded mutant human microtubule structures that contain 14-protofilmanets at a fairly high resolution (approximately 4 Å). However, the use of helical symmetry results in the mixing of α- and β-tubulin heterodimers, which lowers the overall resolution of the structure. Additionally, the presence of a seam in a true microtubule is not accounted for in a helically reconstructed sample. To define and preserve the presence of the seam, and prevent mixing of

the tubulin monomers, we are currently working to modify and apply a 'seam-preserving' reconstruction algorithm to our reconstructions. This algorithm is based on prior work from the Nogales lab (Zhang & Nogales, 2015).

The idea behind this algorithm is to create 'super particles' (many single particles averaged together from the same microtubule to increase the signal:noise ratio in the image) to score against a reference microtubule that contains a seam—the alignment with the "best" score dictates the proper orientation of the particle in reference to the seam and α- and β-tubulin placement. Although it seems relatively straight forward, there are many detailed steps that must be accounted for along the way. In RELION, orientation of a particle with respect to a 3D reference is dictated by five alignment parameters: x and y translations (referred to as shx and shy), and three Euler angles, ψ in-plane rotation, θ out-of-plane tilt typically 90°, φ azimuthal angle around MT axis. Because tubulin monomers are so structurally similar, especially in low resolution features that tend to drive the alignment, particles from the same microtubule tend to be assigned inconsistent φ angles, which directly affects their x and y translations. In order to produce high signal: noise super particles, we must modify their alignment parameters so that all raw images from the same microtubule have consistent φ angles and x and y translations. Currently, we have developed an algorithm that allows us to extract groups of seven raw particles from the same microtubule, unify their φ angles and x and y translations, and align and average the particles together into one 'super particle' (Figure 4.1).

To determine the correct placement of the super particle against the reference, and therefore the proper placing of the seam, we will perform iterative reconstructions of each particle against the reference, rotating the particle by a single protofilament each consecutive reconstruction. In these reconstructions, we will vary the x and y translations and angles of each

super particle to move each particle onto each of the individual 14 protofilaments. The idea here is that aligning every particle against each protofilament during separate reconstructions will produce a unique score for each run (see output from example reconstruction in Figure 4.2 A). After 28 runs (14 to check each possible orientation of the seam, done with and without a monomer shift), the scores from each iteration will be compared and the optimal score will indicate what the 'correct' angles and x/y translations are for that particle to allow for proper orientation of the seam and the tubulin heterodimer. We would then go back and re-assign the correct angles and translations to each super particle, re-extract the raw particles from the super particles and then perform a 3D reconstruction with these properly assigned raw particles to produce the 'true' microtubule lattice where the tubulin monomers are properly identified and the seam is present.

At the moment, we are struggling with the scoring portion of this workflow. While we have developed a method that allows us to iteratively reconstruct each super particle against each individual protofilament in the reference model, we have failed to see scoring trends similar to what was reported in Zhang & Nogales, 2015 (Figure 4.2 B). We are starting to make progress in this area after observing that our reconstructed microtubule might not be close enough to the reference map we have been using, based on the rise and twist parameters of the map against our structure. We are in the process of trying these scoring portion using different 3D reference models that more closely fit our reconstructed lattice. Throughout our analysis, we have only been using RELION software to perform all of these steps; however, the method that we're following used multiple different software platforms to achieve this overall algorithm. In particular, they used FREALIGN to score their particles. If the scoring algorithms between RELION and FREALIGN are not similar, we may not see the same type of obvious trends, or

changes in score to the same degree, as was previously shown. Additionally, in our data sets we have kept all the raw particles that were originally picked in the Autopicking algorithm of RELION. It is possible that there are a high number of 'junk' particles (low signal: noise) that are affecting the overall quality of the super particles and thus the scoring in the reconstruction steps. We may need to go back and exclude junk particles from the overall data set. Finally, we have been using a 14-protofilament reference microtubule model that was solved in a GDP state, as it was one of the only 14-protofilmanet references available that did not contain a marker protein. This could be affecting how well our super particles are comparing against the reference, especially if our mutant microtubules are in a different conformational state than the reference model. In the future, we plan to make new super particles against a 14-protofilament microtubule model in a GMPCPP (GTP) state to determine whether this affects the overall scoring output.

We have made large strides in creating and modifying protocols to allow us to unify, align and average super particles, and to perform reconstructions of these super particles by translating them against a reference model. Much work remains to be done to ensure that the algorithm for solving naked microtubules structure with a proper seam is robust and reliable and to confirm that the scoring function is working properly for particles picked from the same microtubule. Once we are able to properly score and re-classify the alignment parameters on each super particle, we will be very close to reconstructing naked mutant microtubules with proper seam placement and correct αβ-tubulin register. This will allow us to answer questions in regards to the conformational state of the mutant microtubule lattice in both GTP and GDP nucleotide states.

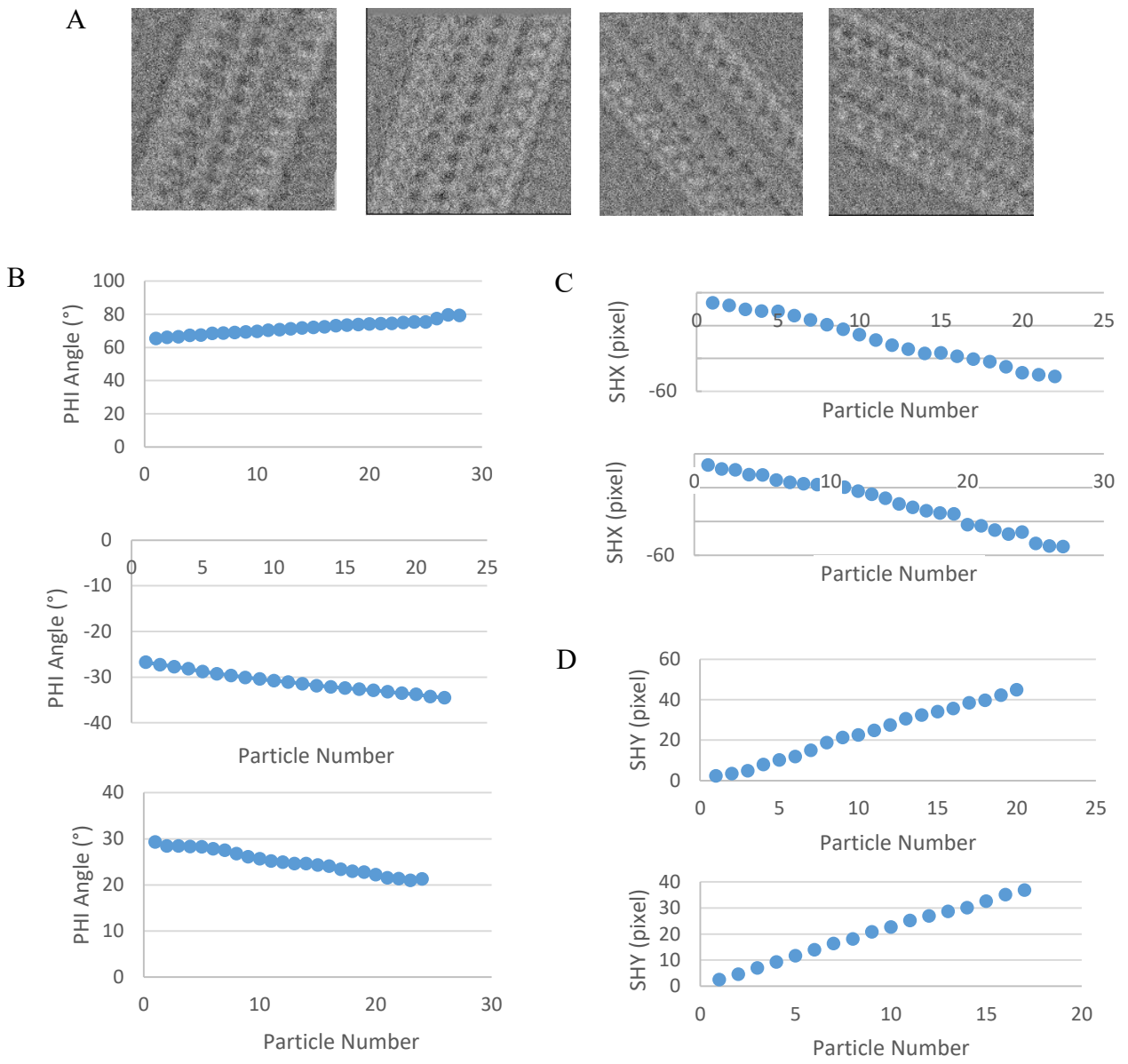

Figure 4.1: Unifying raw particle alignment parameters to create high quality super particles. A. Representative images of four individual super particles from four unique microtubules. These super particles were made by aligning and averaging seven raw particles together after unifying their phi angles and x/ y translations. B. Example plots of PHI angle as a function of particle number demonstrate that our algorithm is properly aligning particles picked from the same microtubule. C and D. Example plots of x (C) and y (D) alignments that are resulted from our alignment algorithm.

A

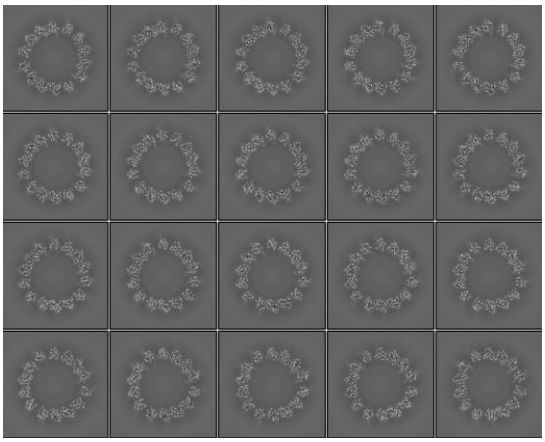

B

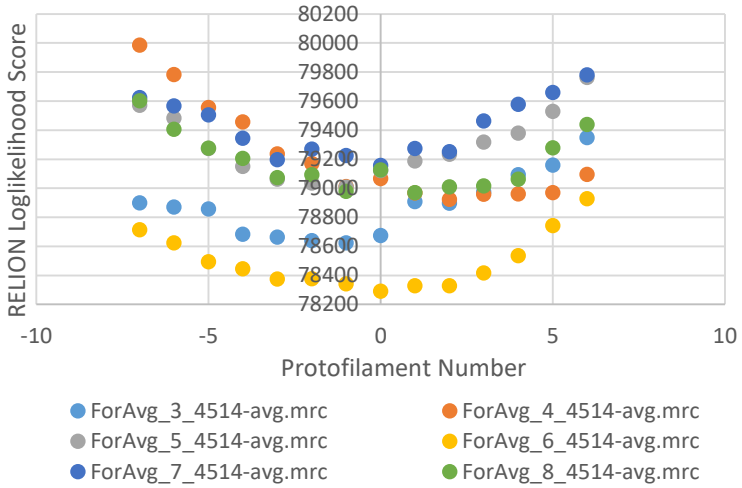

Figure 4.2: Scoring super particles against a reference model by performing a 3D reconstruction is leading to poor resolution structures and scoring trends that produce inconsistent scoring peaks for particles from the same microtubule. A. Z-slice through the output of a 3D reconstruction from a prior scoring run, using the '0' protofilament run. Notice the poor signal: noise in the images, but the presence of 14 protofilaments in the structure. B. Representative scoring plot assessing the log likelihood score output from RELION against the protofilament number assigned to that particle during each reconstruction. In this plot, six super particles are being compared. All super particles in the plot were produced from the same original microtubule and thus should all have very similar score outputs. While the trend in the score is present, with a local minimum near the '0' protofilament, some particles reach their maximum and minimum scores at different protofilament numbers. Because these particles are all from the same original microtubule segment, it would be expected that they should look almost identical in scoring values.

Solving the crystal structure of a TOG-bound T238 mutant tubulin

Although we are hypothesizing that there will be differences in the conformational state of the microtubule lattice in the presence of the T238 mutants, it may be that the lattice structures are identical to wild-type. One possibility is that there may be subtle difference to the solution state conformation of tubulin. To determine if I can observe structural changes to the 'curved' soluble form of either T238A or T238V mutants, I am working to crystallize a complex between T238A-LR1/T238V-LR1 and the TOG2 domain from Stu2p. I am working with the LR1 β-tubulin longitudinal blocked mutations to prevent tubulin from polymerizing at the high concentrations required for crystallization. The choice to crystallize these tubulin mutants with the TOG2 domain was two-fold: not only can the domain help to stabilize the tubulin in solution, but if we can successfully solve the structure we will be able to assess any changes in binding between the T238 mutants against wild-type tubulin bound to the TOG domains.

Attempting to crystallize these more difficult, low expression tubulin mutants, presents many challenges. My years of experience handling these samples provides me with the right background to attempt this project. I have optimized the purifications for these tubulin variants such that I am able to purify yields close to 2.5-3 mg/mL (~25-30 μM) of protein. Sample preparation for TOG2 has also been improved from previous protocols which has resulted in higher yield purifications of the domain with samples at 30 μM. Initial screens were done with T238V-LR1, because it was thought that this protein would be more amenable to being concentrated to very high amounts with little aggregation. In setting up samples and selecting screens, I am choosing to follow an approach similar to a previous graduate student in the lab who successfully solved structures of wild-type yeast tubulin bound to both TOG domains from Stu2 several years ago. This will include focusing on screening conditions that vary the amount

of type of polyethylene glycol (PEG) solutions (example: PegRX, PegION screens from Hampton Research).

I performed a first round of screens with T238V-LR1/TOG2 samples near a concentration of ~ 1.5 mg/mL (15 µM) in RB100 buffer (25 mM Tris pH 7.5, 100 mM NaCl, 1 mM $MgCl_2$, 1 mM EGTA, 50 µM GTP). Screens were set-up with 1:1 protein: screen ratios at 20°C. While many conditions produced phase separation or small amounts of granular precipitate, none of the conditions yielded crystals or crystal-like structures. As a second attempt, I prepared the same screens with T238V-LR1/TOG2, again in RB100. This time I concentrated the final sample to ~ 2.5 mg/mL (25 µM), and set-up trays with 2:1 protein: screen ratios at 20°C. These screens produced several crystal hits, many of which were UV positive. Most notably was the production of spore-like, UV positive crystal shards in two separate conditions in the PegION screen that grew within 24 hours (well H2: 0.05 M Citric acid, 0.05 M BIS-TRIS propane/ pH 5.0, 16% w/v PEG 3350 and well E3: 0.1 M sodium malonate pH 5.0, 12% w/v PEG 3350) (Figure 4.3 A and B). Several years ago, Luke attempted to crystallize these same samples in very similar conditions. Reassuringly, he saw very similar spore-like shard crystals in the same conditions as I've now produced in the PegION screens. This is a positive sign that the crystals are real and now need to be optimized to produce larger, single crystals. To optimize these samples, I will prepare custom screens that will focus on the conditions in well H2. I will make a 6x4 screen where I vary the PEG amount from 12-22%, in increments of 2%; I will also vary the pH of the BIS-TRIS propane buffer from 4.8 to 5.4, in increments of 0.2. We are hoping to find a condition where the crystals will grow as individual shards and not clusters, so that we can loop the samples and shoot in the near future.

After having positive hits using T238V-LR1 samples, I decided to attempt growing crystals with the more challenging T238A-LR1 mutant. I prepared T238A-LR1/TOG2 samples to a final concentration of ~ 2.4 mg/ mL (24 μM), in RB100, and prepared PegION and PegRX screens with 2:1 protein: screen ratios at 20°C. After 24 hours spore-like shard crystals appeared in wells E3 and H2 of the PegION screen, just as had been seen from the T238V-LR1 samples (Figure 4.2 C and D). These crystal shards were highly UV positive, consistent with the fact that the crystal most likely contains my protein of interest. I will now optimize these crystals, identical to my plans for optimization of T238V-LR1, as both binding samples grew identical crystals in identical conditions. Once I am able to optimize the crystal growth to produce single crystals that are large enough to shoot, we will shoot the crystals and hopefully solve the structures of both T238A-LR1 and T238V-LR1 bound to TOG2.

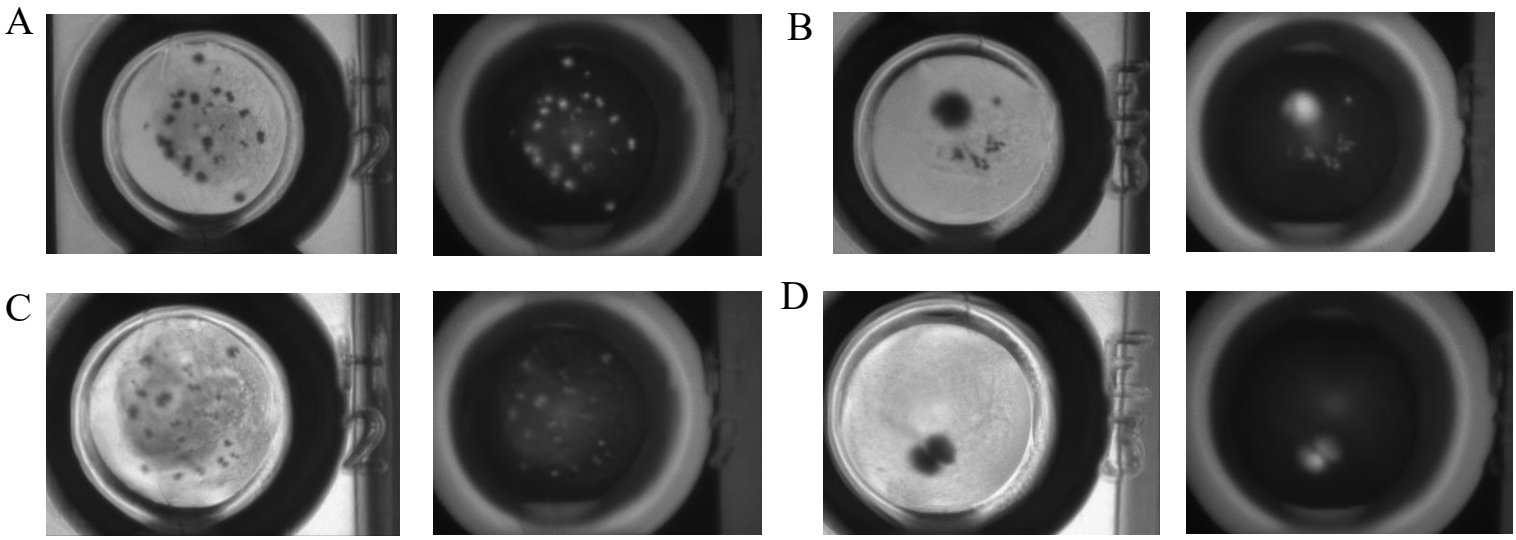

Figure 4.3. UV-positive crystal hits from screening trays for T238V-LR1/TOG2 and T238A-LR1/TOG2 samples. All bright field images are on the left and all UV images are on the right for all figure panels. A. Multiple spore-like shard crystals of T238V-LR1/TOG2 in well H2 from PegION screen. These crystals were seen after 24 h but picture was taken at day 7. B. More spore-like shard crystals of T238V-LR1/TOG2 in well E3 from PegION screen. These crystals were seen after 48 hours but imaged at day 7. C. Multiple spore-like shard crystals of T238A-LR1/TOG2 in well H2 from PegION screen. These images were taken at ~20 hour after preparing screen. D. More spore-like shard crystals of T238V-LR1/TOG2 in well E3 from PegION screen. These images were taken at ~20 hour after preparing screen.

Dissecting the molecular mechanism of Stu2

I studied full-length Stu2 to gain insight behind how the domain composition and organization of the protein effects polymerase activity, processivity and end-tracking. By using a quantitative all-yeast *in vitro* reconstitution system, I have revealed new insights into the mechanism of polymerase function that were never previously seen. Mutational analysis of the TOG domains showed that the polymerase does not require different 'flavors' of TOG domains (TOG1 or TOG2 specifically) to function, but does require the presence of two functional tubulin-binding TOGs. Altering the charge of the basic domain in both the monomeric and dimeric proteins revealed that dimerization is not a necessary component for functional polymerase activity, as long as the protein has adequate charge in it SK-rich region to properly associate with the microtubule lattice. I uncovered a new role for the basic proximal TOG domain (in this case, TOG2) by demonstrating that it functions to control end localization: mutating TOG2 decreased overall polymerase activity, but removal of TOG2 from its basic-proximal region abolished protein end-localization and overall function. Prior to our findings, it was believed that TOG1 and TOG2 were approximately equivalent in function and could be swapped interchangeably throughout the protein. Measurements of end-residence time and quantifications of the number of polymerases on the microtubule end both work to control the total output of polymerase activity. I have shown that TOG engagement to tubulin controls the strength of interaction between the basic domain at the microtubule lattice. When the TOG domains are 'empty' (not bound to free tubulin dimers), Stu2 can bind tightly to the microtubule lattice; once the TOG domains bind free tubulin, Stu2 is no longer able to engage with the microtubule and so releases from the lattice. This condition is specific to ability of the bound

tubulin dimers to form lateral contacts. If the tubulin dimers are incapable of interacting laterally, Stu2 is retained to the microtubule lattice even when the TOGs are bound to tubulin.

Characterization of Stu2 in the presence of microtubule stabilizing conditions, specifically through the use of a stabilizing mutant such as β:T238A or chemical reagents such as epothilone-B, revealed that the tubulin conformational cycle has large impacts on polymerase activity. Any type of perturbation that stabilizes a tubulin: tubulin interaction within the polymerase (ie between tubulin dimers that are bound by the TOG domains) results in 'futile cycling' of Stu2. The TOG domains are known to bind with high affinity to the curved conformation of tubulin. When the TOGs engage with certain tubulin mutants or wild-type tubulin in the presence of epothilone, tubulin dimers are able to undergo conformational changes and form lattice-like contacts while still bound to the TOG domains. If these polymer interactions and conformational changes occur before Stu2 can reach the microtubule tip to 'drop off' the tubulin dimers to the plus end, the TOG domains will end up releasing the tubulin dimers because they can no longer tightly bind the lattice-like conformation of tubulin. This results in 'futile cycling' as it produces an excess of empty polymerases that are incapable of performing their function, and an excess of tubulin intermediate products in solution that are not capable of being incorporated into the microtubule lattice. Therefore, the tubulin conformational cycle must be tightly regulated in regards to TOG binding to prevent premature release from the TOG domains before the polymerase has reached the microtubule end.

Taken together, these results have many implications, but importantly, they point to the development of a new way to explain processivity of the polymerase on the microtubule end. A ratcheting/altering engagement mechanism can simply explain polymerase processivity: when the TOG domains are bound to tubulin, the basic domain has very low affinity for the

microtubule lattice, allowing for release of the polymerase to properly target and localize to the microtubule end. Once at the plus-end, Stu2 can deliver its tubulin dimers into the polymer. Empty TOGs allow for a high affinity interaction between the basic domain and microtubule lattice, localizing and retaining Stu2 at the plus-end long enough to capture new tubulin dimers, release from the microtubule, incorporate the dimers into the polymer, and then re-engage the lattice at the plus end. This 'see-saw' type motion prevents Stu2 from diffusing away from the microtubule in between successive rounds of tubulin additions.

There are a number of unanswered questions and new areas to explore around this polymerase family, particularly in regards to Stu2. How exactly does the regulation of tubulin-bound TOG domains control the ability for Stu2 to tightly engage the microtubule lattice? What drives Stu2 to the microtubule end? Is it possible to solve a cryo-EM structure of tubulin-bound TOG domains in full-length Stu2 to determine what the intermediate tubulin-bound TOG complex looks like, particularly in regards to what type of lateral contacts are being formed between tubulin dimers? Recent work has demonstrated the ability of XMAP215 to function as a microtubule nucleating factor that interacts with γ-TuRC (tubulin ring complex) (Thawani et al., 2018). Could Stu2 possess this same ability and function as a microtubule nucleating factor that interacts with the yeast γ-tubulin complex? Now that we have a basic understanding as to the requirements and the general mechanism behind this polymerase family, is it possible to build a 'Frankenstein' polymerase as a 'proof of principle' experiment? By combining domains from multiple family members and stringing them together, one could try to recapitulate tip-tracking and polymerase activity in an *in vitro* system. Finally, further exploration into interactions between Stu2 and other MAPs within the cell, is a large area that still yields a plethora of questions. What other proteins does Stu2 help to localize to the microtubule end?

How does this affect the function of Stu2, not only as a polymerase, but as a key factor in mitosis? These questions, and many more that are still yet to be asked, are an exciting region of science that will yield interesting and critical results in the years to come.

BIBLIOGRAPHY

Al-Bassam, J., & Chang, F. (2011). Regulation of microtubule dynamics by TOG-domain proteins XMAP215/Dis1 and CLASP. *Trends Cell Biol, 21*(10), 604-614. doi:10.1016/j.tcb.2011.06.007

Al-Bassam, J., Larsen, N. A., Hyman, A. A., & Harrison, S. C. (2007). Crystal structure of a TOG domain: conserved features of XMAP215/Dis1-family TOG domains and implications for tubulin binding. *Structure, 15*(3), 355-362. doi:10.1016/j.str.2007.01.012

Al-Bassam, J., van Breugel, M., Harrison, S. C., & Hyman, A. (2006). Stu2p binds tubulin and undergoes an open-to-closed conformational change. *J Cell Biol, 172*(7), 1009-1022. doi:10.1083/jcb.200511010

Altschul, S. F., Madden, T. L., Schaffer, A. A., Zhang, J., Zhang, Z., Miller, W., & Lipman, D. J. (1997). Gapped BLAST and PSI-BLAST: a new generation of protein database search programs. *Nucleic Acids Res, 25*(17), 3389-3402.

Alushin, G. M., Lander, G. C., Kellogg, E. H., Zhang, R., Baker, D., & Nogales, E. (2014). High-resolution microtubule structures reveal the structural transitions in alphabeta-tubulin upon GTP hydrolysis. *Cell, 157*(5), 1117-1129. doi:10.1016/j.cell.2014.03.053

Amos, L. A. (2011). What tubulin drugs tell us about microtubule structure and dynamics. *Semin Cell Dev Biol, 22*(9), 916-926. doi:10.1016/j.semcdb.2011.09.014

Ayaz, P., Munyoki, S., Geyer, E. A., Piedra, F. A., Vu, E. S., Bromberg, R., . . . Rice, L. M. (2014). A tethered delivery mechanism explains the catalytic action of a microtubule polymerase. *Elife, 3*, e03069. doi:10.7554/eLife.03069

Ayaz, P., Ye, X., Huddleston, P., Brautigam, C. A., & Rice, L. M. (2012). A TOG:alphabeta-tubulin complex structure reveals conformation-based mechanisms for a microtubule polymerase. *Science, 337*(6096), 857-860. doi:10.1126/science.1221698

Bachmann, C., Fischer, L., Walter, U., & Reinhard, M. (1999). The EVH2 domain of the vasodilator-stimulated phosphoprotein mediates tetramerization, F-actin binding, and actin bundle formation. *J Biol Chem, 274*(33), 23549-23557.

Bechstedt, S., & Brouhard, G. J. (2012). Doublecortin recognizes the 13-protofilament microtubule cooperatively and tracks microtubule ends. *Dev Cell, 23*(1), 181-192. doi:10.1016/j.devcel.2012.05.006

Bode, C. J., Gupta, M. L., Jr., Reiff, E. A., Suprenant, K. A., Georg, G. I., & Himes, R. H. (2002). Epothilone and paclitaxel: unexpected differences in promoting the assembly and stabilization of yeast microtubules. *Biochemistry, 41*(12), 3870-3874.

Brautigam, C. A. (2015). Calculations and Publication-Quality Illustrations for Analytical Ultracentrifugation Data. *Methods Enzymol, 562*, 109-133. doi:10.1016/bs.mie.2015.05.001

Breitsprecher, D., Kiesewetter, A. K., Linkner, J., Vinzenz, M., Stradal, T. E., Small, J. V., . . . Faix, J. (2011). Molecular mechanism of Ena/VASP-mediated actin-filament elongation. *EMBO J, 30*(3), 456-467. doi:10.1038/emboj.2010.348

Brouhard, G. J., & Rice, L. M. (2014). The contribution of alphabeta-tubulin curvature to microtubule dynamics. *J Cell Biol, 207*(3), 323-334. doi:10.1083/jcb.201407095

Brouhard, G. J., & Rice, L. M. (2018). Microtubule dynamics: an interplay of biochemistry and mechanics. *Nat Rev Mol Cell Biol, 19*(7), 451-463. doi:10.1038/s41580-018-0009-y

Brouhard, G. J., Stear, J. H., Noetzel, T. L., Al-Bassam, J., Kinoshita, K., Harrison, S. C., . . . Hyman, A. A. (2008). XMAP215 is a processive microtubule polymerase. *Cell, 132*(1), 79-88. doi:10.1016/j.cell.2007.11.043

Buey, R. M., Diaz, J. F., & Andreu, J. M. (2006). The nucleotide switch of tubulin and microtubule assembly: a polymerization-driven structural change. *Biochemistry, 45*(19), 5933-5938. doi:10.1021/bi060334m

Burns, R. G. (1991). Alpha-, beta-, and gamma-tubulins: sequence comparisons and structural constraints. *Cell Motil Cytoskeleton, 20*(3), 181-189. doi:10.1002/cm.970200302

Cooper, J. R., Wagenbach, M., Asbury, C. L., & Wordeman, L. (2010). Catalysis of the microtubule on-rate is the major parameter regulating the depolymerase activity of MCAK. *Nat Struct Mol Biol, 17*(1), 77-82. doi:10.1038/nsmb.1728

Desai, A., & Mitchison, T. J. (1997). Microtubule polymerization dynamics. *Annu Rev Cell Dev Biol, 13*, 83-117. doi:10.1146/annurev.cellbio.13.1.83

Diaz, J. F., Valpuesta, J. M., Chacon, P., Diakun, G., & Andreu, J. M. (1998). Changes in microtubule protofilament number induced by Taxol binding to an easily accessible site. Internal microtubule dynamics. *J Biol Chem, 273*(50), 33803-33810.

Dorn, J. F., Jaqaman, K., Rines, D. R., Jelson, G. S., Sorger, P. K., & Danuser, G. (2005). Yeast kinetochore microtubule dynamics analyzed by high-resolution three-dimensional microscopy. *Biophysical Journal, 89*(4), 2835-2854. doi:10.1529/biophysj.104.058461

Dougherty, C. A., Himes, R. H., Wilson, L., & Farrell, K. W. (1998). Detection of GTP and Pi in wild-type and mutated yeast microtubules: implications for the role of the GTP/GDP-Pi cap in microtubule dynamics. *Biochemistry, 37*(31), 10861-10865. doi:10.1021/bi980677n

Duellberg, C., Cade, N. I., Holmes, D., & Surrey, T. (2016). The size of the EB cap determines instantaneous microtubule stability. *Elife, 5*. doi:10.7554/eLife.13470

Edelstein, A., Amodaj, N., Hoover, K., Vale, R., & Stuurman, N. (2010). Computer control of microscopes using microManager. *Curr Protoc Mol Biol, Chapter 14*, Unit14 20. doi:10.1002/0471142727.mb1420s92

Elie-Caille, C., Severin, F., Helenius, J., Howard, J., Muller, D. J., & Hyman, A. A. (2007). Straight GDP-tubulin protofilaments form in the presence of taxol. *Curr Biol, 17*(20), 1765-1770. doi:10.1016/j.cub.2007.08.063

Flemming, W. (1965). Historical Paper. Contributions to the Knowledge of the Cell and Its Vital Processes. *J Cell Biol, 25*, SUPPL:1-69.

Fygenson, D. K., Needleman, D. J., & Sneppen, K. (2004). Variability-based sequence alignment identifies residues responsible for functional differences in alpha and beta tubulin. *Protein Sci, 13*(1), 25-31. doi:10.1110/ps.03225304

Ganguly, A., Yang, H., Sharma, R., Patel, K. D., & Cabral, F. (2012). The role of microtubules and their dynamics in cell migration. *J Biol Chem, 287*(52), 43359-43369. doi:10.1074/jbc.M112.423905

Gard, D. L., & Kirschner, M. W. (1987). Microtubule assembly in cytoplasmic extracts of Xenopus oocytes and eggs. *J Cell Biol, 105*(5), 2191-2201.

Gardner, M. K., Charlebois, B. D., Janosi, I. M., Howard, J., Hunt, A. J., & Odde, D. J. (2011). Rapid microtubule self-assembly kinetics. *Cell, 146*(4), 582-592. doi:10.1016/j.cell.2011.06.053

Gell, C., Bormuth, V., Brouhard, G. J., Cohen, D. N., Diez, S., Friel, C. T., . . . Howard, J. (2010). Microtubule dynamics reconstituted in vitro and imaged by single-molecule

fluorescence microscopy. *Methods Cell Biol, 95*, 221-245. doi:10.1016/S0091-679X(10)95013-9

Geyer, E. A., Burns, A., Lalonde, B. A., Ye, X., Piedra, F. A., Huffaker, T. C., & Rice, L. M. (2015). A mutation uncouples the tubulin conformational and GTPase cycles, revealing allosteric control of microtubule dynamics. *Elife, 4*, e10113. doi:10.7554/eLife.10113

Gigant, B., Curmi, P. A., Martin-Barbey, C., Charbaut, E., Lachkar, S., Lebeau, L., . . . Knossow, M. (2000). The 4 A X-ray structure of a tubulin:stathmin-like domain complex. *Cell, 102*(6), 809-816.

Goode, B. L., & Eck, M. J. (2007). Mechanism and function of formins in the control of actin assembly. *Annu Rev Biochem, 76*, 593-627. doi:10.1146/annurev.biochem.75.103004.142647

Griffin, B. A., Adams, S. R., Jones, J., & Tsien, R. Y. (2000). Fluorescent labeling of recombinant proteins in living cells with FlAsH. *Methods Enzymol, 327*, 565-578.

Gupta, M. L., Jr., Bode, C. J., Dougherty, C. A., Marquez, R. T., & Himes, R. H. (2001). Mutagenesis of beta-tubulin cysteine residues in Saccharomyces cerevisiae: mutation of cysteine 354 results in cold-stable microtubules. *Cell Motil Cytoskeleton, 49*(2), 67-77. doi:10.1002/cm.1021

Gupta, M. L., Jr., Bode, C. J., Thrower, D. A., Pearson, C. G., Suprenant, K. A., Bloom, K. S., & Himes, R. H. (2002). beta-Tubulin C354 mutations that severely decrease microtubule dynamics do not prevent nuclear migration in yeast. *Mol Biol Cell, 13*(8), 2919-2932. doi:10.1091/mbc.e02-01-0003

Hansen, S. D., & Mullins, R. D. (2010). VASP is a processive actin polymerase that requires monomeric actin for barbed end association. *J Cell Biol, 191*(3), 571-584. doi:10.1083/jcb.201003014

Helenius, J., Brouhard, G., Kalaidzidis, Y., Diez, S., & Howard, J. (2006). The depolymerizing kinesin MCAK uses lattice diffusion to rapidly target microtubule ends. *Nature, 441*(7089), 115-119. doi:10.1038/nature04736

Hirokawa, N., Noda, Y., Tanaka, Y., & Niwa, S. (2009). Kinesin superfamily motor proteins and intracellular transport. *Nat Rev Mol Cell Biol, 10*(10), 682-696. doi:10.1038/nrm2774

Howes, S. C., Geyer, E. A., LaFrance, B., Zhang, R., Kellogg, E. H., Westermann, S., . . . Nogales, E. (2017). Structural differences between yeast and mammalian microtubules revealed by cryo-EM. *J Cell Biol, 216*(9), 2669-2677. doi:10.1083/jcb.201612195

Huang, B. Y., & Huffaker, T. C. (2006). Dynamic microtubules are essential for efficient chromosome capture and biorientation in S-cerevisiae. *Journal of Cell Biology, 175*(1), 17-23. doi:10.1083/jcb.200606021

Huttelmaier, S., Harbeck, B., Steffens, O., Messerschmidt, T., Illenberger, S., & Jockusch, B. M. (1999). Characterization of the actin binding properties of the vasodilator-stimulated phosphoprotein VASP. *FEBS Lett, 451*(1), 68-74.

Hyman, A. A., Chretien, D., Arnal, I., & Wade, R. H. (1995). Structural changes accompanying GTP hydrolysis in microtubules: information from a slowly hydrolyzable analogue guanylyl-(alpha,beta)-methylene-diphosphonate. *J Cell Biol, 128*(1-2), 117-125.

Hyman, A. A., Salser, S., Drechsel, D. N., Unwin, N., & Mitchison, T. J. (1992). Role of GTP hydrolysis in microtubule dynamics: information from a slowly hydrolyzable analogue, GMPCPP. *Mol Biol Cell, 3*(10), 1155-1167. doi:10.1091/mbc.3.10.1155

Inoue, S. (1981). Cell division and the mitotic spindle. *J Cell Biol, 91*(3 Pt 2), 131s-147s.

Johnson, V., Ayaz, P., Huddleston, P., & Rice, L. M. (2011). Design, overexpression, and purification of polymerization-blocked yeast alphabeta-tubulin mutants. *Biochemistry, 50*(40), 8636-8644. doi:10.1021/bi2005174

Jordan, M. A., & Wilson, L. (2004). Microtubules as a target for anticancer drugs. *Nat Rev Cancer, 4*(4), 253-265. doi:10.1038/nrc1317

Kovar, D. R., Harris, E. S., Mahaffy, R., Higgs, H. N., & Pollard, T. D. (2006). Control of the assembly of ATP- and ADP-actin by formins and profilin. *Cell, 124*(2), 423-435. doi:10.1016/j.cell.2005.11.038

Li, F., & Higgs, H. N. (2003). The mouse Formin mDia1 is a potent actin nucleation factor regulated by autoinhibition. *Curr Biol, 13*(15), 1335-1340.

Liu, H., & Naismith, J. H. (2008). An efficient one-step site-directed deletion, insertion, single and multiple-site plasmid mutagenesis protocol. *BMC Biotechnol, 8*, 91. doi:10.1186/1472-6750-8-91

Machin, N. A., Lee, J. M., & Barnes, G. (1995). Microtubule stability in budding yeast: characterization and dosage suppression of a benomyl-dependent tubulin mutant. *Mol Biol Cell, 6*(9), 1241-1259.

Majumdar, S., Kim, T., Chen, Z., Munyoki, S., Tso, S. C., Brautigam, C. A., & Rice, L. M. (2018). An isolated CLASP TOG domain suppresses microtubule catastrophe and promotes rescue. *Mol Biol Cell, 29*(11), 1359-1375. doi:10.1091/mbc.E17-12-0748

Margolis, R. L., & Wilson, L. (1978). Opposite end assembly and disassembly of microtubules at steady state in vitro. *Cell, 13*(1), 1-8.

Matthews, L. R., Carter, P., Thierry-Mieg, D., & Kemphues, K. (1998). ZYG-9, a Caenorhabditis elegans protein required for microtubule organization and function, is a component of meiotic and mitotic spindle poles. *J Cell Biol, 141*(5), 1159-1168.

Maurer, S. P., Bieling, P., Cope, J., Hoenger, A., & Surrey, T. (2011). GTPgammaS microtubules mimic the growing microtubule end structure recognized by end-binding proteins (EBs). *Proc Natl Acad Sci U S A, 108*(10), 3988-3993. doi:10.1073/pnas.1014758108

Maurer, S. P., Cade, N. I., Bohner, G., Gustafsson, N., Boutant, E., & Surrey, T. (2014). EB1 accelerates two conformational transitions important for microtubule maturation and dynamics. *Curr Biol, 24*(4), 372-384. doi:10.1016/j.cub.2013.12.042

Maurer, S. P., Fourniol, F. J., Bohner, G., Moores, C. A., & Surrey, T. (2012). EBs recognize a nucleotide-dependent structural cap at growing microtubule ends. *Cell, 149*(2), 371-382. doi:10.1016/j.cell.2012.02.049

Miller, M. P., Asbury, C. L., & Biggins, S. (2016). A TOG Protein Confers Tension Sensitivity to Kinetochore-Microtubule Attachments. *Cell, 165*(6), 1428-1439. doi:10.1016/j.cell.2016.04.030

Mitchison, T., Evans, L., Schulze, E., & Kirschner, M. (1986). Sites of microtubule assembly and disassembly in the mitotic spindle. *Cell, 45*(4), 515-527.

Mitchison, T., & Kirschner, M. (1984a). Dynamic instability of microtubule growth. *Nature, 312*(5991), 237-242.

Mitchison, T., & Kirschner, M. (1984b). Microtubule assembly nucleated by isolated centrosomes. *Nature, 312*(5991), 232-237.

Nawrotek, A., Knossow, M., & Gigant, B. (2011). The determinants that govern microtubule assembly from the atomic structure of GTP-tubulin. *J Mol Biol, 412*(1), 35-42. doi:10.1016/j.jmb.2011.07.029

Nogales, E., Wolf, S. G., & Downing, K. H. (1998). Structure of the alpha beta tubulin dimer by electron crystallography. *Nature, 391*(6663), 199-203. doi:10.1038/34465

Otomo, T., Tomchick, D. R., Otomo, C., Panchal, S. C., Machius, M., & Rosen, M. K. (2005). Structural basis of actin filament nucleation and processive capping by a formin homology 2 domain. *Nature, 433*(7025), 488-494. doi:10.1038/nature03251

Pampaloni, F., & Florin, E. L. (2008). Microtubule architecture: inspiration for novel carbon nanotube-based biomimetic materials. *Trends Biotechnol, 26*(6), 302-310. doi:10.1016/j.tibtech.2008.03.002

Pecqueur, L., Duellberg, C., Dreier, B., Jiang, Q., Wang, C., Pluckthun, A., . . . Knossow, M. (2012). A designed ankyrin repeat protein selected to bind to tubulin caps the microtubule plus end. *Proc Natl Acad Sci U S A, 109*(30), 12011-12016. doi:10.1073/pnas.1204129109

Pickett-Heaps, J. D., Tippit, D. H., & Porter, K. R. (1982). Rethinking mitosis. *Cell, 29*(3), 729-744.

Piedra, F. A., Kim, T., Garza, E. S., Geyer, E. A., Burns, A., Ye, X., & Rice, L. M. (2016). GDP-to-GTP exchange on the microtubule end can contribute to the frequency of catastrophe. *Mol Biol Cell, 27*(22), 3515-3525. doi:10.1091/mbc.E16-03-0199

Podolski, M., Mahamdeh, M., & Howard, J. (2014). Stu2, the budding yeast XMAP215/Dis1 homolog, promotes assembly of yeast microtubules by increasing growth rate and decreasing catastrophe frequency. *J Biol Chem, 289*(41), 28087-28093. doi:10.1074/jbc.M114.584300

Prota, A. E., Bargsten, K., Northcote, P. T., Marsh, M., Altmann, K. H., Miller, J. H., . . . Steinmetz, M. O. (2014). Structural basis of microtubule stabilization by laulimalide and peloruside A. *Angew Chem Int Ed Engl, 53*(6), 1621-1625. doi:10.1002/anie.201307749

Pruyne, D., Evangelista, M., Yang, C., Bi, E., Zigmond, S., Bretscher, A., & Boone, C. (2002). Role of formins in actin assembly: nucleation and barbed-end association. *Science, 297*(5581), 612-615. doi:10.1126/science.1072309

Reijo, R. A., Cooper, E. M., Beagle, G. J., & Huffaker, T. C. (1994). Systematic Mutational Analysis of the Yeast Beta-Tubulin Gene. *Molecular Biology of the Cell, 5*(1), 29-43.

Rice, L. M., Montabana, E. A., & Agard, D. A. (2008). The lattice as allosteric effector: structural studies of alphabeta- and gamma-tubulin clarify the role of GTP in microtubule assembly. *Proc Natl Acad Sci U S A, 105*(14), 5378-5383. doi:10.1073/pnas.0801155105

Scheres, S. H. (2012). RELION: implementation of a Bayesian approach to cryo-EM structure determination. *J Struct Biol, 180*(3), 519-530. doi:10.1016/j.jsb.2012.09.006

Schneider, C. A., Rasband, W. S., & Eliceiri, K. W. (2012). NIH Image to ImageJ: 25 years of image analysis. *Nat Methods, 9*(7), 671-675.

Schuck, P. (2000). Size-distribution analysis of macromolecules by sedimentation velocity ultracentrifugation and Lamm equation modeling. *Biophysical Journal, 78*(3), 1606-1619. doi:Doi 10.1016/S0006-3495(00)76713-0

Schuck, P. (2010). Sedimentation patterns of rapidly reversible protein interactions. *Biophysical Journal, 98*(9), 2005-2013. doi:10.1016/j.bpj.2009.12.4336

Schuck, P., Perugini, M. A., Gonzales, N. R., Howlett, G. J., & Schubert, D. (2002). Size-distribution analysis of proteins by analytical ultracentrifugation: Strategies and application to model systems. *Biophysical Journal, 82*(2), 1096-1111. doi:Doi 10.1016/S0006-3495(02)75469-6

Schwartz, K., Richards, K., & Botstein, D. (1997). BIM1 encodes a microtubule-binding protein in yeast. *Mol Biol Cell, 8*(12), 2677-2691.

Sievers, F., Wilm, A., Dineen, D., Gibson, T. J., Karplus, K., Li, W., . . . Higgins, D. G. (2011). Fast, scalable generation of high-quality protein multiple sequence alignments using Clustal Omega. *Mol Syst Biol, 7*, 539. doi:10.1038/msb.2011.75

Srayko, M., Kaya, A., Stamford, J., & Hyman, A. A. (2005). Identification and characterization of factors required for microtubule growth and nucleation in the early C. elegans embryo. *Dev Cell, 9*(2), 223-236. doi:10.1016/j.devcel.2005.07.003

Stearns, T., Hoyt, M. A., & Botstein, D. (1990). Yeast mutants sensitive to antimicrotubule drugs define three genes that affect microtubule function. *Genetics, 124*(2), 251-262.

Tang, N. H., Takada, H., Hsu, K. S., & Toda, T. (2013). The internal loop of fission yeast Ndc80 binds Alp7/TACC-Alp14/TOG and ensures proper chromosome attachment. *Mol Biol Cell, 24*(8), 1122-1133. doi:10.1091/mbc.E12-11-0817

Thawani, A., Kadzik, R. S., & Petry, S. (2018). XMAP215 is a microtubule nucleation factor that functions synergistically with the gamma-tubulin ring complex. *Nat Cell Biol, 20*(5), 575-585. doi:10.1038/s41556-018-0091-6

Thomas, J. H., Neff, N. F., & Botstein, D. (1985). Isolation and characterization of mutations in the beta-tubulin gene of Saccharomyces cerevisiae. *Genetics, 111*(4), 715-734.

Ti, S. C., Pamula, M. C., Howes, S. C., Duellberg, C., Cade, N. I., Kleiner, R. E., . . . Kapoor, T. M. (2016). Mutations in Human Tubulin Proximal to the Kinesin-Binding Site Alter Dynamic Instability at Microtubule Plus- and Minus-Ends. *Dev Cell, 37*(1), 72-84. doi:10.1016/j.devcel.2016.03.003

Tseng, W. C., Lin, J. W., Wei, T. Y., & Fang, T. Y. (2008). A novel megaprimed and ligase-free, PCR-based, site-directed mutagenesis method. *Anal Biochem, 375*(2), 376-378. doi:10.1016/j.ab.2007.12.013

Tuszynski, J. A., Carpenter, E. J., Huzil, J. T., Malinski, W., Luchko, T., & Luduena, R. F. (2006). The evolution of the structure of tubulin and its potential consequences for the role and function of microtubules in cells and embryos. *Int J Dev Biol, 50*(2-3), 341-358. doi:10.1387/ijdb.052063jt

Wade, R. H., Chretien, D., & Job, D. (1990). Characterization of microtubule protofilament numbers. How does the surface lattice accommodate? *J Mol Biol, 212*(4), 775-786. doi:10.1016/0022-2836(90)90236-F

Walker, R. A., O'Brien, E. T., Pryer, N. K., Soboeiro, M. F., Voter, W. A., Erickson, H. P., & Salmon, E. D. (1988). Dynamic instability of individual microtubules analyzed by video light microscopy: rate constants and transition frequencies. *J Cell Biol, 107*(4), 1437-1448.

Wang, P. J., & Huffaker, T. C. (1997). Stu2p: A microtubule-binding protein that is an essential component of the yeast spindle pole body. *J Cell Biol, 139*(5), 1271-1280.

Waterhouse, A. M., Procter, J. B., Martin, D. M., Clamp, M., & Barton, G. J. (2009). Jalview Version 2--a multiple sequence alignment editor and analysis workbench. *Bioinformatics, 25*(9), 1189-1191. doi:10.1093/bioinformatics/btp033

Widlund, P. O., Stear, J. H., Pozniakovsky, A., Zanic, M., Reber, S., Brouhard, G. J., . . . Howard, J. (2011). XMAP215 polymerase activity is built by combining multiple tubulin-binding TOG domains and a basic lattice-binding region. *Proc Natl Acad Sci U S A, 108*(7), 2741-2746. doi:10.1073/pnas.1016498108

Winkelman, J. D., Bilancia, C. G., Peifer, M., & Kovar, D. R. (2014). Ena/VASP Enabled is a highly processive actin polymerase tailored to self-assemble parallel-bundled F-actin networks with Fascin. *Proc Natl Acad Sci U S A, 111*(11), 4121-4126. doi:10.1073/pnas.1322093111

Wolyniak, M. J., Blake-Hodek, K., Kosco, K., Hwang, E., You, L., & Huffaker, T. C. (2006). The regulation of microtubule dynamics in Saccharomyces cerevisiae by three interacting plus-end tracking proteins. *Mol Biol Cell, 17*(6), 2789-2798. doi:10.1091/mbc.e05-09-0892

Zanic, M., Widlund, P. O., Hyman, A. A., & Howard, J. (2013). Synergy between XMAP215 and EB1 increases microtubule growth rates to physiological levels. *Nat Cell Biol, 15*(6), 688-693. doi:10.1038/ncb2744

Zhang, R., Alushin, G. M., Brown, A., & Nogales, E. (2015). Mechanistic Origin of Microtubule Dynamic Instability and Its Modulation by EB Proteins. *Cell, 162*(4), 849-859. doi:10.1016/j.cell.2015.07.012

Zhang, R., & Nogales, E. (2015). A new protocol to accurately determine microtubule lattice seam location. *J Struct Biol, 192*(2), 245-254. doi:10.1016/j.jsb.2015.09.015